Contributions to the FEL2000 Conference, August 13-18, 2000 in Durham, North Carolina USA

October 2000, TESLA-FEL 2000-05

Contents

Different focusing solutions for the TTF-FEL undulator

B. Faatz, J. Pflüger

Hamburger Synchrotronstralungslabor (HASYLAB) at Deutsches Elektronen-Synchrotron (DESY), Notkestr. 85, 22607 Hamburg, Germany

Abstract

While aiming at shorter wavelengths, the SASE-FEL undulators become longer. Therefore, maintaining the small electron beam sizes required, the question of what kind of focusing structures should be used for optimum performance becomes of increasing interest.

Present SASE FEL undulators that have been developed and proposed for future FELS both include integrated focusing (TTF-FEL), seperate function quadrupoles combined with the natural undulator focusing (LEUTL) and triplet or FODO structures.

In this contribution, the consequence of the different undulators designs in terms of alignment (tolerances) and flexibility will be discussed.

1. Introduction

First SASE results of the TESLA Test Facility (TTF) FEL have shown that the undulator performs according to predictions [1],[2]. The gain, which is measured to be of the order of 3000, is not close to saturation, this is partly because the tolerance level of 10 μm alignment rms of the electron beam along the entire undulator is not possible as long as the beam based alignment procedure has not been performed, something which has not been possible so far.

The advantages of the present undulator design with its integrated quadrupoles are obvious [3]. The β-function can be made both small and almost constant. This would not be possible with a separate focusing structure unless one uses short undulator segments (≈ 0.4 m). In this case a lot of additional space would be needed in addition to the undulator segments.

However, there are also a number of drawbacks. In order to keep the β-function constant, one needs in the order of two quadrupoles per meter for the TTF-FEL parameters. These have to be aligned with high accuracy. Although the actual alignment of quadrupoles is close to the values needed, one still has to re-steer the beam to compensate for residual quadrupole kicks. In order to know what values of the correctors are needed, beam based alignment has to be performed. Because the quadrupole strength is fixed, one has to vary the electron beam energy in order to minimize dispersion or determine offsets of the beam position monitors (BPM) [5],[6]. For this reason,

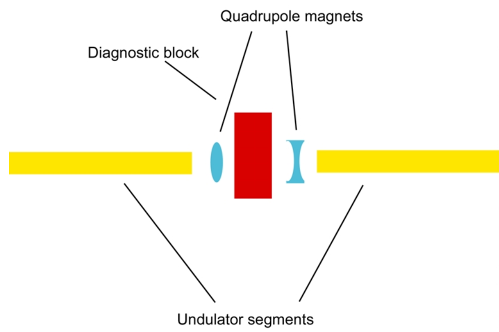

Fig. 1. *Layout of the doublet structure with between undulator segments a doublet and a diagnostic block.*

many steerers and BPMs are needed along the undulator, resulting in a complicated design of the vacuum chamber [7].

As an alternative, one could consider a separate focusing structure. If we do not change the basic design of the undulator, i.e. each segment has a length of approximately 4.5 m, then the quadrupoles at this moment integrated into the undulator would have to be taken out. Additional space is needed for the quadrupoles between the undulator segments. Because of the length of the segments, a FODO-structure is not possible because of the large phase-advance between quadrupoles at β-functions that are needed. In fact, an average β-function smaller than 9 m is not possible, with $\beta_{max}/\beta_{min} \approx 5$. The only alternatives are doublet or triplet structures. Because a triplet structure takes more space and due to problems with debunching (see next section), we have chosen to analyse the doublet structure as shown in Fig. 1.

2. Debunching in a separate focusing structure

In any FEL, debunching occurs due to longitudinal velocity spread, i.e. due to energy spread and finite emittance of the electron beam and the betatron oscillation performed by individual electrons. The influence of energy spread effects and emittance has been well recognized and leads to limits on those two parameters for all FELs [8][9]. Also the influence of focusing has already been described before [10].

The additional problem occuring with the separate focusing is the pathlength difference due to different initial conditions for the individual electrons. An electron with zero transverse position and momentum will enter a next undulator segment at a different time than an electron with an initial angle and offset. Averaged over all electrons, this results in debunching in the space between undulator segments, and therefore a strong decrease in gain. If one looks at the difference in path length of an electron of initial offset and angle (x, x') compared to an on axis electron, this can be written as

$$\Delta\ell = \int_0^z (\sqrt{1 + x'^2(\zeta)} - 1) d\zeta \approx \frac{1}{2} \int_0^z x'^2(\zeta) d\zeta \, ,$$

and similar in the y-direction. Expressed in terms of initial conditions and transfer functions C' and S' (see for example [11])

$$\Delta\ell = \frac{1}{2} x_0^2 \int_0^z C'^2(\zeta) d\zeta + \frac{1}{2} x_0'^2 \int_0^z S'^2(\zeta) d\zeta$$

$$+ x_0 x_0' \int_0^z C'(\zeta) S'(\zeta) d\zeta \, .$$

Averaged over all electrons, this results in

$$\frac{2\delta\ell}{\epsilon} = \frac{2 < \Delta\ell >}{\epsilon} = \beta_0 \int_0^z C'^2(\zeta) d\zeta +$$

$$\gamma_0 \int_0^z S'^2(\zeta) d\zeta - 2\alpha_0 \int_0^z C'(\zeta) S'(\zeta) d\zeta \, , \quad (1)$$

with α_0, β_0 and γ_0 the Twiss parameters. The value for $\delta\ell$ gives an average phase shift, $\sigma_\ell =< \Delta\ell^2 > - < \Delta\ell >^2$ gives the debunching. From Eq. (1) one can see that the effect becomes smaller for smaller emittance. A reduction of the Twiss parameters also makes the effect smaller. This would result in a preference for shorter undulator segments, which on the other hand would result in more quadrupoles to reach the same effective undulator (interaction) length.

In the next section, a numerical example will be worked out for the TTF-FEL parameters.

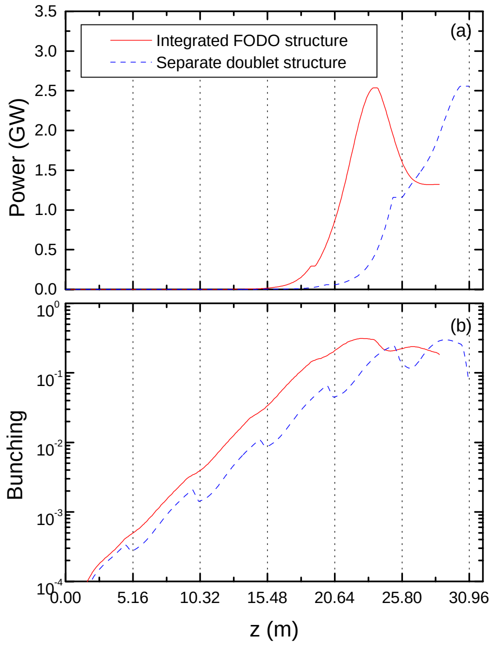

Fig. 2. *Power (a) and bunching (b) for an integrated FODO lattice (solid line) and a separate doublet (dashed line). The vertical dotted lines indicate the start of a new undulator for the doublet structure. The undulator segment length is the same in both cases.*

3. Comparison of integrated with separate function undulator

Because the debunching is most severe at the smallest wavelength, only the 6.4 nm case is studied here. Even if the effect still occurs at longer wavelengths, there is enough undulator space available to reach saturation in those cases.

The following problems will be addressed:

- Increase in saturation length
- Variation in saturation length with effective shotnoise power
- Tolerances on quadrupoles
- Strength of correctors needed to correct quadrupole offsets
- Accuracy of beam position monitors

For the nominal parameters given here, the saturation length is given in Fig. 2a. Even though

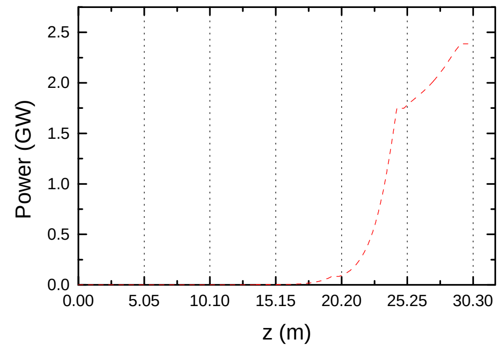

Fig. 3. *Power for a separated doublet with a reduced space between segments. The total space has been reduced to 546 mm, the drift space to 273 mm, the quadrupole gradient is 50 T/m for an optical length of 70 mm. The vertical dotted lines indicate the start of a new undulator.*

the radiation power level still increases in the the last undulator segment, the power in additional segments only increases further by some 25 %. For comparison, the power growth along the undulator is shown for the integrated FODO structure. In Fig. 2b, the corresponding bunching for the two structures is shown.

As can be clearly seen, at each intersection between undulator segments, the bunching decreases in case of the separate doublet focusing structure. The power level, which is reached within 5 undulator segments in case of the integrated FODO structure, is only reached after 6 in the doublet structure. Note also that close to saturation, the bunching still decreases inside the undulator. Changing the pag between segments can prevent this, but decreases the start of the power growth in the linear regime (far from saturation). The possibility of using phase shifters in order to change the phase shift between segments is under investigation.

It is possible to reach the power level at an earlier stage. The large angles introduced due to the stroing focusing, result in a large debunching in the drift space between the two quadrupoles (328 mm in this case). This space, which is planned at the moment for a diagnostic station, could possibly be reduced. Fig. 3 shows the result if this space is reduced.

In Fig. 4, the power growth along the undulator is shown for three different values for the effective shotnoise power. As can be seen, there is still an

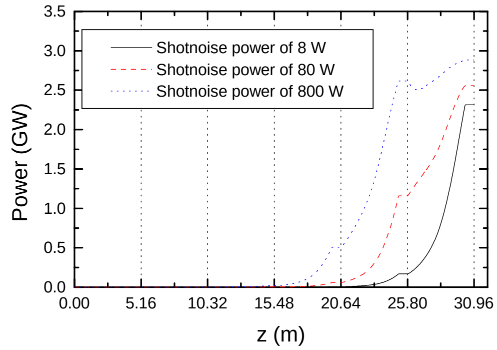

Fig. 4. *Power for a separated doublet with an effective shotnoise power of 8 (solid), 80 (dashed) and 800 W (dotted line). The vertical dotted lines indicate the start of a new undulator.*

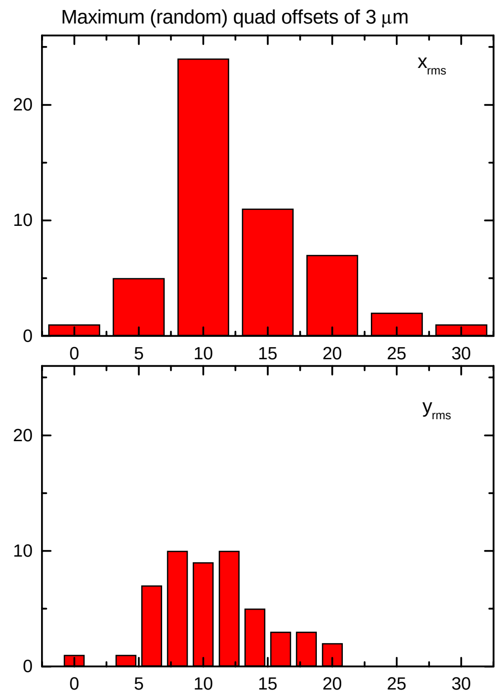

Fig. 5. *rms orbit deviation for a random misalignment of quadrupoles within 3 μm.*

increase in power of approximately 20 % between an input power of 8 and 800 W within the total undulator length.

One of the main advantages of the separate focusing is that the number of quadrupoles can be reduced. The tolerances on undulator alignment becomes more relaxed but is now transferred to the alignment of the individual quadrupoles. In Fig. 5, the rms value of the orbit deviation of the electron beam along the undulator is shown for randomly misaligned quadrupoles within 3 μm. In this case only in 2 % is the power reduction larger than 10 %. For misaligned quadrupoles this number is increased to approximately 8 %. As has been shown before, the rms orbit deviation should not exceed 20 % of the beam size [4]. In this case, because of the large variation in beam size along the undulator, the accuracy of such a general statement is doubtful.

Because an alignment of quadrupoles within 3 μm is not possible, beam based alignment could be used to align the quadrupoles from their prealigned positions to the final position. The two qustions to be answered are then what strength of correctors are needed to correct the quadrupole center and what BPM resolution is required to detect a quadrupole offset of 3 μm or less.

To start with the first of the two, if a corrector would be integrated into the quadrupole, it has to be able to shift its center. With a gradient Q T/m, an offset δx results in a dipole field of $Q \times \delta x$. For a gradient of 37 T/m and a typpical offset of 100 μm, the corrector has to have a minimum strength of 37 Gauss. This value is rather strong. In case that the quadrupole length has to be reduced in order to reduce the debunching or if a 100 μm prealignment cannot be achieved, this value becomes even larger.

As a first indication of the resolution of the BPMs, the offset at a BPM position due to a quadrupole with an offset of 3 μm can be calculated. For a quadrupole with gradient Q, an offset δx and length L_Q, the kick is

$$x' = \frac{e}{\gamma mc} Q \delta x L_Q \, .$$

The offset measured at the position of the BPM is then $x' L_u$, with L_u approximately the length of the undulator segment, i.e. 4.5 m (assuming that the undulator can be considered as a drift space. For the values in Table 1, the offset measured is 10 μm for a 1 GeV beam. This is the resolution that is less than a factor of two more accurate than we have at the moment.

Table 1
Parameters of the TESLA Test Facility FEL with separate doublet focusing

Electron beam	
Energy, $\mathcal{E}_0$	1 GeV
Peak current, I_0	2.5 kA
rms bunch length, σ_z	$50\,\mu$m
rms normalized emittance	2π mm mrad
rms energy spread	1 MeV
External β-function,	4.5 m
rms transverse beam size	70 μm
Undulator	
Type	Planar, Hybrid
Focusing structure	Separate, Doublet
Period, λ_w	27.3 mm
Segment length	4.45 m
Distance between segments	710.0 mm
Peak magnetic field, H_w	0.5 T
Focusing structure	Doublet
Quadrupole optical length	82.0 mm
Quadrupole strength	37.0 T/m
Output radiation	
Wavelength, λ	$6 - 60$ nm

4. Discussion

Under ideal circumstances, the integrated FODO-structure used in the TESLA Test facility undulator has a better performance. At the same time, the alignment tolerances for the undulator is very tight. In addition, the vacuum chamber with integrated beam position monitors (BPMs) and corrector coils is more complicated to construct than the chamber for the separate function lattice. Although the performnce of the latter structure is not as good, its advantage is that the alignment of undulators is more relaxed, less BPMs and correctors are needed and the beam based alignment procedure to align the quadrupoles is easier to perform. The main reason for the gain degradation needs more study.

Acknowledgement:

The authors would like to thank J. Lewellen, S. Reiche, E.L. Saldin, G. Schmidt, E.A. Schneidmiller and M.V. Yurkov for many useful discussions.

References

[1] "A VUV Free Electron Laser at the TESLA Test Facility: Conceptual Design Report", DESY Print TESLA-FEL 95-03, Hamburg, DESY, 1995

[2] "First observation of self-amplified Spontaneous Emission in a Free-Electron Laser at 109 nm Wavelength", J. Andruszkow et. al., submitted to Phys. Rev. Letters.

[3] J. Pflüger, P. Gippner, A. Swiderski, T. Vielitz Proceedings of the Free Electron Laser Conference in Hamburg, Germany.

[4] B. Faatz, J. Pflüger and Y.M. Nikitina, Nucl. Instr. and Meth. A393 (1997) 380.

[5] K. Flöttmann, B. Faatz, J. Rossbach, E. Czuchry, Nucl. Instr. and Meth. A416 (1998) 152.

[6] P. Castro, B. Faatz, K. Flöttmann, Nucl. Instr. and Meth. A427 (1999) 12.

[7] U. Hahn, P.K. deh Hartog, J. Pflüger, M. Rüter, G. Schmidt, E.M. Trakhtenberg Nucl. Instr. and Meth. A445 (2000) 442.

[8] W. Brefeld, B. Faatz, Y.M. Nikitina, J. Pflüger, P. Pierini, J. Rossbach, E.L. Saldin, E.A. Schneidmiller, M.V. Yurkov Nucl. Instr. and Meth. A393 (1996) 295.

[9] W. Brefeld, B. Faatz, Y.M. Nikitina, J. Pflüger, P. Pierini, J. Rossbach, E.L. Saldin, E.A. Schneidmiller, M.V. Yurkov Nucl. Instr. and Meth. A393 (1997) 119.

[10] E.T. Scharlemann J. Appl. Phys. 58(1985) 2154.

[11] H. Wiedemann, Particle Accelerator Physics, Springer, Berlin, 1995

Development of a Pump-Probe Facility Combining a Far-Infrared Source with Laser-Like Characteristics and a VUV Free Electron Laser

B. Faatz [a], A.A. Fateev [b], J. Feldhaus [a], J. Krzywinski [c], J. Pflueger [a], J. Rossbach [a], E.L. Saldin [a], E.A. Schneidmiller [a], M.V. Yurkov [b]

[a] *Deutsches Elektronen-Synchrotron (DESY), Notkestrasse 85, D-22607 Hamburg, Germany*

[b] *Joint Institute for Nuclear Research, Dubna, 141980 Moscow Region, Russia*

[c] *Institute of Physics of the Polish Academy of Sciences, 02688 Warszawa, Poland*

Abstract

The TESLA Test Facility (TTF) at DESY is a facility producing sub-picosecond electron pulses for the generation of VUV or soft X-ray radiation in a free electron laser (FEL). The same electron pulses would also allow the direct production of high-power coherent radiation by passing the electron beam through an undulator. Intense, coherent far-infrared (FIR) undulator radiation can be produced from electron bunches at wavelengths longer than or equal to the bunch length. The source described in this paper provides, in the wavelength range 200–300 μm, a train of about 10 ps long radiation pulses, with about 1 mJ of optical energy per pulse radiated into the central cone. The average output power can exceed 50 W. In this conceptual design we assume to use a conventional electromagnetic undulator with a 60 cm period length and a maximum field of 1.5 T. The FIR source will use the spent electron beam coming from the VUV FEL which allows one to extend significantly the scientific potential of the TTF without interfering with the main option of the TTF FEL operation. The pulses of the coherent FIR radiation are naturally synchronized with the VUV pulses from the main TTF FEL, enabling pump-probe techniques using either the FEL pulse as a pump and the FIR pulse as a probe, or vice versa.

1. Introduction

The FIR range of the electromagnetic spectrum is not well covered by intense sources except of a few operating FELs. The analysis of the parameters of existing FIR FELs shows that practical sources of broadly tunable, powerful coherent FIR radiation remains essentially unavailable at wavelengths beyond 200 μm [1–3]. This situation, however, might change soon. The development of magnetic bunch compression systems, together with advances in superconducting accelerator technology and design, now offers the new possibility of laser-like sources in the far-infrared wavelength range. The generation of relativistic, sub-picosecond electron pulses allows the direct production of high-power, coherent, narrow-band, FIR radiation by passing the electron beam through an undulator. This provides a reliable and easily tunable powerful source of FIR radiation for scientific applications [4,5].

The TTF is a facility producing sub-picosecond electron pulses (50 μm rms) for the generation of VUV or soft X-ray radiation. Utilizing these sub-picosecond electron bunches can also provide broadband FIR source. Intense, coherent FIR radiation can be produced from sub-picosecond electron bunches at wavelengths longer than or equal to the bunch length. The total radiation from an electron bunch is the summation of the electric fields emitted by each individual electron and the total radiated energy is then equal to the square of the total electric field. The coherent radiation energy is proportional to the square rather than linear proportional to the number of radiating electrons. Since there are 6×10^9 electrons in each bunch, the radiation intensity is enhanced by this large factor over the incoherent radiation. This paper describes such a coherent source, proposed as part of the TTF FEL user facility. The FIR source addresses the needs of the science community for a high-brightness, tunable source covering a broad region of the far-infrared spectrum – from 200 to 300 μm. The FIR radiator described in this paper provides a train of about 10 ps long pulses with about 1 mJ of optical energy per pulse into the central cone. The average output power can exceed 50 W.

The pump-probe technique is one of the most promising methods for the application of a high power FIR source [6]. It is the aim of the present project to develop a user facility for pump-probe experiments in the picosecond regime, combining FIR and short-wavelength FEL radiation. The TTF will allow, for the first time, the integration of a far-infrared coherent radiation source and a VUV beamline. One type of experiments will use the VUV FEL beam as a pump and the far-infrared photon beam as a probe; in this mode, researchers will be able to study the vibrational structure of highly excited and superexcited molecules. The other mode – far-infrared beam pump and VUV beam probe – can be used to study cluster energetics and dynamics. The FIR radiation can be used to excite the clusters, which can subsequently be dissociated or ionized by the VUV radiation. Spectroscopic and structural information can thus be extracted. Spectroscopy of gas-phase free radicals will also benefit from the FIR beam pump and VUV beam probe experiments. In these experiments, a cold molecular beam containing a small concentration of radicals would be excited by the intense FIR beam, tunable across the absorption spectrum. Since the density of radicals in the beam is not high enough to allow the direct measurement of absorption, a VUV beam from the TTF FEL would be used to detect the infrared-exited states of molecules by selectively ionizing the vibrationally excited radicals.

2. Temporal coherent undulator radiation

The electron beam current is made up of moving electrons randomly arriving at the entrance to the undulator:

$$I(t) = (-e)\sum_{k=1}^{N} \delta(t - t_k) \ ,$$

where $\delta(\cdots)$ is the delta function, $(-e)$ is the charge of the electron, N is the number of electrons in a bunch, and t_k is the random arrival time of the electron at the undulator entrance. The electron bunch profile is described by the profile function $F(t)$. The beam current averaged over an ensemble of bunches can be written in the form:

$$\langle I(t) \rangle = (-e)NF(t) \ .$$

The probability of arrival of an electron during the time interval $t, t + \mathrm{d}\,t$ is equal to $F(t)\,\mathrm{d}\,t$.

The radiation power at the frequency ω, averaged over an ensemble, is given by the expression:

$$\langle P(\omega) \rangle = p(\omega)[N + N(N-1)|\bar{F}(\omega)|^2] \ ,$$

where $p(\omega)$ is the radiation power from one electron and $\bar{F}(\omega)$ is the Fourier transform of the bunch profile function. For wavelengths shorter than the bunch length the form factor reduces to zero and approaches unity for longer wavelengths.

To optimally meet the needs of basic research with FIR coherent radiation, it is desirable to provide specific radiation characteristics. To generate this characteristics, radiation is produced from undulator installed along the electron beam path. The undulator equation

$$\omega = 2ck_{\mathrm{w}}\gamma^2 \left[1 + \frac{K^2}{2} + \gamma^2\theta^2\right]^{-1}$$

tells us the frequency of radiation as a function of undulator period $\lambda_{\mathrm{w}} = 2\pi/k_{\mathrm{w}}$, undulator parameter K, electron energy γ, and polar angle of observation θ. Note that for radiation within the cone of half angle

$$\theta_{\mathrm{con}} = \frac{\sqrt{1 + K^2/2}}{\gamma\sqrt{N_{\mathrm{w}}}}$$

the relative spectral bandwidth $\Delta\omega/\omega \simeq 1/N_{\mathrm{w}}$, where N_{w} is the number of undulator periods. The energy radiated into the central cone, for a single electron, is given by

$$\Delta E_{\mathrm{con}} \simeq \pi e^2 A_{\mathrm{JJ}}^2 \omega_0 K^2/[c(1 + K^2/2)] \ .$$

Table 1

Parameters of the FIR coherent radiation source

Electron beam	
energy	1000 MeV
bunch charge	1 nC
rms bunch length	50 μm
rms emittance	2 π mm-mrad/γ
rms energy spread	2.5 MeV
bunch repetition rate	9 MHz
duty factor	1 %
Undulator	
type	Planar
period	60 cm
peak magnetic field	1.2–1.5 T
number of periods	10
Output radiation	
wavelength	200–300 μm
bandwidth	transform-limited
peak power	100 MW
average power	50 W
micropulse duration	10 ps
micropulse energy	1 mJ

Here $\omega_0 = 2\gamma^2 k_{\mathrm{w}}/(1+K^2/2)$ is the resonance frequency, $A_{\mathrm{JJ}} = [J_0(Q) - J_1(Q)]$, J_n is the Bessel function of nth order, $Q = K^2/(4+2K^2)$. The coherent radiation enhances the energy radiated into the central cone by a factor of $N|\bar{F}(\omega_0)|^2$.

3. Facility Description

In the far-infrared, beyond 200 μm, a source based on coherent undulator radiation has unique capabilities. In this paper we propose to integrate such a source into the TESLA Test Facility at DESY [7,8]. This source will be able to deliver up to 800 μs long trains of FIR pulses at a separation of 111 ns with about 10 ps duration [1], 1 mJ energy radiated into the central cone, and 200–300 μm wavelength. The superconducting linac will operate at about 1 % duty factor, and the average output power of coherent FIR radiation can exceed 50 W.

We propose to install an additional undulator after the VUV SASE FEL. Because the FIR source uses the electron beam coming from the VUV FEL, the proposed source operates in a "parasitic" mode not interfering with the main mode of the VUV FEL operation (see Fig. 1). Starting point of the design are the project parameters of the electron beam after the VUV FEL at the TTF (see Table 1). The planar undulator is an inexpensive electromagnetic device with 10 periods, each 60 cm long. At the operation wavelength of the FIR source around 300 μm the peak value of the magnetic field is about 1.5 T.

Many practical applications require to control the shape and time characteristics of the FIR pulse. For instance, closely spaced picosecond FIR pulses with controllable phase relations are needed for coherent multi-photon excitation and selective excitation of, for

[1] When the electron bunch moves along the undulator, the electromagnetic wave advances the electron beam by one wavelength at one undulator period

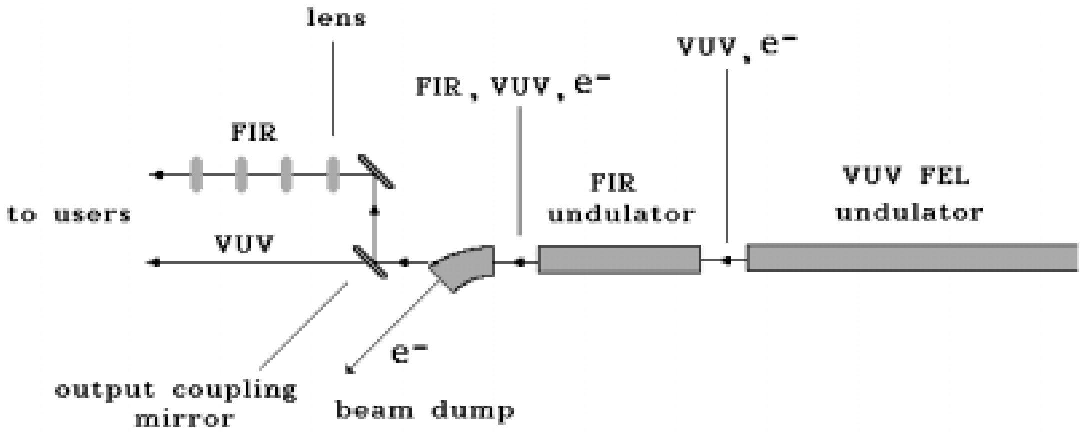

Fig. 1. Schematic layout of the FIR-VUV pump-probe facility

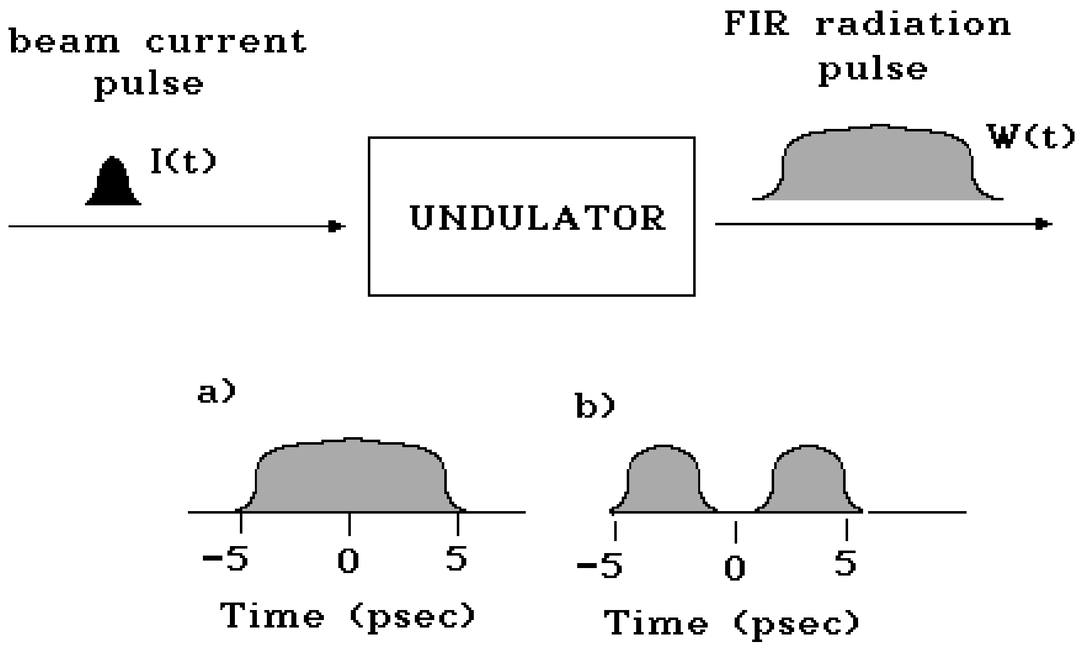

Fig. 2. FIR pulse profiles generated by the FIR undulator in the central cone (300 μm wavelength). Plot (a) illustrates the pulse produced by a uniform undulator (rectangular pulse of 10 ps duration). Plot (b) illustrates the case when four central poles are switched off (two pulses of 3 ps duration each delayed by 3 ps)

example, certain molecular vibrations. The proposed FIR source provides wide possibilities to control and modify in a well-defined manner the shape of the radiation pulse on a picosecond time scale (see Fig. 2). The electron beam passing uniform undulator produces FIR pulse with rectangular profile. FIR optical pulses can be shaped in a complicated manner by means of individual tuning of the magnetic field in each period. It is important to stress that resulting shape (spectrum) of FIR pulses can be well described analytically for this source.

Proposed FIR source is compatible with the layout of the TTF and the VUV FEL at DESY, and can be realized with minimal additional efforts. The undulator and outcoupling optical system can be installed in the unoccupied straight vacuum line used for the electron and VUV beamlines behind the dipole magnet separating the electron beam from the VUV beam (see Fig. 1). In order to make use of the FIR radiation an additional mirror is needed to couple out the major fraction of the optical power in the central cone and to direct it to the experimental area. The distance between the mirror and the exit of the second undulator is 10 m, the distance between the mirror and the exit of the FEL undulator is about 16 m. The minimum size of the hole in the outcoupling mirror is defined by the condition that VUV radiation losses due to hole aperture limitation should be avoided. The fraction of the output FEL power passing the mirror hole is calculated from the angular distribution of the VUV radiation (20 μrad rms). For a hole diameter of 2 mm the fraction of VUV power directed into the experimental area is close to 100%. Due to the angle-frequency correlation of the coherent undulator radiation the required frequency bandwidth of radiation could be provided by angular selection. To provide a natural selection of coherent radiation in the central cone ($\theta_{\mathrm{con}} \simeq 5$ mrad), the radius of the mirror should be equal to 6 cm at a distance of about 10 m between the exit of the second undulator and the mirror.

The operation of the proposed FIR source is insensitive to the emittance of the electron beam, since the condition of optimal electron beam transverse size is: $\sigma^2 \ll Lc/\omega \simeq 1\ \mathrm{cm}^2$, where L is undulator length. The analysis of the parameters of the FIR source has shown that it will operate reliably even for an emittance exceeding the project value of 2π mm mrad by two orders of magnitude.

An undulator is a sequence of bending magnets where particles with different energies have different path length. As a result, the energy spread in the beam leads to the bunch lengthening in the undulator. When an electron bunch passes the FIR undulator, radiation interaction induces additional energy spread in the electron beam which also can lead to bunch lengthening. Recently, the problem connected with radiative interaction of the particles in a line-charge microbunch moving in an undulator has been investigated analytically [9]. In the case of a Gaussian bunch profile the induced energy spread ΔE_{f} is given by:

$$\frac{\Delta E_{\mathrm{f}}}{E} = \frac{r_{\mathrm{e}} N K^2 L}{\sqrt{2\pi}\sigma_z^2\gamma^3} G(p, K) \ , \qquad (1)$$

where, r_{e} is the classical electron radius, $p = k_{\mathrm{w}}\sigma_z\gamma^2/[(1 + K^2/2)]$ is the bunch length parameter, and σ_z is the rms bunch length. Parameter of the FIR source project are: $N = 6 \cdot 10^9$, $\sigma_z = 50\ \mu$m, $K = 70$ (for 200 μm wavelength), $L = 6$ m, and $\gamma = 2 \cdot 10^3$. The value of G is $G \simeq 0.5$. Substituting these values into (1), we obtain an induced correlated energy spread at the exit of undulator $\Delta E_{\mathrm{f}}/E \simeq 2\%$. This leads to an increase of the bunch length:

$$\Delta l_{\mathrm{b}} \simeq \frac{L(1+K^2/2)}{2\gamma^2}\frac{\Delta E_{\mathrm{f}}}{E} \simeq 20\ \mu\mathrm{m}\ .$$

Since this value is much less than the radiation wavelength $\lambda \simeq 200\ \mu$m, we can conclude that bunch decompression in the undulator due to induced energy spread should not be a serious limitation in our case.

Acknowledgments

We thank D. Trines and J.R. Schneider for interest in this work and support, and A.F.G. van der Meer for useful discussions on scientific applications of coherent far-infrared sources.

References

[1] G. Ramian, Nucl. Instrum. and Methods A 318(1992)225

[2] D. Oepts, A. F. G. van der Meer, and P. W. van Amersfort, Infrared Phys. Tech. 36 (1995)297

[3] H. A. Schwettman, T. I. Smith, and R. L. Swent, Nucl. Instrum. and Methods A 375(1996)662

[4] D. Bocek et al., SLAC-PUB-7016, Nucl. Instrum. and Methods A 375(1996)13

[5] C. Settakorn et al., SLAC-PUB-7812 May 1998

[6] K.-J. Kim et al., LBL preprint Pub-5335(1992)

[7] "A VUV Free Electron Laser at the TESLA Test Facility: Conceptual Design Report", DESY Print TESLA-FEL 95-03, Hamburg, DESY, 1995

[8] J. Rossbach, Nucl. Instrum. and Methods A 375(1996)269

[9] E. L. Saldin, E. A. Schneidmiller, and M.V. Yurkov, Nucl. Instrum. and Methods A 417(1998)158

Development of a Facility for Probing the Structural Dynamics of Materials with Femtosecond X-ray Pulses

B. Faatz [a], A.A. Fateev [b], J. Feldhaus [a], K. Floettmann [a], T. Tschentscher [a], J. Krzywinski [c], J. Pflueger [a], J. Rossbach [a], E.L. Saldin [a], E.A. Schneidmiller [a], M.V. Yurkov [b]

[a] *Deutsches Elektronen-Synchrotron (DESY), Notkestrasse 85, D-22607 Hamburg, Germany*

[b] *Joint Institute for Nuclear Research, Dubna, 141980 Moscow Region, Russia*

[c] *Institute of Physics of the Polish Academy of Sciences, 02688 Warszawa, Poland*

Abstract

We propose to use Thomson backscattering of far-infrared (FIR) pulses (100-300 μm wavelength range) by a 500 MeV electron beam to generate femtosecond X-rays at the TESLA Test Facility (TTF) at DESY. Using the parameters of the photocathode rf gun and the magnetic bunch compressors of the TESLA Test Facility (TTF), it is shown that electron pulses of 100-fs (FWHM) duration can be generated. Passing the short electron bunches through an undulator (after the conversion point) can provide a FIR high-power source with laser-like characteristics. On the basis of the TTF parameters we expect to produce X-ray pulses with 100-fs duration, an average brilliance of nearly 10^{13} photons s^{-1} mrad^{-2} mm^{-2} per 0.1% BW at a photon energy 50 keV. The total number of Thomson backscattered photons, produced by a single passage of the electron bunch through the mirror focus, can exceed 10^7 photons/pulse. We also describe the basic ideas for an upgrade to shorter X-ray pulse duration. It is demonstrated that the TTF has the capability of reaching the 10^{12} photons s^{-1} mrad^{-2} mm^{-2} per 0.1% BW brilliance at a ten femtosecond scale pulse duration.

1. Introduction

Understanding the structural dynamics of materials on the fundamental time scale of atomic motion represents an important frontier in condensed matter research because chemical reactions, phase transitions, and surface processes are ultimately driven by the motion of atoms on the time scale of one vibrational period ($\simeq$ 100 fs). Resent efforts at applying X-rays to probe structural dynamics have used

Table 1
Major electron beam parameters for 100 fs-scale X-ray facility option

Parameter	Value
beam energy	500 MeV
transverse emittance	$2\ \pi$ mm-mrad$/\gamma$
longitudinal emittance	$30\ \pi$ keV-mm
bunch charge	1 nC
bunch repetition rate	9 MHz
duty factor	1%

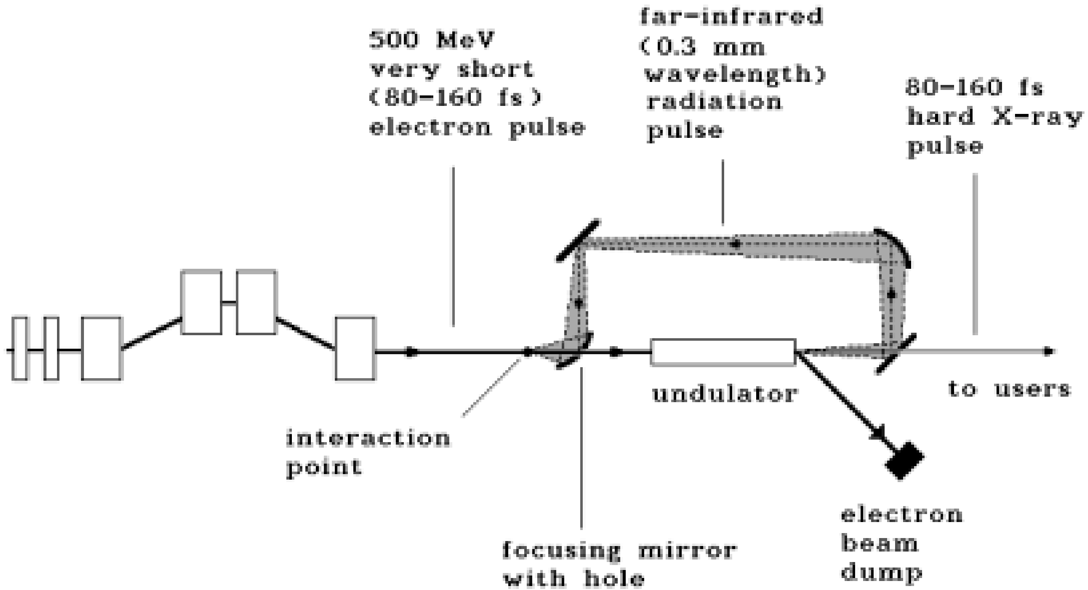

Fig. 1. Basic scheme of the femtosecond X-ray facility

a synchrotron source combined with a femtosecond optical laser [1]. Femtosecond synchrotron radiation pulses were generated directly from an electron storage ring ALS. An ultrashort laser pulse was used to modulate the energy of electrons within a 100-femtosecond slice of the stored 30-picosecond electron bunch. The energy-modulated electrons were spatially separated from the long bunch and used to generate 300-femtosecond X-ray pulses at a bending magnet beamline. The same technique can be used to generate 100-femtosecond X-ray pulses. On the basis of the parameters of an ALS small-gap undulator and for example, laser pulses of 25 fs and 100 μJ at a repetition of rate 20 kHz, Schoenlein and co-workers expect in the future an average brilliance of 10^{11} photons s^{-1} mrad^{-2} mm^{-2} per 0.1% BW at a photon energy of 2 keV.

Another project of a femtosecond X-ray facility, which is described in detail in this paper, is based on the idea to use Thomson backscattering of a high power far-infrared radiation pulse from a relativistic electron bunch. In our project we use 500 MeV electron bunches from the Tesla Test Facility (TTF) linear accelerator [2] and 200 MW optical pulses from a FIR source based on coherent undulator radiation (see Fig. 1). The basic TTF electron beam parameters are given in Table 1. In a backscattering geometry,

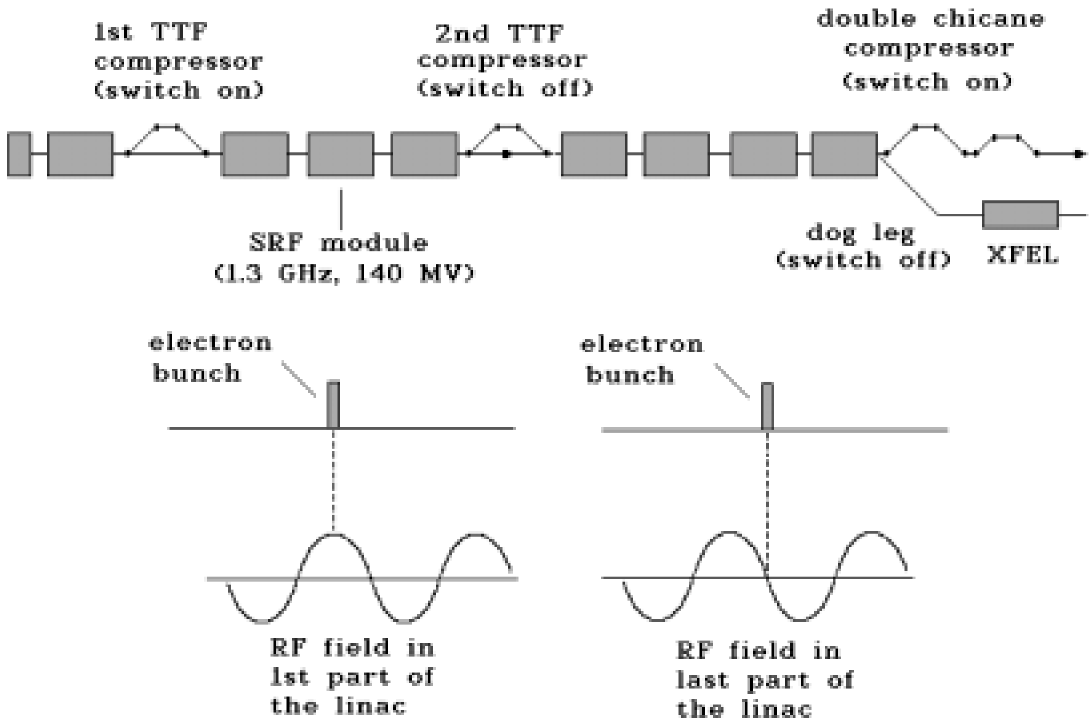

Fig. 2. Femtosecond X-ray facility compression and acceleration schematic

the duration of the scattered X-ray burst is determined by the length of the electron bunch. In order to achieve a small bunch length in the conversion point, the bunch must be compressed in magnetic chicanes. For this project we assume to use a two-stage compressor design (see Fig. 2). The first TTF magnetic chicane compresses the bunch from $\sigma_z \simeq 1.6$ mm to $\sigma_z \simeq 0.4$ mm. After the first bunch compressor the electron bunch is accelerated in the next part of the TTF linac from 150 MeV to 500 MeV energy. Then the electron bunch passes the last part of the accelerating structure (voltage $V = 500$ MV) at 90° crossing phase and the energy spread of the electron beam is increased to about 5 MeV. The electron bunch with such large correlated energy spread can be compressed in special double magnetic chicane down to $\sigma_z \simeq 10\ \mu$m.

2. Yield of X-ray photons

We propose to install a special undulator after the interaction point. Intense, coherent far-infrared undulator radiation can be produced from electron bunches at wavelengths longer than the bunch length. The undulator equation $\omega_0 = 2ck_{\mathrm{w}}\gamma^2\left[1+K^2/2\right]^{-1}$ tells us the resonance frequency of radiation as a function of undulator period $\lambda_{\mathrm{w}} = 2\pi/k_{\mathrm{w}}$, undulator parameter K and relativistic factor γ. Note that for radiation within the central cone the relative spectral bandwidth $\Delta\omega/\omega \simeq 1/N_{\mathrm{w}}$, where N_{w} is the number of undulator periods. The energy radiated into the central cone in the case when the resonance wave length much longer that the bunch length is given by ($K^2 \gg 1$): $\Delta E_{\mathrm{con}} \simeq \pi e^2\omega_0 N_{\mathrm{e}}^2/c$.

The planar undulator is an inexpensive electromagnetic device with 20 periods, each 60 cm long. At the operation wavelength of the FIR source around 100 μm and an electron beam energy of 500 MeV the peak value of the magnetic field is about 0.5 T. In the case when the number of electron per bunch is about $N_\mathrm{e} = 6 \times 10^9$ (1 nC) the FIR source described above provides a train of 6.6 ps long micropulses (the wave advances the electron beam by one wavelength at one undulator period), with 1.5 mJ of optical energy per micropulse radiated into the central cone at 100 μm wavelength. To provide a natural selection of coherent radiation in the central cone ($\theta_\mathrm{cone} \simeq 4$ mrad), the radius of the mirror should be equal to 5 cm at a distance of about 10 meters between the exit of the FIR undulator and the mirror.

To obtain an effective conversion of the primary photons into X-ray photons, the far-infrared beam should be focused on the electron beam. This may be performed, for instance, by means of a metal focusing mirror (see Fig. 1). Electrons move along the z axis and pass through the mirror focus. The conditions of optimal focusing are as follow ($l_\mathrm{e} \ll l_\mathrm{opt}$):

$$\sigma^2_{x,y} \ll [4cF/(\omega a_0)]^2 \ , \quad F^2 \ll a_0^2 l_\mathrm{opt}/(2\lambda) \ ,$$

where $\sigma_{x,y} = \sqrt{\epsilon_{x,y}\beta_{x,y}}$ is the transverse electron beam size at the conversion point, $\beta_{x,y}$ is the beta function, $\epsilon_{x,y}$ is transverse emittance of the electron beam, F is the focal length of the mirror, a_0 is the radius of the optical beam spot on the mirror, l_e and l_opt are the lengths of electron and optical bunch, respectively. The first condition assumes the transverse size of the electron beam at the conversion point to be much less than the FIR beam size. The second condition means that the characteristic axial size of the region with a strong optical field is much less than the length of the optical bunch.

Hard X-ray photons are produced by means of Thomson backscattering of the optical photons by the high energy electrons. Relativistic effects cause the X-ray flux to be strongly peaked in the forward direction; for the 500 MeV electron beam ($\gamma = 10^3$) and 100 μm radiation wavelength used in our project, the Thomson backscattered X-rays are peaked at a maximum energy $\hbar\omega_\mathrm{x-ray} = 4\gamma^2\hbar\omega_\mathrm{opt} \simeq 50$ keV.

When the conditions of optimal focusing are fulfilled the total number of X-ray photons, produced by a single passage of the electron beam through the mirror focus, is given by the following relation:

$$\Delta N_\mathrm{x-ray} = \frac{2W\sigma_\mathrm{T}}{\hbar c^2} N_\mathrm{e} \ ,$$

where σ_T is the total Thomson cross section, N_e is the number of electrons in the bunch, and W is the peak power of the optical beam. An important feature of the obtained result is that the number of produced X-ray photons does not depend on the details of the optical field distribution at the mirror surface and is defined by the peak optical beam power only. Taking into account the TTF parameters and FIR source parameters (see Table 1) and assuming that the conditions of optimal focusing are fulfilled, we obtain a yield of X-ray photons of $\mathrm{d}\, N_\mathrm{x-ray}/\mathrm{d}\, t \simeq 2 \times 10^{12}\ \mathrm{s}^{-1}$.

The quality of the radiation source is described usually by the brilliance defined as the density of photons in the six-dimensional phase space volume:

$$B = \frac{1}{4\pi^2\sigma_x\sigma'_x\sigma_y\sigma'_y}\left(\lambda\frac{\mathrm{d}^2\, N_\mathrm{ph}}{\mathrm{d}\,\lambda\,\mathrm{d}\, t}\right) \ .$$

Let us proceed with numerical example for 160 fs (FWHM) electron pulse duration. The main parameters of the electron beam are presented in Table 1. The source of primary photons has the following parameters: wavelength 100 μm, peak power $W \simeq 250$ MW, pulse duration 6.6 ps. Assuming the focus distance of the mirror to be equal to $F \simeq 20$ cm and the radius of the FIR beam at the focusing mirror $a_0 \simeq 10$ cm we find that the condition of optimal focusing will be fulfilled at $\beta \simeq 10$ cm. Under these conditions we calculate an average brilliance of 10^{13} photons s^{-1} mrad^{-2} mm^{-2} per 0.1% BW at a photon energy of 50 keV

In order to produce 80 fs long electron pulses the bunch charge must be reduced to about 0.3 nC. It will be done in stages to avoid coherent synchrotron radiation effects (longitudinal wakefield) limiting the achievable bunch length and beam emittance. On the basis of the parameters of the electron beam with 80-fs pulses and the FIR source we expect an average brilliance of about 10^{12} photons s^{-1} mrad^{-2} mm^{-2} per 0.1% BW at a photon energy of 50 keV.

3. Bunch compressors

The proposed phase bunching system is sketched in Fig. 2. Compressing the bunch will be done in stages to avoid space charge and coherent synchrotron radiation (CSR) effects limiting the achievable bunch length and transverse emittance. The first compression is from 1.6 mm to 400 μm. It consists of a 150 MeV accelerating module followed by the first TTF magnetic chicane generating the R_{56} needed for bunch compression [3]. Calculations show that induced energy spread and emittance dilution should not be a serious limitation in BC1 [3].

After leaving the first bunch compressor the electron bunch of 400μm length is accelerated in the next part of the TTF linac with an on-crest phase from 150 MeV to 500 MeV. For the second compression the required large correlated energy spread in the bunch of 5 MeV is induced by passing the last part of the accelerating structure at 90° crossing phase. Our analysis shows that adequate solution for the BC2 design is a double chicane. Each chicane is twelve meters long and contains four C-type rectangular bending magnets. For compression from 400 μm to 20 μm the parameters of BC2 are practically identical to that designed for LCLS BC2 [4]. The first and second chicanes generate $R_{56} = 3$ cm and 0.3 cm at bend angle $\theta_{\rm B1} = 3.4^\circ$ and $\theta_{\rm B2} = 1.3^\circ$, respectively. Four quadrupoles are placed between the chicanes in locations where the dispersion passes through zero. Since the energy spread generated by CSR is coherent along the bunch, its effect on the transverse emittance can be compensated in a double chicane with optical symmetry to cancel the longitudinal-to-transverse coupling [4].

4. Future potential

For the 100-femtosecond X-ray facility described above, we have adopted the TTF design parameters for the photocathode rf gun injector [2]. In order to achieve a 5 μm rms bunch length (40-fs pulse duration) a new mode of operation of the TTF injector is required. The injector should produce 100 pC bunches with a longitudinal emittance of 10 π keV-mm and a normalized transverse emittance of 1 π mm-mrad. In order to reach $B \simeq 10^{13}$ photons s^{-1} mrad^{-2} mm^{-2} per 0.1% BW, the bunch repetition rate (within a macropulse) would have to be increased up to 108 MHz. Such values of bunch charge and repetition rate would keep the mean value of average current during a macropulse and the mean power of the laser system (below 2 W) at the TTF design level. As a result, no modifications are necessary for the rf gun. In this high repetition rate option only the laser system needs hardware modifications.

Analysis of the TTF parameters shows that an extension to bunch lengths shorter than 5 μm rms is also direct and straightforward but needs increasing linear correlated energy spread. Compressing the bunch in our case will be done in stages to avoid RF curvature effect. The proposed solution is to perform compression in three steps: compression at 150 MeV, decompression at 500 MeV before the last part of the linac and compression at 500 MeV at the linac exit. In this scheme the energy spread of the electron beam is increased to about 15 MeV. An electron bunch with such a large correlated energy spread and 30 pC charge per bunch, can be compressed in a special double magnetic chicane down to $\sigma_z \simeq 2$ μm. The average brilliance of such a 10 fs-scale X-ray facility could reach a value of $B \simeq 10^{11}$ photons s^{-1} mrad^{-2} mm^{-2} per 0.1% BW. This requires installation of an additional chicane for decompression and modification of the photoinjector laser system.

The yield of X-ray photons may be increased further more by means of organizing several conversion points. After crossing the first conversion point, the optical beam is directed to an optical delay line and then it is focused at the next electron bunch, etc. Taking into account that the reflection losses of metal focusing mirrors for radiation of 100 μm wavelength are only about 0.5%, we may conclude that each optical bunch can effectively interact with many electron bunches. As a result, a yield of X-ray photons may be increased by a factor of about 10.

Acknowledgments

We thank D. Trines and J.R. Schneider for interest in this work and support.

References

[1] R. W. Schoenlein et al., Science 287, 2237(2000)

[2] J. Rossbach, Nucl. Instrum. and Methods A 375(1996)269

[3] T. Limberg et al., Nucl. Instrum. and Methods A 375(1996)322

[4] The Linac Coherent Light Source (LCLS) Design Study Report, SLAC-R-521, 1998

Development of a Pump-Probe Facility with Sub-Picosecond Time Resolution Combining a High-Power Ultraviolet Regenerative FEL Amplifier and a Soft X-ray SASE FEL

B. Faatz [a], A.A. Fateev [b], J. Feldhaus [a], J. Krzywinski [c], J. Pflueger [a], J. Rossbach [a], E.L. Saldin [a], E.A. Schneidmiller [a], M.V. Yurkov [b]

[a] *Deutsches Elektronen-Synchrotron (DESY), Notkestrasse 85, D-22607 Hamburg, Germany*

[b] *Joint Institute for Nuclear Research, Dubna, 141980 Moscow Region, Russia*

[c] *Institute of Physics of the Polish Academy of Sciences, 02688 Warszawa, Poland*

Abstract

This paper presents the conceptual design of a high power radiation source with laser-like characteristics in the ultraviolet spectral range at the TESLA Test Facility (TTF). The concept is based on the generation of radiation in a regenerative FEL amplifier (RAFEL). The RAFEL described in this paper covers a wavelength range of 200–400 nm and provides 200 fs pulses with 2 mJ of optical energy per pulse. The linac operates at 1 % duty factor and the average output radiation power exceeds 100 W. The RAFEL will be driven by the spent electron beam leaving the soft X-ray FEL, thus providing minimal interference between these two devices. The RAFEL output radiation has the same time structure as the X-ray FEL and the UV pulses are naturally synchronized with the soft X-ray pulses from the TTF FEL. Therefore, it should be possible to achieve synchronization close to the duration of the radiation pulses (200 fs) for pump-probe techniques using either an UV pulse as a pump and soft X-ray pulse as a probe, or vice versa.

1. Introduction

Pump-probe techniques using either the soft X-ray pulse from the TTF FEL [1] as a pump and the visible-UV laser as a probe pulse, or vice versa, promise unprecedented insight into the dynamics of electronic excitations, chemical reactions and phase transitions of matter, from atoms, through organic and inorganic molecules and clusters, to surfaces,

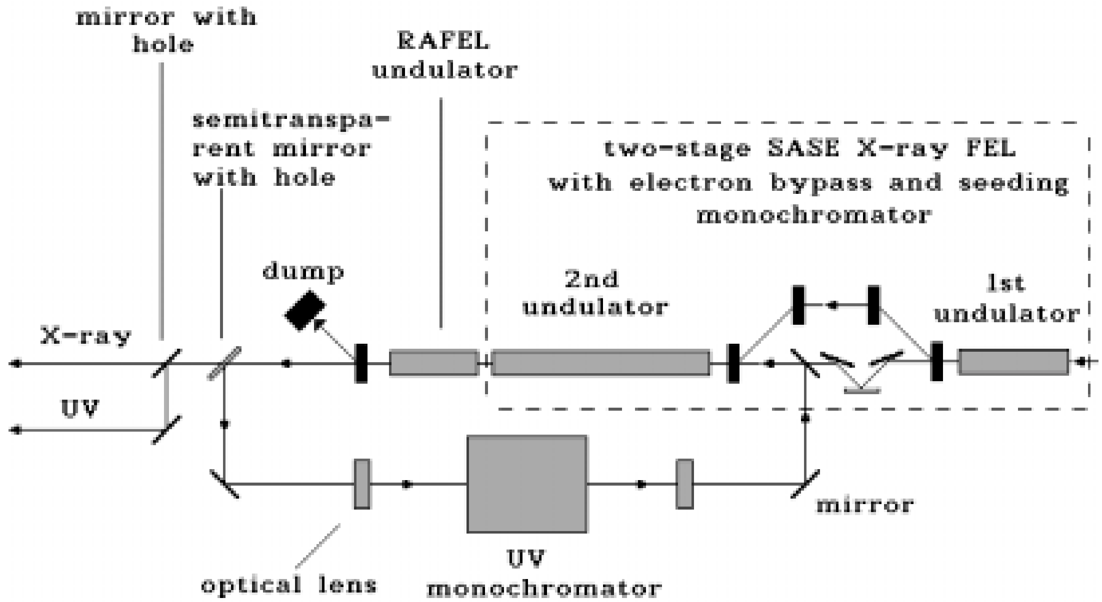

Fig. 1. Schematic layout of the pump-probe facility combining UV regenerative FEL amplifier and soft X-ray FEL at TTF

solids and plasmas. For applications in the visible and near-visible wavelength range a pump-probe facility based on a conventional quantum laser system will be available at the TTF [2]. The laser will provide in the visible spectral region between 750 and 900 nm a train of 150 fs pulses with 100 μJ of optical energy per pulse, at the same repetition rate as the X-ray FEL. The synchronization of the optical laser with the soft X-ray FEL pulses to within 200 fs is the most challenging task of this project. The main problem is the time jitter (± 1 ps) of electron bunches which are synchronous with the soft X-ray FEL pulses.

In this paper we describe the extension of the pump-probe facility into the ultraviolet wavelength range. Our approach is based on the idea to use a narrow band feedback between exit and entrance of a high gain FEL amplifier operating in multibunch mode (so called regenerative FEL amplifier – RAFEL [3]). Such a feedback can be realized in the UV wavelength range using mirrors, lenses, and a grating as a dispersive element. We propose to install an additional undulator after the soft X-ray FEL. A layout of the proposed RAFEL is shown in Fig. 1. This design makes use of the spent electron beam leaving the X-ray undulator. The SASE process in the X-ray FEL induces an additional energy spread in the electron beam. Nevertheless, the electron beam at the exit of the X-ray FEL is still a good "active medium" for an UV FEL amplifier. Because the RAFEL uses the spent electron beam, the proposed laser system operates in a "parasitic" mode not interfering with the main mode of the X-ray FEL operation. Since the X-ray and UV radiation pulses are generated by the same electron bunch, there is no problem of synchronization for pump-probe experiments with an accuracy close to the duration of the radiation pulses (200 fs). The RAFEL proposed here will provide intense, tunable and coherent radiation in the UV region of the spectrum between 200 and 400 nm as direct laser output. The RAFEL output radiation has the same pulse format as the X-ray FEL and produces 200 fs micropulses with 2 mJ of radiation energy per micropulse and transform-limited spectral width.

The RAFEL undulator and outcoupling optical system proposed can be installed in the unoccupied straight vacuum line used to transfer the X-ray beam to the experimental area, behind the dipole magnet separating the electron beam from the X-ray beam. The installation of the feedback is greatly facilitated by the fact that there is free space available for the input optical system. In order to get fully coherent X-ray radiation, a seeding option will be implemented into the X-ray FEL under construction at DESY [4]. The X-ray FEL seeding option consists of an additional 18 m long undulator, an electron bypass and X-ray grazing incidence monochromator (see Fig. 1). The electron bypass is necessary to delay the electron beam by the same amount as the X ray photon beam is delayed by the X-ray monochromator. The magnetic chicane has to deflect the electron beam out of the straight flight pass to make room for the X-ray monochromator and input optical elements of RAFEL.

2. Facility description

The RAFEL parameters are presented in Table 1. The RAFEL operates as follows. The first bunch in a train of up to 7200 bunches amplifies shot noise and produces intense, but wide-band radiation. A fraction of the radiation is back-reflected by a semi-transparent output coupling mirror. The spherical grating which is installed in the straight section of the feedback loop, disperses the light and focuses a narrow band of radiation back on the entrance of the undulator. The bandwidth of the feedback is chosen to produce a photon pulse length about ten times as long as the electron bunch length in order to avoid effects from a ± 1 ps time jitter (see Fig. 2). This requires a resolving power $\lambda/\Delta\lambda \simeq 6000$ at $\lambda = 200$ nm (photon pulse duration at the monochromator exit $l_{\mathrm{ph}} \simeq \lambda^2/(c\Delta\lambda) \simeq 4$ ps).

After the undulator the electron and the radiation beams are separated. The electron beam is guided into the beam dump and the radiation enters the output coupling system. The distance between the feedback outcoupling mirror and the exit of the RAFEL undulator is 20 m, the distance between the mirror and the exit of the X-ray FEL undulator is about 27 m. At a diameter of the hole in the mirror of 3 mm the fraction of the X-ray power directed through the mirror is close to 100%. This mirror is semi-transparent for the UV radiation, and approximately 50% of the UV radiation power is transmitted through it and delivered to the experimental area. Calculations show that an alignment accuracy of about 10 μrad is sufficient for reliable operation of the optical feedback.

The monochromator for the RAFEL should be able to select any wavelength between 200 and 400 nm. We adopted the Namioka scheme where tuning of the wavelength is

Table 1
Parameters of the UV pump-probe facility (RAFEL option)

Electron beam	
energy	1000 MeV
charge per bunch	1 nC
rms bunch length	50 μm
rms emittance	2 π mm mrad $/\gamma$
rms energy spread	2.5 MeV
number of bunches	7200/train
bunch spacing	111 ns
repetition rate	10 Hz
Undulator	
type	Planar
period	7 cm
peak magnetic field	1–1.4 T
number of periods	85
Output radiation	
wavelength	200–400 nm
bandwidth	Transform-limited
micropulse duration	200 fs
micropulse energy	2 mJ

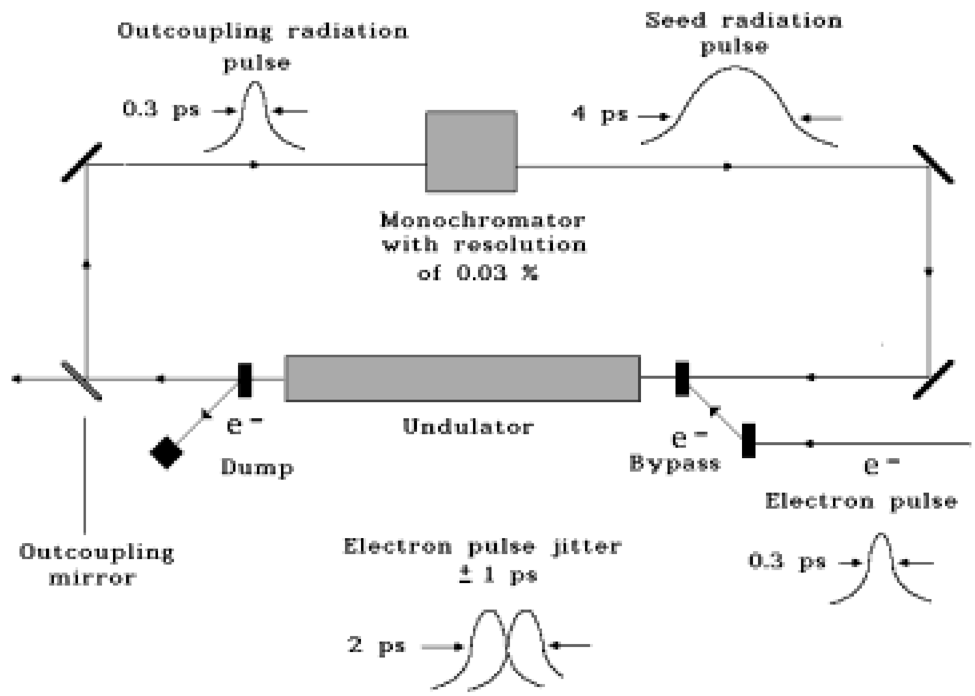

Fig. 2. The use of a monochromator as a pulse stretcher. Drawing illustrates how electron pulse jitter effects on the feedback system can be avoided

performed by means of rotation of the grating, while entrance and exit slits are fixed. Commercially available holographic gratings allow one to focus the image of the entrance slit exactly on the exit slit at small values of coma and astigmatism in the 200–400 nm wavelength band. The feedback transmission factor can be written as $T_{\mathrm{fb}} = K_{\mathrm{coupl}} \times R_{\mathrm{loss}}$, where K_{coupl} is the fraction of output radiation coupled out through the semi-transparent mirror, R_{loss} refers to the losses in the optical elements (mirrors, lenses, grating) of the feedback system. In addition, the grating reduces the peak power of the coherent signal further since it stretches the pulse longitudinally by a factor $\lambda^2/(\sigma_z \Delta\lambda)$ [5].

In the present design the lateral size of the photon beam focus, w, is completely determined by the fixed geometry of the feedback optical system (i.e. the focal distances of the mirrors and the aperture of the X ray undulator vacuum chamber). In our numerical example for 400 nm wavelength the size of the photon beam focus is about $w \simeq 800$ μm, which is about 15 times larger than the rms electron beam size, σ. Such a mismatch, however, is not dramatic and will result in a reduction of the gain by a factor of about 3 only (see section 3 for more details). Taking into account all the effects mentioned above, the overall loss factor for the feedback system is about 2×10^{-2}. When the power gain in the undulator, G, exceeds the relative losses of power in the optical feedback system, the output radiation power begins to grow, i.e. lasing takes place.

The undulator is one of the central components of the RAFEL. The values of the peak field and the period length are given in Table 1. The required field strength can be achieved using a hybrid configuration. At a gap of 12 mm, a peak field up to 1.5 T is feasible for the undulator period of $\lambda_{\mathrm{u}} = 7$ cm. This is more than needed for the RAFEL undulator. To minimize the length of the matching section between the VUV/X-ray undulator and RAFEL undulator, we decided to use the same value of the beta function of 3 meters. It is shown in section 3 that the maximum value of the gain well exceeds the relative losses of peak power in the optical feedback system when the undulator is at least 6 m long. The wavelength can be tuned continuously by changing the undulator magnetic field and adjusting the monochromator wavelength by simple rotation of the grating. Using the present design it should be possible to cover the range from 200 nm down to 400 nm.

3. Operation of the RAFEL

The main physical effects defining the operation of the FEL amplifier are the diffraction effects and the space charge effects. The longitudinal velocity spread was calculated using actual energy distribution in the electron beam after leaving the VUV/X-ray undulator (see Fig. 3). It is seen that the distribution function of the electrons can be fitted well by a Gaussian distribution with the rms deviation $\sigma_{\mathrm{E}} \simeq 2.5$ MeV. The energy spread does not influence too much the gain at chosen parameters (the power gain length is increased by 20% only with respect to the case of a "cold" electron beam). Calculations of the total power gain must take into account the details of focusing of the external radiation on the electron beam at the undulator entrance. A quantitative description may be performed in the following way. We assume that the seed radiation has a Gaussian radial intensity distribution which is characterized by the position of the focus, z_0, and the size of the waist in the focus, w. In the high-gain linear (steady-state) regime the radiation power grows exponentially with the undulator length:

$$G = P_{\mathrm{out}}/P_{\mathrm{in}} = A \exp[z/L_{\mathrm{g}}] \ ,$$

where P_{out} and P_{in} is the output and input power, respectively. The input coupling factor A depends on the focusing of the seed radiation and is a function of z_0 and w. It should

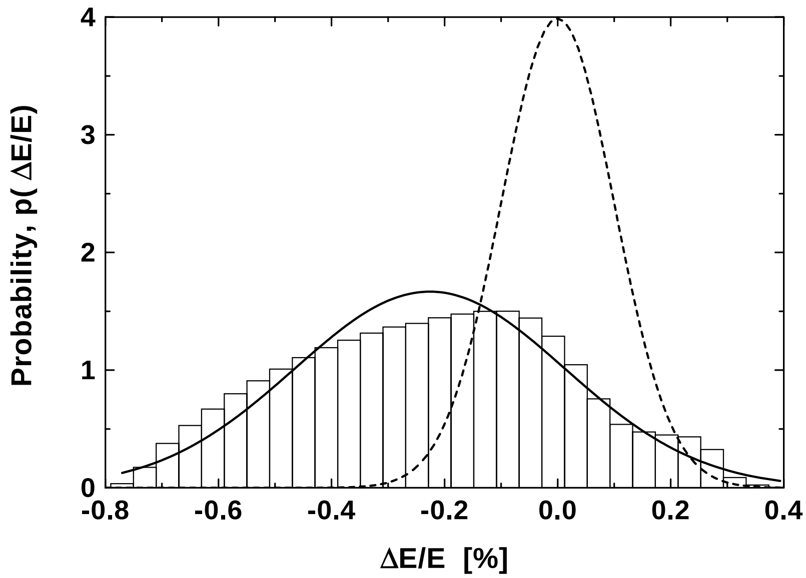

Fig. 3. Histogram of energy distribution of the particles after leaving the VUV/X-ray FEL driven by 1 GeV electron beam. The solid line represents a Gaussian distribution with the rms deviation σ_{E} = 2.5 MeV. The dashed line is the energy distribution at the entrance of the VUV/X-ray undulator (σ_{E} = 1 MeV)

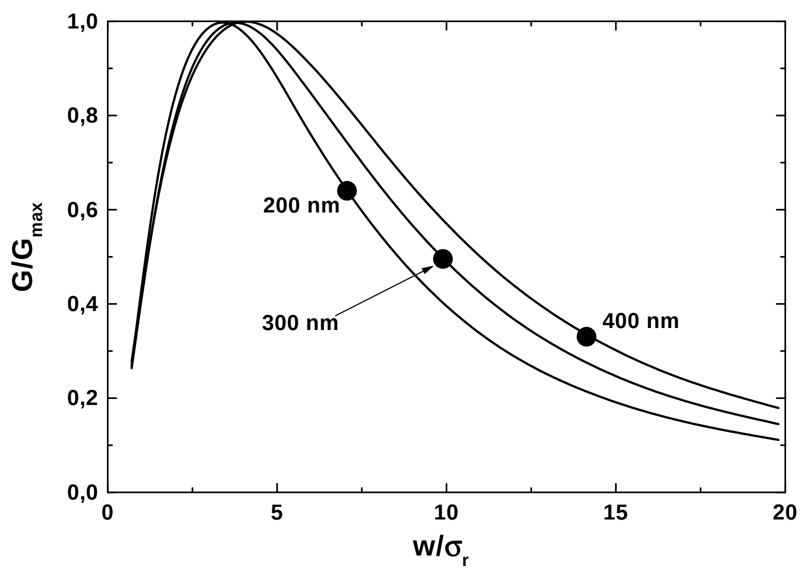

Fig. 4. Power gain in the linear regime versus spot size of the seeding radiation beam (the rms transverse size of the electron beam is σ_{r} = 55 μm)

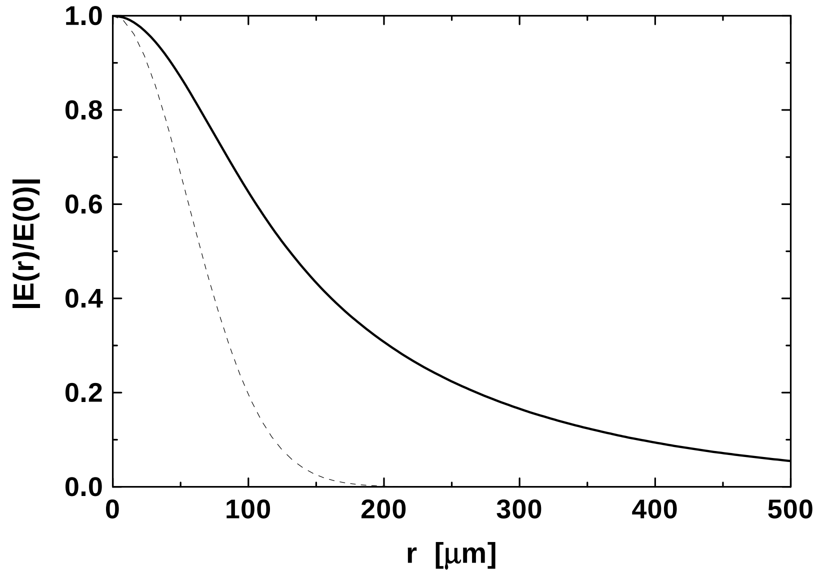

Fig. 5. Transverse distribution of the radiation field amplitude for the FEL amplifier operating at a wavelength of 200 nm. The dashed line is the transverse profile of the electron beam current density, $\exp[-r^2/(2\sigma_{\mathrm{r}}^2)]$ with $\sigma_{\mathrm{r}} = 55$ μm

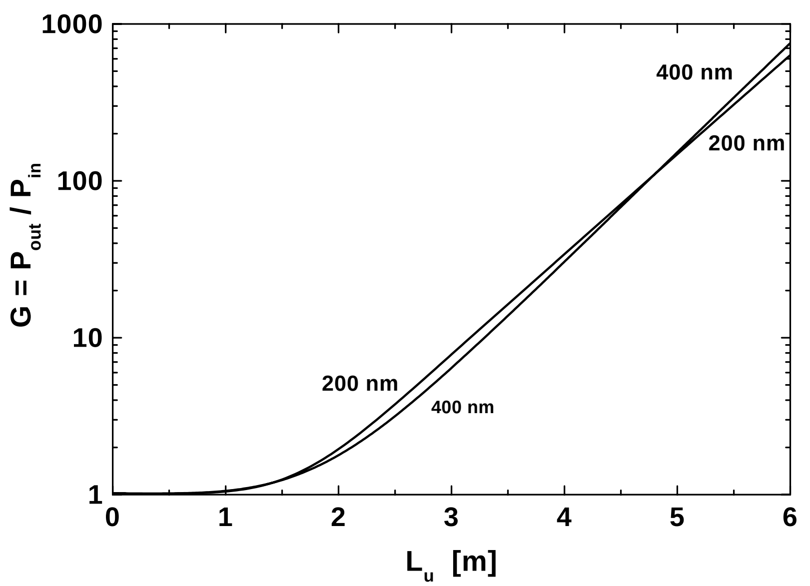

Fig. 6. Power gain, $G = P_{\mathrm{out}}/P_{\mathrm{in}}$ versus undulator length for the FEL amplifier operating at 200 and 400 nm wavelength (radiation beam size at the undulator entrance w is equal to 400 and 800 μm, respectively

be maximized by an appropriate choice of w and z_0. This problem has been studied in detail in [8] using the solution of the initial-value problem. It has been found that the value of A at $z_0 = 0$ does not differ significantly from its maximal value and the position of the Gaussian beam waist can be placed at the coordinate of the undulator entrance.

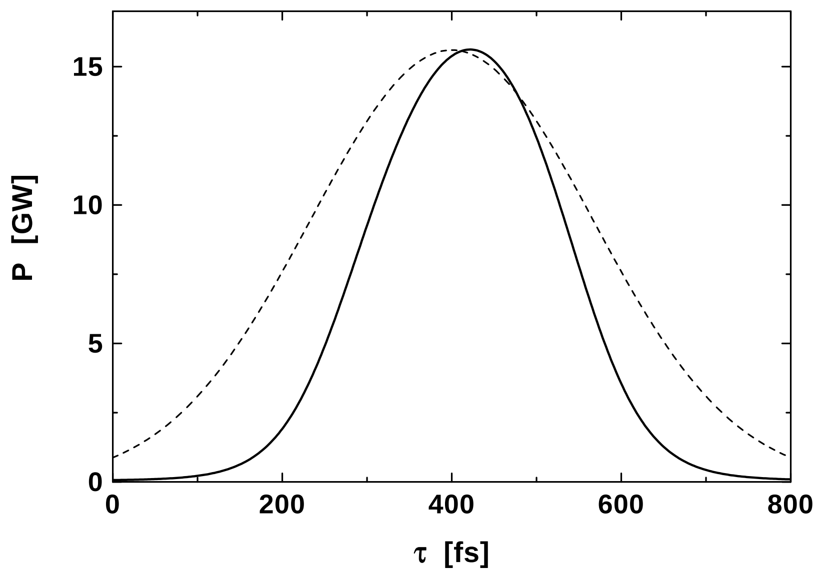

Fig. 7. Temporal structure of the radiation pulse at the exit of the RAFEL undulator. The dotted line represents the longitudinal profile of the electron beam current (the maximum corresponds to 2.5 kA)

However, due to the constraints of the present design we have no possibility to achieve the optimal value. The reason for this is that the focusing mirror can only be placed at a fixed position of 20 meters apart from the RAFEL undulator entrance. Also, there is an aperture limitation of 9 mm due to the diameter of the vacuum chamber in the VUV/X-ray undulator. Fortunately, this does not lead to significant degradation of the gain as it is illustrated in Fig. 4. The reason for this is the strong influence of diffraction effects. In the general case the seeding radiation should be matched with the beam radiation mode, but not with the transverse size of the electron beam. In the case of small diffraction parameter [8], the transverse size is larger than the transverse size of the electron beam as it is illustrated in Fig. 5.

Figure 6 presents the plots for the power gain versus undulator length for the FEL amplifier operating in the linear regime at 200 and 400 nm wavelength. It is seen that the gain only slightly depends on the wavelength for an undulator length of 6 meters. On the one hand, the focusing of radiation becomes less optimal at increasing wavelength (see Fig. 4). On the other hand, the power gain length decreases with the increase of the wavelength. At a relatively short undulator length these two effects compensate each other.

The final optimization of the FEL amplifier parameters has been performed with the nonlinear, three dimensional, time-dependent simulation code FAST [7]. The optimized parameters of the FEL amplifier are presented in Table 1. Figure 7 shows the time structure of the radiation pulse at the exit of the undulator. We obtain that the RAFEL operating at saturation produces 4 mJ pulses of about 200 fs pulse duration.

The analysis of the RAFEL parameters has shown that it will operate reliably even at a value of the energy spread exceeding the project value for the TTF by a factor of two. There is also a safety margin (by a factor of two) with respect to the value of the emittance.

Acknowledgments

We thank D. Trines and J.R. Schneider for their interest in this work and their support.

References

[1] J. Rossbach, Nucl. Instrum. and Methods A 375(1996)269

[2] "Development of a pump-probe facility combining a high-power optical laser and a soft X-ray FEL": Proposal. Available at DESY by request only

[3] J. Goldstein, D. Nguyen and R. Sheffield, Nucl. Instrum. and Methods **A393**(1997)137

[4] "Seeding Option for the VUV Free Electron Laser at DESY": Proposal. Available at DESY by request only

[5] J. Sollid et al., Nucl. Instrum. and Methods **A285**(1989)147

[6] B. Faatz et. al., Nucl. Instrum. and Methods A 429(1999)424

[7] E. L. Saldin, E. A. Schneidmiller, and M.V. Yurkov, Nucl. Instrum. and Methods A 429(1999)233

[8] E. L. Saldin, E. A. Schneidmiller, and M.V. Yurkov, "The Physics of Free Electron Lasers" (Shpringer-Verlag, Berlin-Heidelberg-New-York, 1999)

Photon Diagnostics for the study of Electron Beam Properties of a VUV SASE-FEL

Ch. Gerth [1], B. Faatz, T. Lokajczyk [2], R. Treusch, J. Feldhaus

Deutsches Elektronen-Synchrotron DESY, Notkestr. 85, D-22603 Hamburg, Germany

---

Abstract

A single-pass free-electron laser operating in the self-amplified spontaneous-emission (SASE) mode at around 100 nm is currently under test at the TESLA Test Facility at DESY. After first observation of SASE in February 2000, the photon beam has been characterized by different techniques. We present the methods of VUV photon diagnostics that were used to measure the spectral and angular distribution of the photon beam and the effect of the electron beam parameters on these properties. The angular and spectral distribution of the FEL radiation are particularly sensitive to the electron orbit in the undulator, and we indicate ways of on-line photon beam diagnostics to enhance the electron beam quality and the FEL gain.

---

1. Introduction

The TESLA collaboration is currently developing a Free-Electron Laser (FEL) at the TESLA Test Facility (TTF) at DESY. The FEL is based on the principle of self-amplified spontaneous emission (SASE) and operates in the Vacuum Ultraviolet (VUV) energy region [1]. In the SASE process, coherent radiation is emitted by a high-current, low-emittance electron beam during a single pass through a high-precision undulator. The spontaneous radiation emitted in the first part of the undulator overlaps and interacts with the electron bunch and amplifies the power and coherence of the radiation. Since the early theoretical work on the SASE process [2–5], considerable theoretical and experimental efforts have been made to study the physics of SASE. Experimental evidence of SASE in the infrared region 5–16 μm has been reported recently by several groups [6–8] with FEL gains up to 10^5 [9]. Efforts in reducing the wavelength to the visible began with Babzien *et al.* [10] who observed SASE at 633 nm, and FEL operation in the SASE mode at 530 nm was demonstrated by Milton *et al.* [11]. A decisive milestone on the way to Å

[1] Corresponding author. Tel.: +49-40-8998-2179; fax: +49-40-8998-4475.
E-mail address: Christopher.Gerth@desy.de (Ch. Gerth)
[2] Present address: debis Systemhaus, Dortmund, Germany

wavelengths has been achieved in February 2000 when the first FEL output in SASE mode at around 100 nm was observed at the TTF [12]. In none of the experiments saturation has been reached, and the requirements for SASE at still shorter wavelengths are increasingly demanding in terms of electron beam quality and steering through the undulator. In this paper, we report on the VUV photon diagnostics used at the TTF FEL for the determination of the spectral and angular distribution of the photon beam at around 100 nm and indicate ways of studying the electron beam properties in order to enhance the beam quality.

2. VUV photon diagnostics

For the complete characterization of the FEL photon beam properties, an experimental station for photon diagnostics, including a grating monochromator and various detectors, provides all the instrumentation necessary to measure the photon pulse intensity and its angular, spectral and temporal distribution. New detection concepts have been employed in order to measure all SASE specific properties on a single pulse basis. The detectors and the principle layout of the photon diagnostics unit have been described in detail in Ref. [13].

FEL photon diagnostics is particularly challenging in the VUV region. Due to the high absorbance of radiation below 200 nm by any material, neither window materials to outcouple the radiation nor attenuating filters are available. Thus, in order to cover the full dynamic range of intensity from spontaneous undulator emission to SASE in saturation (about 5 orders of magnitude), different types of detectors, suitable for operation under ultra-high-vacuum (UHV) conditions, are employed. Since the photon diagnostics cannot be separated from the undulator and the accelerator vacuum, all components were assembled under cleanroom conditions. This avoids dust particles which could migrate to the accelerator cavities. In addition, all devices are fully remote controlled because radiation background in the accelerator tunnel prevents access during operation.

3. Spectral distribution

For the determination of the spectral distribution, the photon beam is deflected by a plane mirror onto the entrance slit of a commercial 1m normal-incidence monochromator. The width of the entrance slit can be varied by a precise piezo actuator from 1 to 195 μm. For the initial FEL commissioning phase, the monochromator has been equipped with a 1200 lines/mm spherical grating. Spectra of the dispersed FEL radiation are recorded by a thinned, back-illuminated UV-sensitive CCD [14] that has been placed in the focal plane of the spherical grating, attached directly to the monochromator vacuum.

The upper part of Fig. 1 presents an image of the dispersed FEL radiation with an acquisition time of 30 s. The FEL was operated in single-bunch mode with 1 Hz repetition rate. Despite a 20 cm lead shielding of the camera, the background radiation in the accelerator tunnel caused a noticeable pixel damage and, therefore, a background image had to be subtracted and a median filter was applied. The horizontal (x-) axis of the image corresponds to the dispersive direction and the vertical (y-) axis is parallel to the entrance slit. The full CCD image covers a wavelength range of 20 nm in the dispersive direction. The intensity distribution in y-direction reflects the vertical beam profile and is mainly defined by a 5-mm-diameter aperture in front of the monochromator.

The spectral distribution, integrated in the vertical direction, is depicted in the lower part of Fig. 1. The wavelength scale has been calibrated with the use of a hollow-cathode lamp [15] and a Hg-lamp. The spectral distribution of the FEL radiation is centered at 92.1 nm with a full-width at half-maximum (FWHM) of 0.74 nm.

When an electron beam passes through a planar undulator, it emits electro-magnetic radiation at the wavelength

$$\lambda_{ph} = \frac{\lambda_u}{2\gamma^2}\left(1 + \frac{K^2}{2}\right), \tag{1}$$

where $\gamma = E_e/mc^2$ is the relativistic factor of the electrons and $K = eB_u\lambda_u/2\pi m_e c$ the undulator parameter with the peak magnetic field B_u and the undulator period λ_u. The FEL at the TTF (phase I) consists of three fixed-gap undulator modules with a length of 4.5 m each; the wavelength λ_{ph} of the FEL radiation can be varied by changing the electron beam energy E_e. Since K and λ_u are precisely known (see Table 1), the electron beam energy can be determined from the measured wavelength. The determination of the absolute wavelength can be achieved with an accuracy of 0.5 %; this results in an accuracy of 0.25 % for the electron energy. For instance, the spectrum of Fig. 1 centered at 92.1(5) nm corresponds to an electron beam energy of 254(1) MeV. This value is in good agreement with an energy of 250(5) MeV determined from the deflection of the electron beam by a bending magnet. Meanwhile SASE has been observed between 80 and 181 nm at the TTF-FEL. The corresponding parameters are summarized in Table 1.

A series of three single-pulse spectra, centered at around 110 nm, is shown in Fig. 2(a). Each spectrum represents the spectral distribution of the FEL radiation emitted by a single bunch. The spectra were taken subsequently in intervals of several seconds with a slit width of 195 μm which results in an instrumental bandwidth of 0.17 nm. The variation of the centre position of the spectra reflects the energy variation of the electron beam. Here, the shift of 0.2 nm (0.2%) corresponds to an energy jitter of the electron beam of 0.1% [see Eq. (1)]. Fig. 2(b) depicts a spectrum which was accumulated during an interval of 30 s, i.e., this spectrum represents the spectral distribution averaged over 30 subsequent electron bunches. As a consequence of the energy jitter, the width of the spectrum of 1.1 nm (FWHM) is larger than the 0.8 nm (FWHM) for each of the single-bunch spectra [Fig. 2(a)]. The shoulder at the long wavelength side is possibly caused by a fraction of electrons within the bunch with slightly smaller energy.

The minimal interval between two single-pulse spectra is limited by the readout time (8 s) of the CCD camera. To overcome this restriction, the back-illuminated CCD camera has been replaced by an intensified CCD camera [16] with a readout time of 125 ms. It utilizes a fast fluorescent screen in the focal plane of the monochromator which is imaged through a Suprasil viewport. The ICCD camera is equipped with a micro-channel-plate (MCP) as an intensifier which operates as a fast shutter with exposure times down to 5 ns. This enables one to select single pulses from a sequence of pulses and to study, e.g., the variation of electron beam parameters within a bunchtrain. Furthermore, with photon beam intensities expected for the FEL close to saturation, the fine structure in the spectral distribution[17], which stems from the startup from shot noise in the SASE process, can be studied. A 3600 lines/mm grating in conjunction with an 10 μm entrance slit results in a resolving power of $E/\Delta E = 2\times10^4$ at $\lambda = 120$ nm, which is sufficient to fully resolve the fine structure. The parameters of the back-illuminated and the intensified CCD camera are compared in Table 2.

4. Angular distribution

The vertical photon beam profile, recorded at a distance of about 12 m behind the undulator, is shown in the upper part of Fig. 3. A 10 x 10 mm^2 PtSi-photodiode [20] with a 1-mm-diameter spherical aperture in front was moved in steps of 1 mm through the photon beam [3], and for each step the signal of

[3] For further details on the diode and beam profile recording see Ref. [21]

5 subsequent pulses was accumulated; the FEL was operated in single-bunch mode with 1 Hz repetition rate. The solid line represents a fit of a Gaussian profile with a width of 7.7(7) mm (FWHM) and a centre at a vertical position of 3.6(3) mm. The zero position of the detector coordinate system has been aligned to the centre axis of the undulator with an accuracy of ± 0.5mm with the use of a theodolite. Similar vertical displacements of the photon beam have been observed on the CCD image of the normal-incidence spectrometer, depending on the steering of the electron beam into the undulator. Obviously the direction of the electron beam in the gain region can be varied by a few 10^{-4} radian without much change in gain such that the light is emitted into different directions. This has been corroborated by using steerers (corrector coils) along the last undulator module to deflect the electron beam only in this area. Starting from the situation of a vertically displaced beam with all steerers turned off (Fig. 3, top), it was possible to deflect the electron beam down using five steerers such that the centre of the FEL radiation moved to the nominal zero position (Fig. 3, bottom). Again, in this case the light intensity did not change significantly. These results suggest that the on-line observation of the photon beam position might be very useful as a monitor when the electron beam orbit is adjusted, e.g. using beam based alignment techniques.

As in the case of the spectral distribution, the photon beam profile shown in Fig. 3 is most probably broadened by a spatial and angular jitter of the electron beam in the undulator. Hence, single-pulse measurements are required to avoid such a superposition. In a first approach, the fluorescent light of different crystals, such as Ce:YAG and $PbWO_4$, has been imaged with a conventional CCD camera. Using crystals with fast decay channels in conjunction with a gated ICCD camera it will be possible to observe the intensity distribution of single FEL pulses.

5. Summary

The methods used for the determination of the spectral and angular distribution of the VUV radiation generated by the SASE-FEL at the TESLA Test Facility at DESY and a selection of characteristic results have been presented. The angular and spectral distribution of the FEL radiation are particularly sensitive to the electron beam energy and orbit in the undulator. These techniques can therefore be used as on-line diagnostics of electron beam parameters and are promising tools to enhance the electron beam quality and, thus, the FEL gain.

Acknowledgements

The authors are indebted to all members of the TESLA collaboration for their contributions to the TTF at DESY and for successfull operation of the FEL. A list of the participating institutes can be found in Ref. [12].

References

[1] A VUV Free Electron Laser at the TESLA Test Facility at DESY, Conceptual Design Report, DESY Print, June 1995, TESLA-FEL 95-03; J. Roßbach, Nucl. Instr. and Meth. A **375** (1996) 269.

[2] A.M. Kondratenko, E.L. Saldin, Part. Acc. **10** (1980) 207.

[3] Ya.S. Derbenev, A.M. Kondratenko, E.L. Saldin, Nucl. Instrum. and Meth. **193** (1982) 415.

[4] R. Bonifacio, C. Pellegrini, L.M. Narducci, Opt. Commun. **50** (1984) 373.

[5] C. Pellegrini, J. Opt. Soc. Am. **52** (1985) 259.

[6] R. Prazeres, J.M. Ortega, F. Glotin, D.A. Jaroszynski, O. Marcouillé, Phys. Rev. Lett. **78** (1997) 2124.

[7] M. Hogan, C. Pellegrini, J. Rosenzweig, A. Varfolomeev, S. Anderson, K. Bishofberger, P. Frigola, A. Murokh, N. Osmanov, S. Reiche, A. Tremaine, Phys. Rev. Lett. **81** (1998) 289.

[8] D.C. Nguyen, R.L. Sheffield, C.M. Fortgang, J.C. Goldstein, J.M. Kinross-Wright, N.A. Ebrahim, Phys. Rev. Lett. **81** (1998) 810.

[9] M.J. Hogan, C. Pellegrini, J. Rosenzweig, S. Anderson, P. Frigola, A. Tremaine, C. Fortgang, D.C. Nguyen, R.L. Sheffield, J. Kinross-Wright, A. Varfolomeev, A.A. Varfolomeev, S. Tolmachev, Phys. Rev. Lett. **81** (1998) 4867.

[10] M. Babzien, I. Ben-Zvi, P. Catravas, J.-M. Fang, T.C. Marshall, X.J. Wang, J.S. Wurtele, V. Yakimenko, L.H. Yu, Phys. Rev. E **57** (1998) 6093.

[11] S.V. Milton *et al.*, Phys. Rev. Lett. **85** (2000) 988.

[12] J. Andruszkow *et al.*, Phys. Rev. Lett. in print.

[13] R. Treusch, T. Lokajczyk, W. Xu, U. Jastrow, U. Hahn, L. Bittner, J. Feldhaus, Nucl. Instrum. and Meth. A **445** (2000) 456.

[14] CCD camera system ATC 300 L from Photometrics, Tucson, Arizona 85706.

[15] K. Danzmann, M. Günther, J. Fischer, M. Kock, M. Kühne, Appl. Opt. **27** (1988) 4947; see http://www.pmp.uni-hannover.de/arbeitsgruppen/Gruppe-Kock/Kock_Gruppe_engl.html

[16] CCD camera Nanostar S25 from LaVision, Göttingen, Germany; see http://www.lavision.de/cameras/index2.htm.

[17] E.L. Saldin, E.A. Schneidmiller, M.V. Yurkow, Opt. Commun. **148** (1998) 383.

[18] J. Pflüger, Nucl. Instrum. and Meth. A **445** (2000) 366.

[19] P. Castro, B. Faatz, K. Flöttmann, Nucl. Instrum. and Meth. A **427** (1999) 12.

[20] K. Solt, H. Melchior, U. Kroth, P. Kuschnerus, V. Persch, H. Rabus, M. Richter, and G. Ulm, Appl. Phys. Lett. **69** (1996) 3662.

[21] R. Treusch, Ch. Gerth, T. Lokajczyk, J. Feldhaus, Proceedings of 7^{th} International Conference on Synchrotron Radiation and Instrumentation 2000, to be published in Nucl. Instrum. and Meth. A.

Table 1
Measured parameters of the SASE-FEL at the TESLA Test Facility (phase I) at DESY (August 2000).

Parameter	
Photon beam	
Wavelength λ_{ph}	181 nm – 80 nm
Energy	7 eV – 15 eV
Angular divergence at 91 nm	0.7(3) mrad (FWHM)
FEL gain [a]	1–9 10^3
Undulator	
Length	13.5 m
Gap	12 mm
Period λ_u	27.3 mm
Peak Magnetic Field B_u	0.497 T
Electron beam	
Energy	181 MeV – 272 MeV
No. of Bunches per Bunchtrain	1 – 10
Bunch Separation	1 μs
Repetition Rate	1 Hz

[a] see Ref. [12]

Table 2
Parameters of the back-illuminated and the intensified CCD cameras.

	Photometrics ATC 300L	LaVision Nano Star 25
Principle	back-illuminated thinned CCD	Fluorescence screen, Optics 1:2.17, MCP
No. of pixels	1024 x 1024	1280 x 1024
Pixel size	24 μm	6.7 μm
A/D converter	16 Bit @ 0.2 MHz	12 Bit @ 12.5 MHz
Shutter	mechanical	MCP
Readout time	8 s	125 ms
Min. exposure time	1 ms	5 ns
Resolution	24 μm	$\approx 12\mu$m

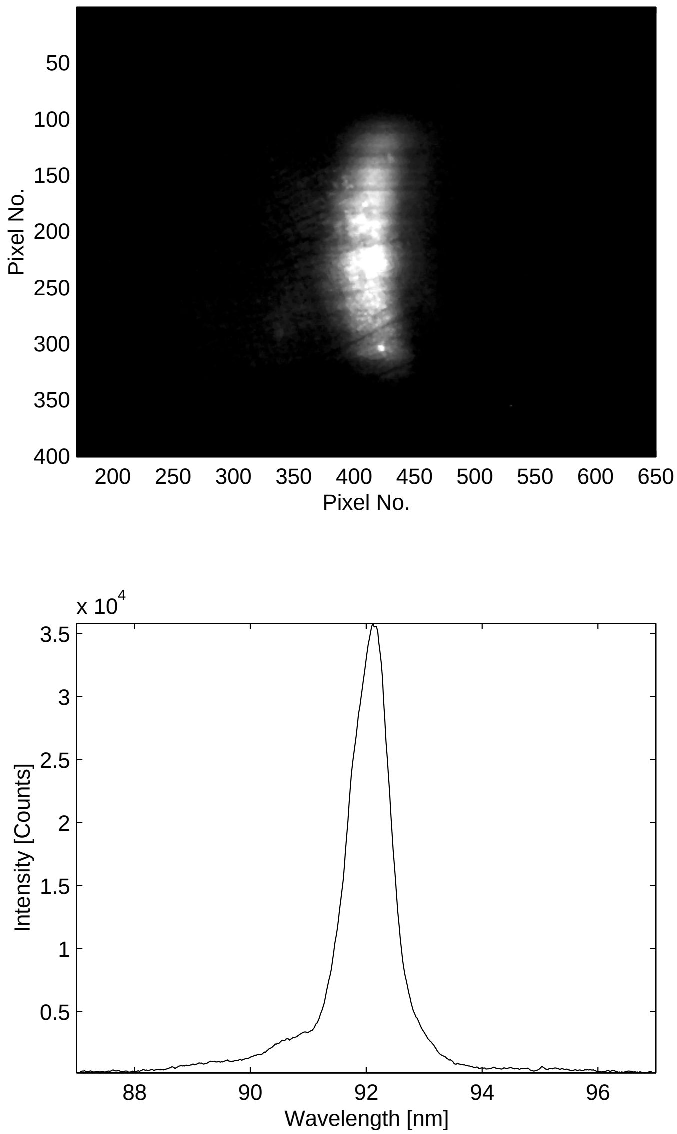

Fig. 1. Upper part: CCD image of the dispersed FEL radiation in SASE mode taken in the focal plane of a 1 m normal-incidence monochromator. Lower Part: Spectral distribution obtained by integration of the image above in vertical direction.

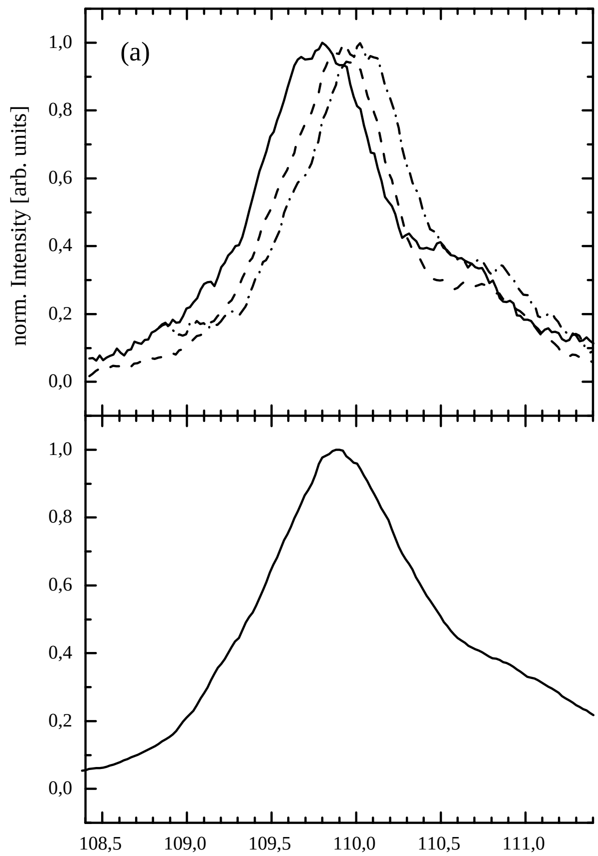

Fig. 2. (a) Series of single-pulse spectra; (b) spectrum of 30 pulses.

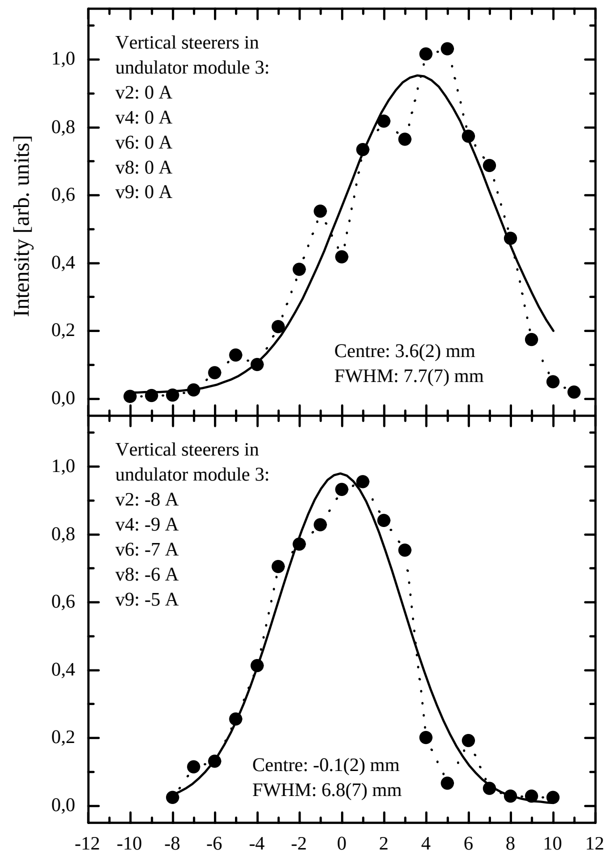

Fig. 3. Vertical beam profile of FEL radiation in SASE mode at 91 nm; (a) without and (b) with the effect of vertical electron beam steerers v2–v9 in the last undulator module.

Observation of Longitudinal Phase Space Fragmentation at the TESLA Test Facility Free-Electron Laser

M. Huening [a] Ph. Piot [a,1] H. Schlarb [a]

[a] *Deutsches Elektronen-Synchrotron, D–22603 Hamburg, Germany*

Abstract

It has been reproducibly observed that the energy distribution of the beam, when fully longitudinally compressed for SASE operation, breaks up into several peaks. In this paper a description of the experimental setup, beam operating conditions, and observations is presented to enable further theoretical studies of this effect.

1. Introduction: Longitudinal beam dynamics at TTF

A schematics of the Tesla Test Facility (TTF) FEL [1] is depicted in Fig. 1. We shall only concentrate on the longitudinal phase space manipulation since the measurements reported hereafter only pertain to this plane: the beam generation line consists of an L-band radio-frequency (RF) photoinjector coupled to a TESLA-type superconducting accelerating cavity that boosts the beam up to 17MeV. The photocathode drive-laser is gaussian-shaped with an rms time duration of 8ps approximately. The electron bunch then enters an accelerating section (Acc. #1)that consists of eight TESLA-type superconducting cavities. The injection phase of the beam in this latter accelerating section is chosen, under nominal operating conditions, to impart the proper time-energy correlation to compress the bunch using the downstream magnetic chicane-based compressor. The beam transport, downstream the bunch compressor, consists of a second accelerating section (Acc. #2, identical to Acc. #1), nominally operated for maximum energy gain,

[1] corresponding author: DESY, D–22603 Hamburg, Tel.: +49 40 8998 2755, e-mail: piot@sun52a.desy.de

followed by the undulator magnets section. Behind the undulator, the beam is separated from the FEL beam by a spectrometer dipole (that bends in the same plane as the compressor). The transfer line up to the dump is instrumented with several diagnostics which especially include a beam profile measurement station.
A detailed description of the magnetic compressor is presented in Reference [2]. During our measurement, the bending angle in the compressor was set to 19deg, which corresponds to a momentum compaction $R_{56} \simeq$-0.18m. This results in an optimum operating phase for the first accelerating section of -10RF-deg off-crest approximately. Because of the rather long bunch length at the injector front-end, typically 2.7mm (rms), the longitudinal phase space is strongly distorted via RF-induced curvature during its acceleration in Acc. #1. This distortion, impinges the compression process by limiting the minimum reachable bunch length to 0.5mm (rms) approximately (as inferred from multiparticle simulations and experimentally verified).

2. Experimental techniques

During our measurements we used the different beam profile monitors mentioned in Fig. 1: energy spread was measured using the optical transition radiation (OTR) viewers OTR1 and OTR/FLU3 (this latter viewer incorporates both an OTR radiator and a fluorescent screen). At the location of these two beam profile stations, the linear dispersion is estimated to R_{16} =0.31m (bunch compressor) and R_{16} =-1.15m (spectrometer) respectively. The nonlinear dispersion, T_{166}, is found, at both locations, to have no significant impact on the beam horizontal profile so that the horizontal coordinate of an electron, x, scales linearly (to first order) with its relative momentum offset, δ, following $x \simeq R_{16}\delta$. This latter scaling implicitly implies that the contribution from the pure betatron term is insignificant, a true assumption since, for all measurements presented in this paper, a set of upstream quadrupoles, located before the bunch compressor or the spectrometer dipole respectively, were tuned to minimize the horizontal beam spot at the observation point thereby asserting the beam spot was essentially dominated by the dispersive contribution. Based on the measurements of energy profiles at OTR/FLU3 for different phases of Acc. #2 a longitudinal tomography technique was implemented [3]. The method to recover the longitudinal phase-space is based on the MENT [4] (Maximum ENTropy) algorithm which computes the best estimate of the phase space density by maximizing its entropy. At the compressor exit the transverse beam density can also be measured using OTR2. At that point the dispersion was found not to be zero, we believe because of spurious dispersion generated by non-zero value of upstream correctors. The diagnostics package also include a bunch length monitor located downstream the second accelerating section. This device provides bunch length measurement by the mean of a sub-millimeter wave polarizing interferometry of coherent transition radiation [5] (CTR). We did not systematically measure the bunch length but rather assess whether the first accelerating section

(Acc. #1) was operated for maximum compression by simply "peaking" the CTR power detected by a pyroelectric detector. All the measurements reported in the following were performed with a charge per bunch of 1nC (within 10%), except when explicitely mentioned. The following observations are proved to be from single RF-bucket by using a streak camera setup.

3. Observations

Energy profiles versus incoming time-energy correlation: In this series of measurement the compressor is operated, and the bunch compression is varied by operating Acc. #1 at different phase to act on the incoming longitudinal phase space slope, $d\delta/ds$: at maximum compression it is related to the bunch compressor momentum compaction by relation $d\delta/ds = -1/R_{56}$. We found, using the CTR signal, that the maximum compression was occurring -10deg w.r.t. the maximum energy gain phase. For this operating conditions, the beam energy was about 135MeV at the bunch compressor location and 230MeV downstream Acc. #2. After each change of Acc. #1 phase, the phase of the Acc. #2 accelerating section was reset to maximize the energy at the machine front end. Fig. 2, depicts the evolution of the beam density recorded at the observation point (i.e. OTR/FLU3) for some phase of the Acc. #1. The maximum compression occurs at $\phi \simeq$-8deg [2] whereas the maximum energy gain through the whole linac is obtained for $\phi \simeq$+2deg. From Fig. 2 we conclude that when the time-energy induced correlation by Acc. #1 does not provide compression, i.e $\phi >$+2deg, the energy profile is as expected: it consists of a bright core with a long energy tail due to the RF-induced curvature because of the relative long incoming bunch. As the time-energy induced correlation allows compression, $\phi <$+2deg, the energy profile starts to show multiple fine structure which seems to separate into two main "islands" at maximum compression. Finally, in the over-compression regime, $\phi <$-8deg, these multiple structures start disappearing and are hardly observable at phases below -14deg.

Impact of the bunch compressor: For three cases (i) bunch compressor operated and accelerating section Acc. #1 operated for maximum compression, (ii) bunch compressor operated and Acc. #1 operated on-crest, and (iii) bunch compressor off with Acc. #1 operated approximately -10deg off-crest, we have investigated the evolution of the energy profile in the high energy spectrometer line for various phase of Acc. #2 ultimately to take tomographic data in order to recover the full longitudinal phase space density. The energy profiles for these three cases are presented in Fig. 3 (Acc. #2 was set for maximum energy gain). A structured energy profile, as the one presented previously, is observed only in the case when the linac operated in maximum compression mode. This feature,

[2] The phase value ϕ mentioned hereafter are arbitrary value read from the control system.

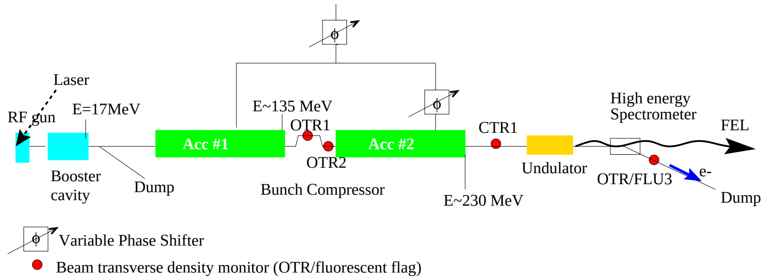

Fig. 1. Overview of the Tesla Test Facility Phase I.

which was also observed for other bunch charge, suggests the induced fragmentation of the energy profile is related to the compression process. At the bunch compressor exit, some structure can already be noticed by observing the beam transverse density at OTR2, but none was observable at OTR1. For the case (ii) the reconstructed longitudinal phase space at the compressor exit is shown in Fig. 4.

Charge-dependence To asses whether the observation could be attributed to collective effects, we also measured the energy distribution for bunch charge ranging from 0.5 to 4nC. The distribution shows no significant dependence on the charge, though the collective effects hypothesis cannot be ruled out: the charge was varied by changing the photocathode drive laser intensity, which impacts the bunch length: from multiparticle simulations we expect that an increase of the charge from 0.5 to 4nC, would double the bunch length (from 2 to 4mm (rms)) principally because of longitudinal space-charge force.

4. Summary

An anomalous “beam break up” of the longitudinal phase space has been observed at TTF-FEL when the linac is operated so that the bunch compression is maximized. A mechanism based on bunch self interaction via coherent synchrotron radiation is discussed in Reference [6].

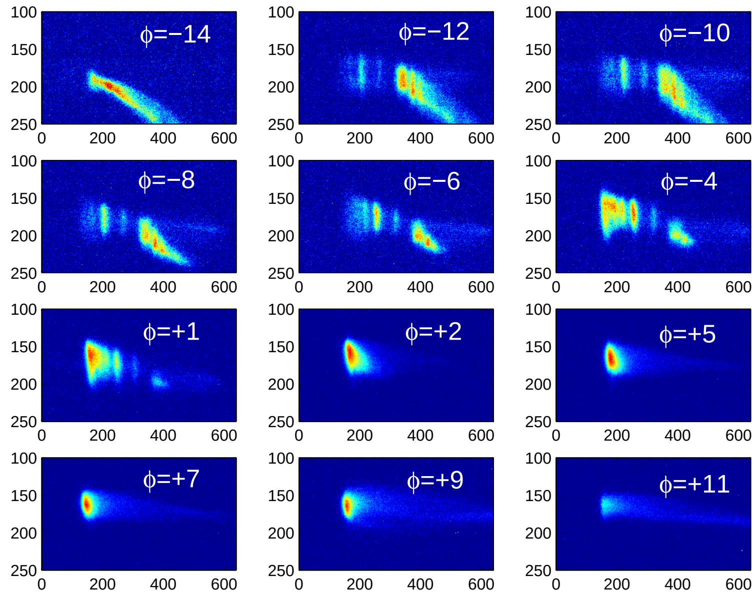

Fig. 2. Single bunch beam transverse density observed at the profile measurement station OTR/FLU3. These measurements were performed using the fluorescent screen.

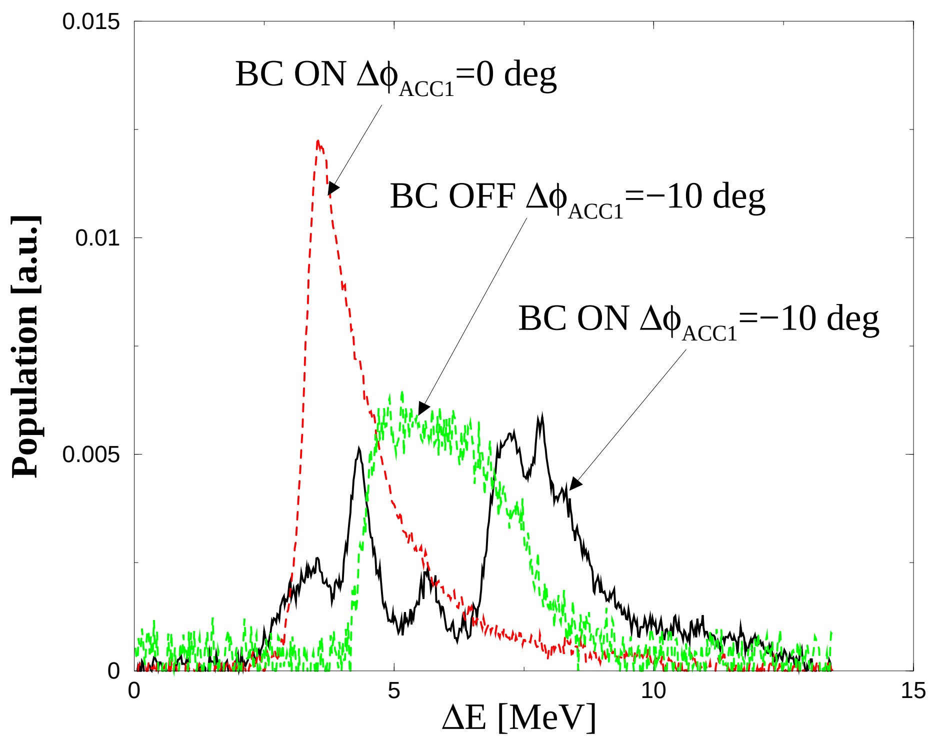

Fig. 3. Energy profile obtained for three different senarii of operation: bunch compressor ON with Acc. #1 on-crest ($\Delta\phi = 0$deg), and setup for minimum bunch length ($\Delta\phi = -10$deg), and bunch compressor OFF with $\Delta\phi = -10$deg.

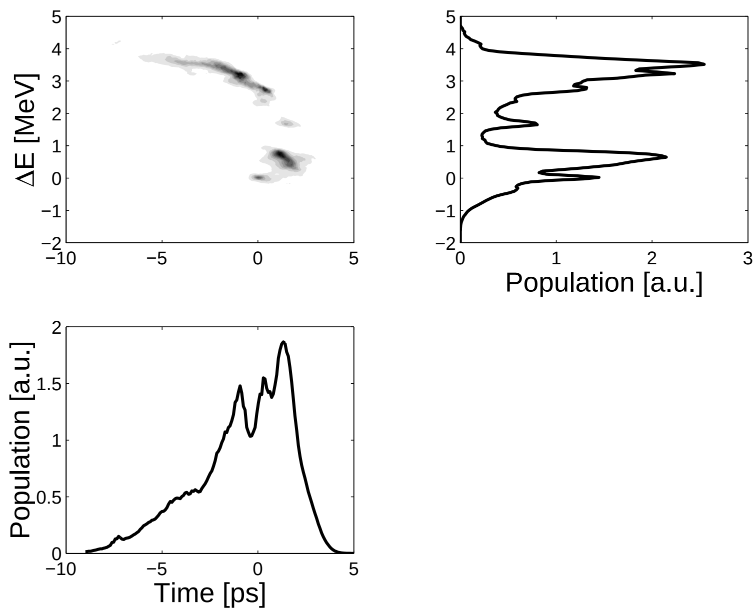

Fig. 4. Reconstructed longitudinal phase space downstream the bunch compressor **(top left)** and energy **(top right)** and time **(bottom)** charge density. (Time>0 correspond to the bunch head)

References

[1] Roßbach J., this conference

[2] Kabel A., et al., proceedings of 1999 part. accel. conf., IEEE catalog #0-7803-5573-3/99, pp. 2507-2509, (1999)

[3] Huening M., to be published

[4] Minerbo G., *Computer Graphics and Image Processing* vol. 10, p. 48 (1970)

[5] Geitz M., et al., proceedings of 1999 part. accel. conf., IEEE catalog #0-7803-5573-3/99, pp. 2174-2176, (1999)

[6] Limberg T., Piot Ph., and Schneidmiller E., this conference

An Analysis of Longitudinal Phase Space Fragmentation at the TESLA Test Facility

T. Limberg [a] , Ph. Piot [a] , E. A. Schneidmiller [a]

[a] *Deutsches Elektronen-Synchrotron, D–22603 Hamburg, Germany*

Abstract

It has been reproducibly observed that the energy profile of the fully longitudinally compressed TTF-FEL beam breaks up into peaks. In this paper we analyse a potential cause of this effect. We study the enhancement of bunch self-interaction via coherent synchrotron radiation (CSR), leading to a break-up of the longitudinal phase space. For our analysis, we use a simple model as well as the simulation code TraFiC[4] [1] to evaluate the CSR-induced effects.

1. Introduction

At the TTF-FEL in its present stage [2], a bunch of 2.7 mm length (RMS) is emitted from the gun, accelerated by a capture cavity and the RF-cryomodule#1 to the bunch compressor chicane (see Fig. 1). At an energy of 135 MeV it is compressed to minimum bunch lengths of about 0.5 mm. A second RF-module increases the energy to 230 MeV; afterwards the beam enters the undulator, followed by the spectrometer magnet and the dump. Between spectrometer dipole and dump the energy profile is monitored on a screen.

The observed energy distribution distortion [3] can roughly be described as a two-peak structure with a distance of

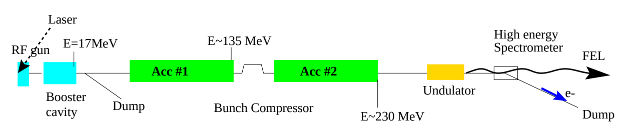

Fig. 1. Overview of the TESLA Test Facility phase I.

3 MeV which appears when the phase of RF-module #1 is close to providing full compression in the bunch compressor chicane (BC-2). Thus a considerable amount of particles must suffer an energy loss of that order. The longitudinal wakefields of the RF structures in the first module for instance are, even for the case that very short sub-structures (<50 μm) carry most of the charge, more than an order of magnitude too weak.
CSR effects, however, do have the strength to cause this kind of energy loss. Evaluating the following formula where E_0 is the

longitudinal CSR-field in Volt produced by a one-dimensional gaussian bunch with RMS-length σ and charge q_0 on an infinitely long trajectory with bending radius R_0 in the bunch center (which is nearly the maximum field),

$$E_0 = \frac{-q_0}{4\pi\epsilon_0}\left[\frac{2^{1/3}\Gamma\left(\frac{5}{6}\right)}{3^{1/3}\sqrt{\pi}R_0^{2/3}\sigma^{4/3}}\right], \qquad (1)$$

yields a field strength of about 3 MeV/m for the case that a spike of ca. 25 μm length (RMS) carries half the bunch charge. In the next chapter we will look into the possible origin of such narrow peaks and endeavour to explain the observed energy distribution break-up with CSR effects.

2. TTF-FEL Bunch Compression and Coherent Synchrotron Radiation Effects

2.1. Non-linear compression of long bunches

So the question remains how a considerable amount of charge can be gathered in such a narrow peak(s). One of us pointed out [4] that an initial bunch modulation with a Fourier component of the charge density in the Fourier space $\tilde{\Lambda}^{-}(\omega) = \alpha\cos(\omega t)$ in the presence of an energy spread dilution mechanism characterized by the longitudinal impedance $Z_{||}(\omega)$ can be enhanced when passing a beamline section with non-zero R_{56}. For the outgoing beam, the amplitude of the charge density component (after linearization) writes [4] $\tilde{\Lambda}^{+}(\omega) \simeq [\alpha R_{56}\omega Z_{||}(\omega)]/[c\gamma_0]\cos(\omega t + \varphi)$, where φ represents a phase shift and γ_0 the beam average energy. The latter expression shows that depending on ω and $Z_{||}(\omega)$ there can be significant amplification of the modulation.

Here we will start with a simpler case of a gaussian beam profile coming out of the injector, so that the peak has to be generated in the compression process itself. Indeed, a rather long bunch as in our case (2.7 mm) accumulates enough curvature in longitudinal phase space due to the non-linear cosine shape of the RF to require full compression even for final bunch lengths of around 0.5 mm (see Fig.2). The longitudinal profile after compression (see Fig.3) is then peaked (see also [5]).

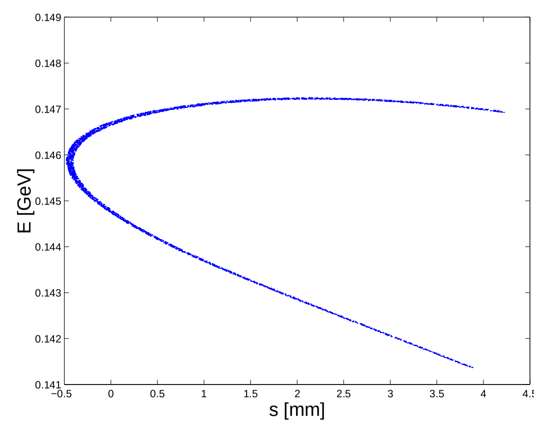

Fig. 2. A typical longitudinal phase space after compression.

The width of the leading peak is given by the initial un-correlated energy spread; in the case shown, an initial spread of 15 keV (RMS) results in a peak width of about 50 μm (RMS) which contains 50% of the charge. Since this is only the case towards the end of the third and through the fourth magnet of BC-2, we are just marginally gathering the observed energy losses.

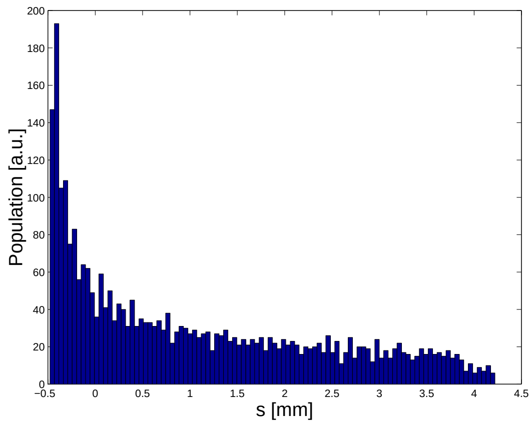

Fig. 3. Bunch charge density computed from Fig. 2.

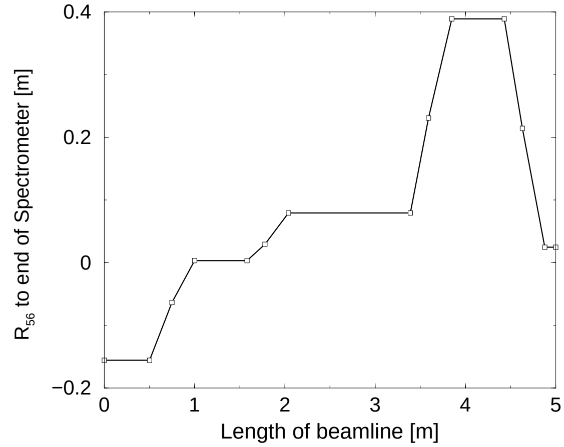

Fig. 4. 'Longitudinal compression factor' R56 from different points in the bunch compressor beam line to the end of the spectrometer magnet

2.2. *Bunch Compression in the spectrometer dipole magnet*

But now we consider the role of the spectrometer magnet, a dipole magnet of one meter length and comparable in deflection angle with the bunch compressor magnets. Any induced energy spread at a given point acts on beam parameters in the bending magnets downstream. Fig. 4 shows the longitudinal compression factor $R_{56} = -(\Delta s)/(\delta p/p)$ to the end of the spectrometer bending magnet for different positions in the bunch compressor beam line.

The energy gradient provided by the CSR in the end region of the third BC-2 magnet, for instance, will cause a further local compression of the bunch in the spectrometer magnet, since the R_{56} to the end of that magnet is of opposite sign and twice as big as that for the whole bunch compressor.

2.3. *TraFiC^4 simulation calculations*

The code TraFiC^4 was used to simulate the TTF-FEL beamline starting from the compressor entrance up to one m downtream the spectrometer dipole. The initial phase space was generated tracking phase space distribution through the injector using the multiparticle code ASTRA [6] which is in good agreement with experimental measurements. The beamline between the chicane and the spectrometer was modeled by a simple four-quadrupole telescope that provides the same transverse transfer functions as the one computed for the TTF-FEL nominal settings. Since the distortions of the longitudinal phase space are quite strong, the calculations were performed in a selfconsistent manner: the generated CSR fields are fed back to the source ensemble in a leap-frog algorithm. The incoming bunch was modeled with 320 3-d sub-bunches of 25 μm length. Shorter sub-bunches require more of them to model the long incoming bunch as a smooth charge distribution. The computing time goes with the square of the number of sub-bunches. So for the present stage of our studies we are limited to bunch structures which are 25 μm or broader.

Fig. 5 shows the results: downstream the compressor the energy profile starts to split up and downstream of the spectrometer the peaks get stronger. The distance between the peaks, however, falls short by a factor of 2-3 if compared with the measurement. The reason most likely is the limited resolution which prevents us to evaluate fields of sub-structures undergoing over-compression in the spectrometer dipole.

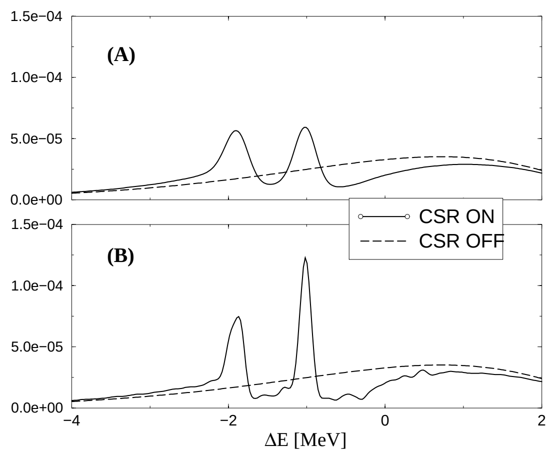

Fig. 5. TraFiC^4 simulation of beam energy distribution downstream of the compressor **(A)** and downstream of the analyzing spectrometer magnet **(B)**.

3. Conclusion and Future Plans

We have shown that CSR-induced energy redistribution inside a bunch can lead to energy splitup similar to those experimentally reported in Reference [3]. Better quantitative agreement can probably be achieved by increasing the number of

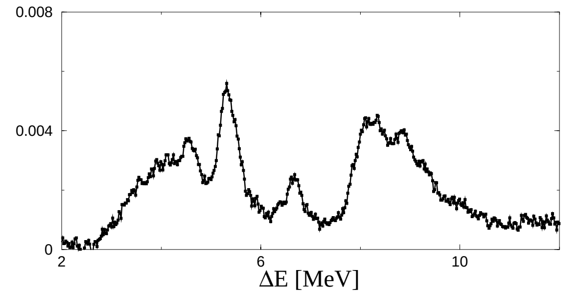

Fig. 6. An example of measured [3] energy distribution after the spectrometer (to be compared with Fig. 5 (B)).

sub-bunches and computing time. We are presently engaged in further experimental study to prove whether we are indeed observing a CSR-driven effect, particularly by varying the charge in a clean experiment. We will also specify and measure the corresponding transverse emittance dilution that should occur in the bending plane. We also plan to study the energy spread structure for different incoming dispersion into the spectrometer magnet by changing the upstream quadrupole magnets.

References

[1] Dohlus M., Kabel A., Limberg T.,Nucl. Instr. and Meth. **A 445**, pp. 338-342 (2000).

[2] Roßbach J., these proceedings

[3] Hüning H., Piot Ph., Schlarb H. these proceedings

[4] Schneidmiller E.A., to be published

[5] Li R., Proceedings of EPAC 2000, Vienna, Austria, pp. 1312-1314

[6] Flöttmann K., ASTRA user manual, `www.desy.de/mpyflo/ASTRA_dokumentation`.

Design Considerations of 10 kW-Scale Extreme Ultraviolet SASE FEL for Lithography

C. Pagani [a], E.L. Saldin [b], E.A. Schneidmiller [b], M.V. Yurkov [c]

[a] *INFN Milano - LASA, Via Cervi, 201, 20090 Segrate (MI), Italy*

[b] *Deutsches Elektronen-Synchrotron (DESY), Notkestrasse 85, Hamburg, Germany*

[c] *Joint Institute for Nuclear Research, Dubna, 141980 Moscow Region, Russia*

Abstract

The semiconductor industry growth is driven to a large extent by steady advancements in microlithography. According to the newly updated industry roadmap, the 70 nm generation is anticipated to be available in the year 2008. However, the path to get there is not obvious. The problem of construction of Extreme Ultraviolet (EUV) quantum laser for lithography is still unsolved: progress in this field is rather moderate and we can not expect a significant breakthrough in the near future. Nevertheless, there is clear path for optical lithography to take us to sub-100 nm dimensions. Theoretical and experimental work in Self-Amplified Spontaneous Emission (SASE) Free Electron Lasers (FEL) physics, and the physics of superconducting linear accelerators over the last ten years has pointed to possibility of the generation high-power optical beams with laser-like characteristics in the EUV spectral range. Recently there have been important advance in demonstrating a high-gain SASE FEL at 100 nm wavelength [1]. The SASE FEL concept eliminates the need for an optical cavity. As a result, there are no apparent limitations which would prevent operation at very short wavelength range and to increase the average output power of this device up to 10-kW level. The use of superconducting energy-recovery linac could produce a major, cost-effective facility with wall plug power to output optical power efficiency of about 1%. A 10-kW scale transversely coherent radiation source with narrow bandwidth (0.5%) and variable wavelength could be excellent tool for manufacturing computer chips with the minimum feature size below 100 nm. All components of the proposed SASE FEL equipment (injector, driver accelerator structure, energy recovery system, undulator etc.) have been demonstrated in practice. This is guaranteed success in the time schedule requirement.

1. Introduction

As the free electron laser (FEL) has several excellent features, such as high efficiency, high power and wavelength tunability, a very wide range of industrial applications is con-

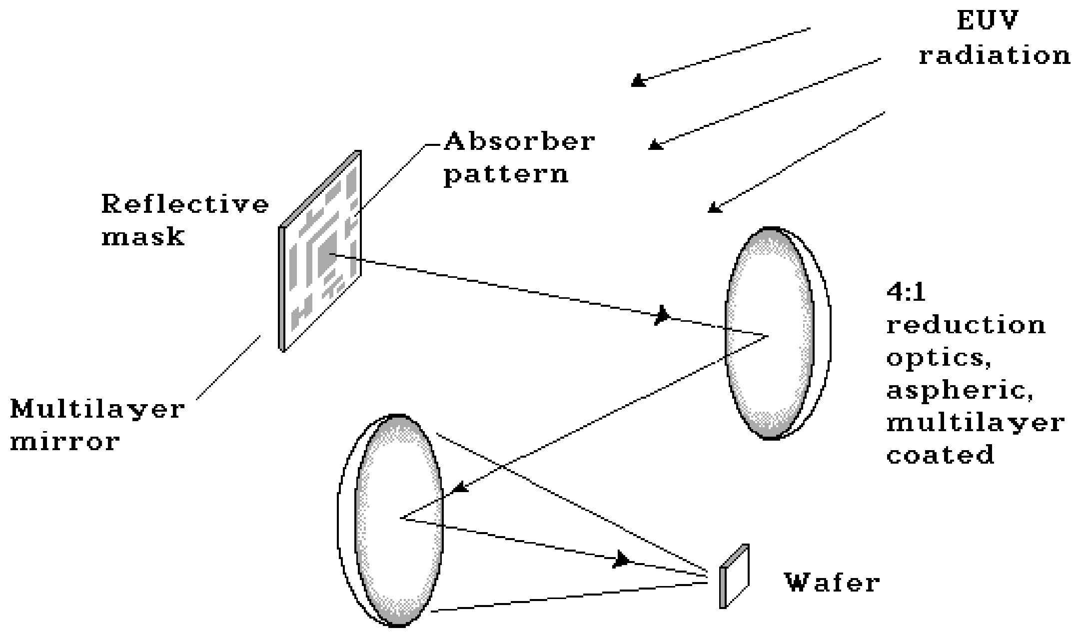

Fig. 1. The basic concept of EUV lithography

templated [2]. The most useful and pertinent frequency ranges for industrial-use FELs are in the UV and VUV. Recently an industrial UV FEL project has been launched by a consortium of industrial firms including DuPont, Xerox, and IBM [3]. In the near future, one can predict that FELs will be widely introduced to high-technology industries. In particular, in the next decade lithography will be highly supported by short-wavelength FELs. Moore's Law, postulated in 1965, predicted the exponential increase in the number of devices per chip which has driven the decrease of lithography dimensions. The exponential decrease in the minimum feature size sustained by optical lithography over the past several decades has enabled exponential increase in memory chips (from 1-kb chips for 10 μm linewidth dimension to 1-Gb for 0.18 μm) [4]. Critical dimensions for use in high volume manufacturing are anticipated to decrease from 180 nm in the year 1999 to 100 nm in the year 2006 and to 50 nm in the year 2012 [4,5]. Nevertheless, now there is no clear path for optical lithography to take us to sub-100 nm dimensions. Uncertainty regarding the extendibility of optical lithography casts doubt on the ability of the semiconductor industry to continue exponential rate of progress.

In principle, optical lithography can cover the dimension range from 100 nm to 10 nm. Potential candidate technology for high volume manufacturing beyond the use of 193 nm wavelength ArF lasers is extreme ultraviolet lithography (EUVL) (see [5]). Based on multilayer coated reflective optics, it makes a jump in wavelength to the sub-100 nm region while maintaining the evolution of optical techniques and the industry investment therein. Figure 1 shows schematically the basic elements of EUV lithography (see [5]).

Transversely coherent radiation illuminates a multilayer coated reflective mask that is overcoated with an absorber pattern. Multilayer coated reduction optics are then used to replicate the pattern at nominal 4:1 reduction on a photoresist-coated wafer. In order to correct for aberrations across the relatively large field, being limited to a few optical surfaces, one must turn to aspheric optics. The reduction optics must be highly corrected so as to print near diffraction-limited patterns at the wafer. This is a new challenge for mirrors and multilayers. It is also necessary to develop the new materials needed for photoresists and photomask.

The new short wavelength light sources must be developed for the EUV lithographic process. Significant efforts of scientists and engineers working in the field of conventional quantum lasers are directed towards the construction of powerful EUV laser for lithography. Nevertheless, this problem is still unsolved: progress in this field is rather moderate and we cannot expect a significant breakthrough in the near future. Uncertainty regarding the extendibility of convenient quantum lasers to EUV wavelength region casts doubt on the ability of the optical lithography to continue to denominate in the next decade.

In this paper we describe the approach being taken to extend the capability of light sources for lithography up to EUV region. Our approach is based on the idea to use SASE FEL for delivering extremely brilliant, coherent light with wavelength in the EUV range. Compared to the state-of-the-art EUV plasma lasers, one expects full transverse coherence, and up to 9-10 order of magnitude larger average brilliance. Since the wavelength of an SASE FEL is adjustable, selection of new materials needed for photoresists and photomask may be much easier than for the case of fixed-wavelength lasers. Recently there have been important advance in demonstrating a high-gain SASE FEL at 100 nm wavelength [1]. The experimental results presented in [1] have been achieved at the TESLA Test Facility (TTF) FEL at DESY. The goal of the TTF FEL is to demonstrate SASE FEL emission in the VUV and, in the second phase, to built a VUV- soft X-ray user facility [6].

We show that it is feasible to construct a 10-kW scale SASE FEL. The technical approach adopted in our design makes use of superconducting RF linear accelerator (SRF accelerator). With SRF linac, a SASE FEL would acquire high average power, thanks to the input beam continuous-wave (CW) nature. The energy recovery of most of the driver electron beam energy would further increase the power efficiency. The stringent electron beam qualities required for EUV SASE FEL operation can be met with a conservative injector design (using a conventional thermionic DC gun and subharmonic bunchers) and the beam compression and linear accelerator technology, recently developed in connection with high-energy linear collider and X-ray FEL programs [7,10].

Table 1
Performance characteristics of the EUV SASE FEL

Electron beam	
energy, MeV	1000
rms energy spread, %	0.18
normalized emittance, π mm-mrad	8
bunch charge, nC	2
rms bunch length, mm	0.16
repetition rate, MHz	6.1
Undulator	
type	planar
period, cm	4.5
Gap, mm	11
maximum peak field, kG	11
external beta-function, cm	100
number of undulator periods	700
Output radiation	
wavelength, nm	70
micropulse duration, ps (FWHM)	0.5
spectrum width, % (FWHM)	0.5
micropulse energy, mJ	2
peak power, GW	3
average power, kW	10

2. Facility description

Figure 2 shows the general scheme of the 10 kW-scale EUV SASE FEL driven by a 1300-MHz superconducting linear accelerator. In the acceleration sections, the superconducting cavities are designed to operate with nominal accelerating gradients of 10 MV/m. The electron beam originates in a 300-kV DC gun with gridded thermionic cathode. The injector, which is practically identical to that designed at LBL for the CW-mode operation infrared FEL [8], includes two subharmonic, room-temperature buncher cavities and 500-MHz accelerator buncher cavity. The injector produces 6.5 MeV electron pulses with a duration 33 ps (FWHM), at average current 12.2 mA (2 nC of charge, 6.1 MHz repetition rate). A 500-MHz single-cavity cryounit follows the injector which increases the beam energy to 12 MeV. The optimized beam parameters at the exit of the cryounit are: bunch charge 2 nC, bunch length 4.2 mm rms, normalized transverse emittance 8 π mm-mrad, and longitudinal rms emittance 300 π keV-mm. Accelerator buncher cavity and first accelerating cavity operating without energy recovery, will require about 170 kW RF power. The klystrons are two 75-kW TH2133 tubes, combined through a magic tee to provide the 120-kW of RF at the input coupler to the each cryounit. Results of stability analysis of the injector are presented in [8]. The charge stability $< 2\%$, bunch length stability $< 2\%$ and bunch timing stability < 3 ps well within RF control system capability.

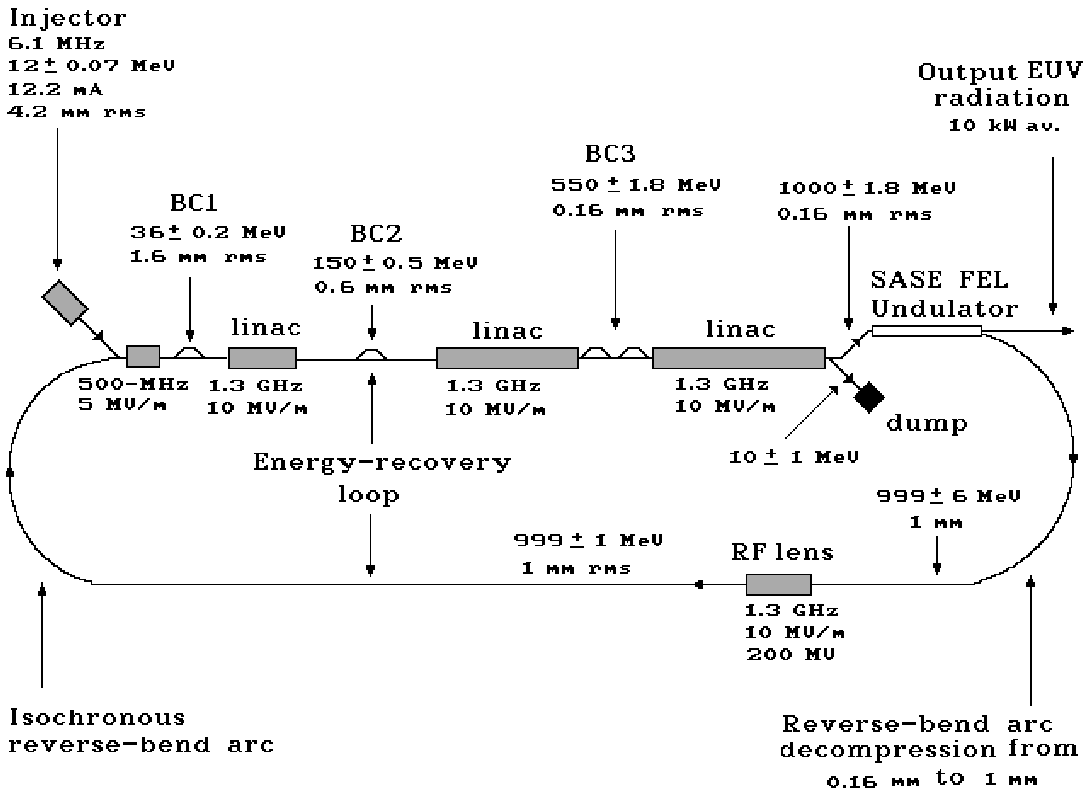

Fig. 2. Basic scheme of the high-power EUV SASE FEL

The 12 MeV energy electron beam then enters the SRF linac for further accelerating up to energy of 1000 MeV. The electron beam enters the undulator, yields EUV coherent radiation, and finally decelerates through an energy recovery pass in the SRF driver linac before its remaining energy is absorbed in the beam dump at the final energy of about 10 MeV. In the present design the beam dump energy is below the photon-neutron production threshold, so the problem of radio-nuclide production in the dump does not exist [1].

The SASE FEL provides a continuous train of 0.5 ps micropulses, with 2 mJ of optical energy per micropulse at a repetition rate 6.1 MHz. The average radiation output power can exceed 10 kW. The radiation from SASE FEL is spatially (or transversely) coherent. The temporal (or longitudinal) coherence, however, is poor due to the start-up from noise. The bandwidth of the output radiation would be about 0.5% (FWHM). A characteristic feature of multilayer mirrors is its rather small bandwidth of the reflected radiation. It is interesting to note that the radiation bandwidth of SASE FEL is close to the typical bandwidth of the multilayer mirror reflectivity.

[1] Recently Jefferson Laboratory energy-recovery SRF linac achieved 48 MeV of beam energy with 4 mA of average beam current [9].

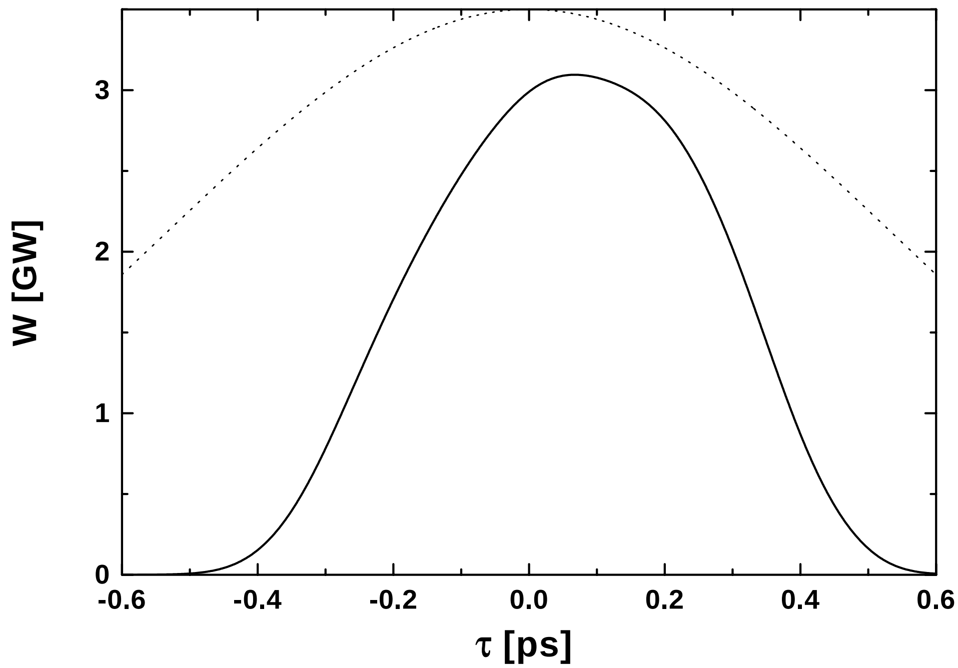

Fig. 3. Temporal structure of the radiation pulse at the undulator length of 34 m. Smooth curve is the radiation pulse profile averaged over large number of statistically independent runs. The dashed line presents the longitudinal profile of the electron beam current

A driver linac design requires considerable manipulation of the longitudinal and transverse beam dynamics in order, on the one side, to provide the bunch parameters for effective generation of the SASE radiation, and on the other side, to make effective energy recovery feasible. For the driver accelerator design we assume to use a three-stage compressor design. The compression performs in three steps: at 36 MeV (from 4.2 mm to 1.6 mm rms), 150 MeV (from 1.6 mm to 0.6 mm rms) and 550 MeV (from 0.6 mm to 0.16 mm rms). Between first and second bunch compressors the curvature of the accelerating field would impose an intolerable nonlinear correlated energy distribution along the bunch. Thus, the use of third harmonic deceleration structure is foreseen in order to reduce the non-linear energy spread. First (BC1) and second (BC2) bunch compressors are simple chicanes formed of four rectangular dipole magnets. The third (BC3) compressor is a sequence of two magnetic chicanes. The shorter bunch and higher energy allow for a much longer and more complicated design than BC2 and the complexity of double chicane is required [7]. The last part of the driver linac accelerates the bunch with an on-crest phase up to 1000 MeV.

In our conceptual design we assume the use of an energy recovery system. Only about 0.1% of the electron energy is converted to light. The reminder undergoes energy recovery, being returned to the SRF cavities, where most of it is converted back to RF power at the cavities' resonant frequency. An off-crest deceleration phase should be tuned in order to minimize the RF power consumption by the accelerator. The decelerated beam is than dumped. The SRF linac must decelerate the bunches from an energy of about 999 MeV to about 10 MeV in the beam dump. The energy spread of the electron beam after leaving the undulator is pretty large, about $\Delta E \simeq \pm 6$ MeV. An important feature of our design is that a very short electron bunch (of about 0.16 mm rms) is used for the generation of the EUV radiation. Thus, the use of energy bunching is foreseen in order to reduce the energy spread.

Energy bunching is appropriate for the situation in which particles are bunched tightly in phase, but have a large energy spread. The transformations are in the reverse order from those used for phase bunching. A relation is first established between phase and energy, creating a skew "ellipse" in longitudinal phase space. This is followed by a RF lens that reduces the energy spread by applying a reverse voltage that returns the "ellipse" to axis. Phase separation (i.e. linear correlation energy and longitudinal position) can be obtained in our case by the first, 180° bend of the recovery loop. A correlated energy spread in the bunch is cancelled by passing a RF accelerator structure at 90° crossing phase (0° corresponding to running on-crest). We select 1300-MHz structure for RF lens, based on SRF cavities operating with gradient 10 MV/m. For chosen parameters of the EUV SASE FEL we get induced energy spread 6 MeV. Voltage which is sufficient to cancel the 6 MeV energy spread is equal to 200 MV. The transformed energy spread is about 1 MeV. It should be noted that energy bunching, in our case can be treated by single particle dynamic theory. This situation is in marked contrast to phase bunching, in which the space charge and wake field effects determine the effective phase-space area occupied by the particles.

The wall plug power to output optical power efficiency of SASE FEL for industrial applications is an important criterion. For the present design we fixed on a rather conservative value of the ratio of the energy in the radiation pulse to the energy in the electron pulse of about 0.1% . Energy recovery of most of the driver electron beam energy would increase the power efficiency and we can reach the RF power to radiation beam power efficiency of about 7%. Assuming the efficiency of the klystron modulator 80% , and electronic efficiency of the klystron 60% , we obtain that the AC wall plug power to output radiation power efficiency is about 3%. The present design requires cooling of about 25 cryomodules. To do this, we need a He refrigerator with net power consumption about one MW. As a result we obtain total efficiency of proposed SASE FEL about to 1%.

A complete description of the SASE FEL can be performed only with three-dimensional (3-D) time-dependent numerical simulation code. With the design and construction of VUV and X-ray SASE FELs, many 3-D time-dependent codes have been developed over the years in order to describe FEL amplifier start-up from shot noise. Optimization of the parameters of the EUV SASE FEL in our case has been performed with the code FAST [11].

The optimized parameters of the EUV SASE FEL are presented in Table 1. Averaging

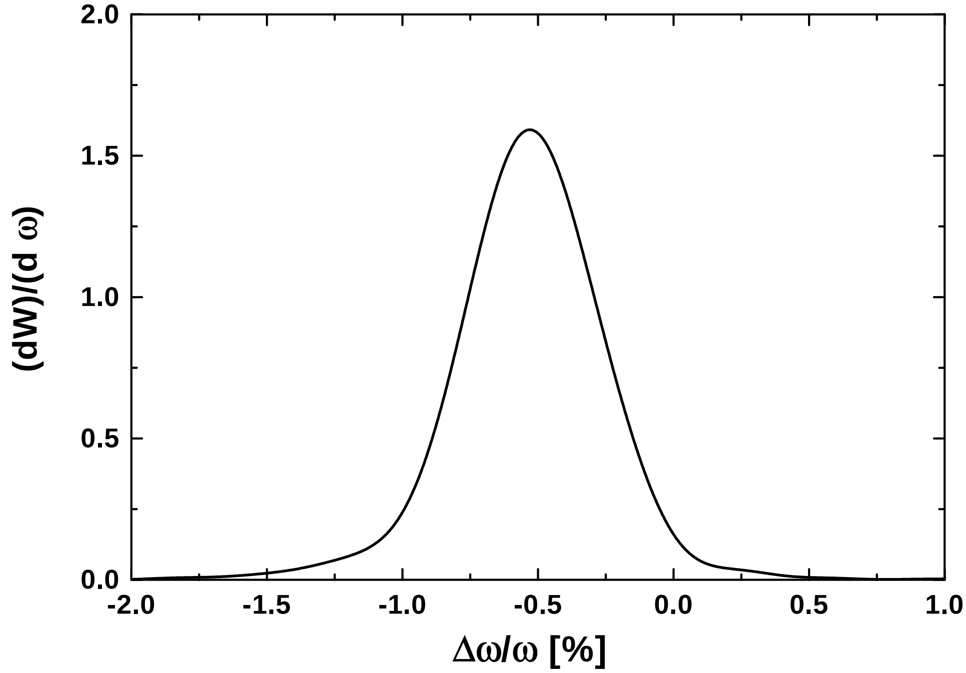

Fig. 4. Spectral distribution of the energy in radiation pulse

over one hundred simulation runs with statistically independent shot noise in the electron beam gives the radiation pulse shape, which is plotted in Fig. 3. We obtain that the duration of the radiation pulse is about 0.5 ps and pulse energy is about 2 mJ. At the next step of calculations we find the spectral distribution of the radiation power for each angle in far zone, and after integrating over all angles we obtain integral spectrum of the radiation pulse. Figure 4 present the spectrum of EUV SASE FEL. An important characteristic of the radiation source is the degree of transverse coherence. Corresponding definitions for the degree of coherence in the high-gain linear regime of the SASE FEL can be found in [12]. Our simulations show that the degree of coherence in our case is close to unity ($\zeta \simeq 0.9$).

Analysis of parameters of a high power EUV SASE FEL shows that its radiation wavelength range is clearly limited by the quality of the electron beam achievable with injector. For 10 kW-scale EUV SASE FEL operating in 10-20 nm wavelength range a new approach for the injector has to be considered. In this context the R&D work on SRF photoinjector [13] looks very promising.

References

[1] J. Andruszkov, et al., "First Observation of Self-Amplified Spontaneous Emission in a Free Electron Laser at 109 nm Wavelength", submitted to Phys. Rev. Lett. (2000)

[2] C. Yamanaka, Nucl. Instrum. and Methods A 318(1992)1

[3] G. R. Neil et al., Nucl. Instrum. and Methods A 358(1995)159

[4] C. P. Ausschnitt, Microelectronic Engineering 41/42(1998)41

[5] D. Attwood, "Soft X-rays and Extreme Ultraviolet Radiation" (Cambridge University Press 1999)

[6] J. Rossbach, Nucl. Instrum. and Methods A 375(1996)269

[7] The Linac Coherent Light Source (LCLS) Design Study Report, SLAC-R-521, 1998

[8] K.-J. Kim et al., LBL preprint Pub-5335(1992)

[9] G. R. Neil et al., Nucl. Instrum. and Methods A 445(2000)192

[10] R. Brinkman et al., (Eds), "Conceptual Design of 500 GeV $e^{+}e^{-}$ Linear Collider with Integrated X-ray Facility", DESY 1997-048, ECFA 1997-182, Hamburg, May 1997

[11] E. L. Saldin, E. A. Schneidmiller, and M.V. Yurkov, Nucl. Instrum. and Methods A 429(1999)233

[12] E. L. Saldin, E. A. Schneidmiller, and M.V. Yurkov, "The Physics of Free Electron Lasers" (Springer-Verlag, Berlin-Heidelberg-New York, 1999)

[13] F. Gabriel et al., Nucl. Instrum. and Methods A 429(1999) II 91

Design considerations of a MW-scale, high-efficiency, industrial-use, ultraviolet FEL amplifier

C. Pagani [a], E.L. Saldin [b], E.A. Schneidmiller [b], M.V. Yurkov [c]

[a] *INFN Milano - LASA, Via Cervi, 201, 20090 Segrate (MI), Italy*

[b] *Deutsches Elektronen-Synchrotron (DESY), Notkestrasse 85, D-22607 Hamburg, Germany*

[c] *Joint Institute for Nuclear Research, Dubna, 141980 Moscow Region, Russia*

Abstract

Theoretical and experimental work in free electron laser (FEL) physics, and the physics of particle accelerators over the last ten years has pointed to the possibility of the generation of MW-level optical beams with laser-like characteristics in the ultraviolet (UV) spectral range. The concept is based on generation of the radiation in the master oscillator – power FEL amplifier (MOPA) configuration. The FEL amplifier concept eliminates the need for an optical cavity. As a result, there are no thermal loading limitations to increase the average output power of this device up to the MW-level. The problem of a tunable master oscillator can be solved with available conventional quantum lasers. The use of a superconducting energy-recovery linac could produce a major, cost-effective facility with wall plug power to output optical power efficiency of about 20 per cent that spans wavelengths from the visible to the deep ultraviolet regime.

1. Introduction

Significant efforts of scientists and engineers working in the field of conventional quantum lasers are directed towards the construction of powerful ultraviolet (UV) lasers for industrial applications such as material processing, lithography, isotope separation, and photo-induced chemistry. Nevertheless, this problem is still unsolved: progress in this field is rather moderate and we cannot expect a significant breakthrough in the near future.

Recent investigations have shown that this problem can be solved by free electron lasers (FELs), which can be divided into two classes: amplifiers and oscillators. FEL amplifiers amplify the input electromagnetic wave from the external master oscillator. The FEL oscillator can be considered as an FEL amplifier with feedback, which is carried out by means of an optical resonator. Recently a kW-scale UV FEL oscillator project has been initiated at Jefferson Laboratory [1,2].

The main problem of constructing a high average power UV FEL oscillator is the heating effects in the cavity mirrors. The results of optical resonator modeling have demonstrated that the oscillator scheme for UV FEL is quite adequate for the kiloWatt demonstrator, but not scalable even to the 100 kW device [3]. If we consider the high gain FEL amplifier, we find that there are no thermal loading limitations to increasing the average output power of this device up to the megawatt level. Since the amplification process develops in vacuum during one pass of the electron beam through the undulator, the problem of absorption of radiation in the cavity mirrors does not exist at all.

2. Facility description

In this paper we perform design consideration of a MW-scale UV FEL amplifier. Figure 1 shows the general scheme of the FEL amplifier. The arrangement of injector, which is practically identical to that designed at LBL for the CW-mode operation infrared FEL oscillator[6], is shown schematically in Fig. 2. The electron beam originates in a high-voltage DC gun with gridded thermionic cathode. The injector includes two subharmonic, room-temperature buncher cavities and a 500 MHz accelerating module. The bunched low-energy electron beam then enters the SRF linac for further acceleration up to energy of

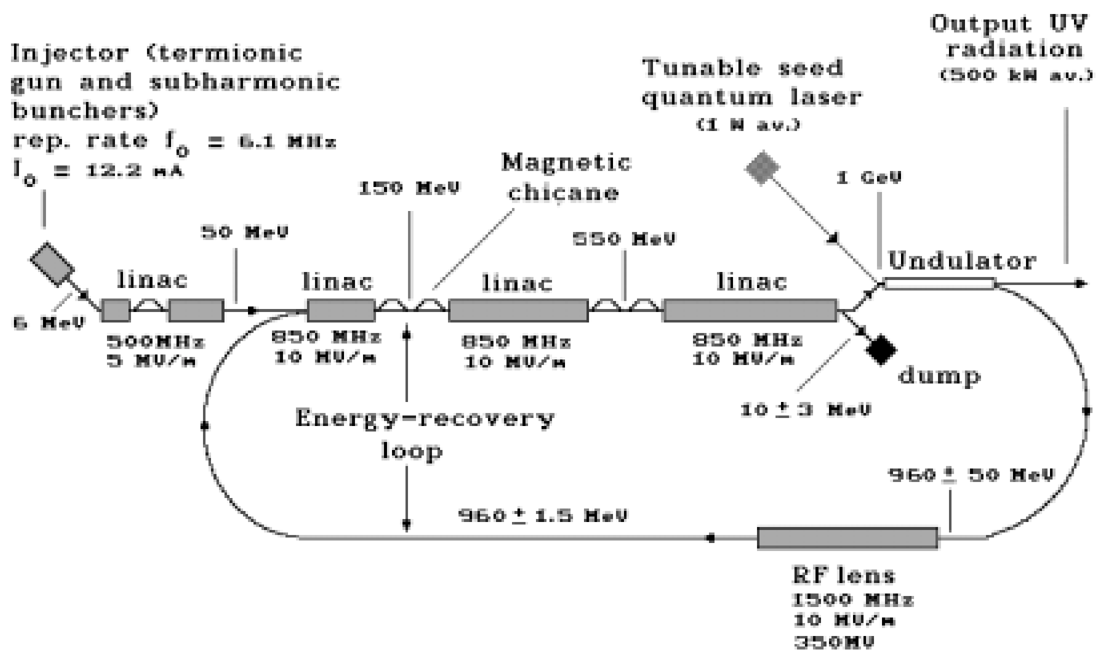

Fig. 1. Schematic illustration of design configuration for the UV FEL amplifier

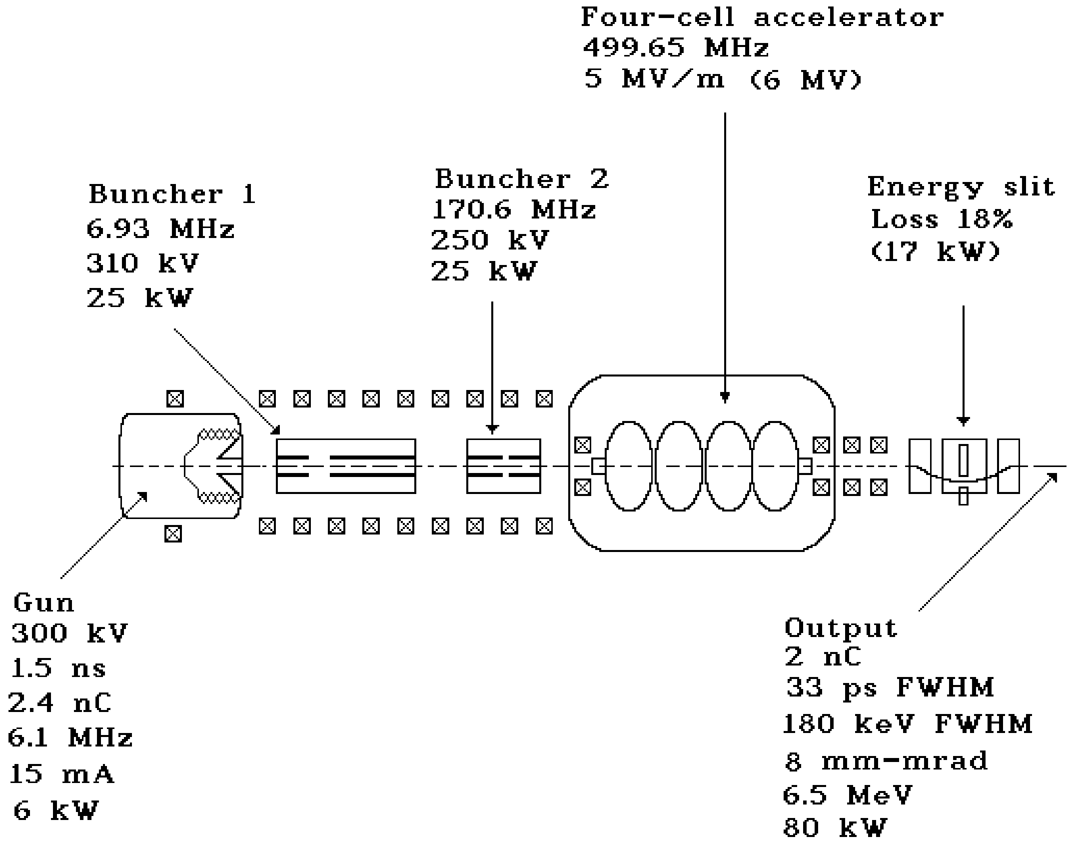

Fig. 2. Schematic of the UV FEL amplifier injector

1000 MeV. The accelerated beam enters the undulator, yields light, and finally decelerates through an energy recovery pass in the SRF linac before its remaining energy is absorbed in the beam dump at the final energy of about 10 MeV. In our conceptual design we assume the use of a conventional quantum laser as a master oscillator, which provides a continuous train of 10 ps micropulses, with 100 nJ of optical energy per micropulse. The average output power of the master laser is about one Watt. A dye laser system with subsequent nonlinear optical elements pumped by Nd glass laser can be used for this purpose.

In order to achieve the high peak current in the undulator the bunch must be compressed in a series of magnetic chicanes. The compression performs in three steps: at 30 MeV (from 4.2 mm to 1.6 mm rms), 150 MeV (from 1.6 mm to 0.45 mm rms) and 550 MeV (from 0.45 mm to 0.15 mm rms) [1]. Requirements for magnetic bunch compressors in our case are very close to those for magnetic bunch compressors in X-ray FELs [4]. In particular,

[1] The magnetic bunch compressors are arranged and located such that RF curvature, space charge effects, longitudinal wake fields do not limit the achievable bunch parameters

Table 1
Performance characteristics of the UV FEL amplifier

Electron beam	
Energy	1000 MeV
rms energy spread	0.2 %
Bunch charge	2 nC
rms pulse duration	0.5 ps
Micropulse repetition rate	6.1 MHz
normalized emittance	8π mm-mrad
Undulator	
Type	Planar
Period	7.0 cm
Gap	12 mm
Maximum peak field	1.15 T
# of undulator periods	850
External beta-function	3.0 m
Radiation	
Wavelength,	260 – 500 nm
Spectrum width	Transform-limited
Peak power	110 GW
Average power	0.5 MW
Micropulse duration	0.7 ps (FWHM)
Micropulse energy	83 mJ
Repetition rate	6.1 MHz

the magnetic chicanes for the VUV FEL at TTF, which is presently under construction, is a good example for many problems related to our bunch compressor design [10].

Optimization of the parameters of the FEL amplifier has been performed with the three-dimensional time-dependent simulation code FAST [8]. This code has been developed in the framework of the investigations on X-ray FELs. The optimized parameters of UV FEL amplifier are presented in Table 1. A reliable method to increase the FEL efficiency consists in an adiabatic change of the undulator parameter (or in undulator tapering). The length of untapered section of the undulator is equal to 18.4 m. At the radiation wavelength 260 nm, the peak value of magnetic field is about 1.15 T. The field in the tapered section is reduced linearly with the length from 1.15 T down to the value of 1.05 T at the end of the undulator of 60 m. Figure 3 presents evolution along the undulator length of the energy of the radiation pulse. Details regarding high-power UV FEL amplifier design can be found in [11].

The undulator for an industrial-use UV FEL amplifier needs to be rather long in order to provide the required power of the output radiation. Thus, strong focusing elements are needed for the electron beam transport system. A combined function undulator (CFU) approach [12], to implement strong focusing in a long undulator, is used in our design. Tolerances for field errors and alignment are estimated on the basis of work done for the 30 m long CFU undulator for the VUV FEL at the TESLA Test Facility [13].

The wall plug power to output optical power efficiency of a FEL for industrial appli-

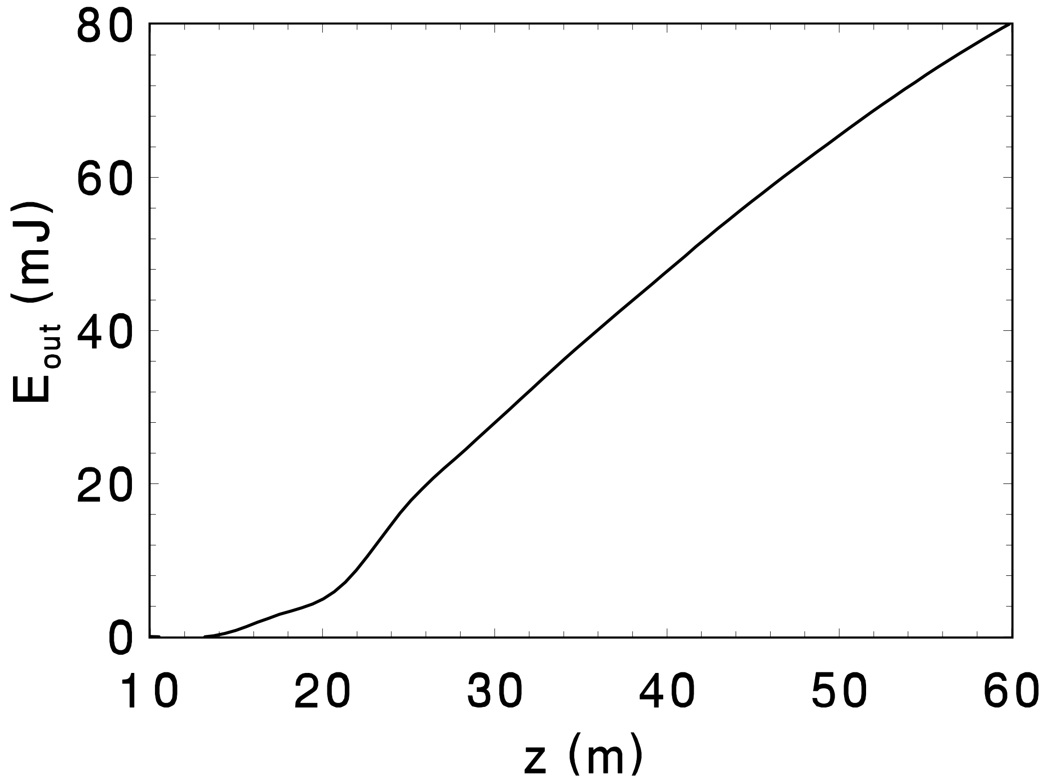

Fig. 3. Energy in the radiation pulse versus the length for the FEL amplifier

cations is an important criterion. For the present design the ratio of the energy in the radiation pulse to the energy in the electron pulse is about 4%. Energy recovery of most of the driver electron beam energy would increase the power efficiency. The energy of the spent electron beam is about 950 MeV. The energy spread of the electron beam after leaving the undulator is pretty large, about ± 50 MeV. An important feature of our design is that a very short electron bunch (of about 0.15 mm rms) is used for the generation of the radiation. When the electron bunch leaves the undulator, we apply a transformation of the particle distribution in the longitudinal phase space resulting in increased bunch length and decreased energy spread [7] [2]. After leaving the undulator the electron beam passes a debuncher (first arc). The length of the bunch is increased by a factor of about 30, and the uncorrelated energy spread is transformed to one correlated with the position of the particles in the bunch. The resulting electron bunch length is still tolerable for use in the energy recovery scheme. Subsequently, the electron bunch passes a special 1500-MHz SRF accelerating structure at 90°crossing phase (0° corresponding to running on-crest) and the energy spread of the electron beam is reduced to about 1.5 MeV. The electron

[2] The transformations are in the reverse order from those used for phase bunching

bunch with such energy spread can be decelerated safely down to the energy of about 10 MeV, which is much less than the initial energy spread [3]. As a result, we can reach the RF power to output optical power efficiency of about 80%. Assuming the efficiency of the klystron modulator be 80%, and the electronic efficiency of the high power CW klystron 60%, we obtain that the AC wall plug power to output optical power efficiency is about 40%. Another source of the energy consumption is cryogenic system of the SRF accelerator. The present design requires cooling of about 30 cryomodules. To do this, we need a He refrigerator with net power consumption about one MW. As a result, we obtain a total efficiency of the proposed UV FEL amplifier about to 20%.

Driver linac cavities will use the energy recovery to reduce the RF power requirements to less than 5 kW per cavity. For our design we had decided to power cryomodule by one 23-kW klystron YK1180 from Siemens. Injector cavities and initial part of linac (first 50 MeV accelerator section) operating without energy recovery, will require about 600 kW RF power. For this active part of the SRF linac we selected 500-MHz SRF structure, since high power klystrons are commercially available for this frequency. An appropriate RF source is one 1000-kW TH2105 tube.

Acknowledgments

We thank J.R. Schneider, D. Trines and A. Wagner for their interest in this work, and B. Dwersteg, J. Pflüger, and J. Sekutowicz for many useful discussions and recommendations on technical topics.

References

[1] G.R. Neil et al., Nucl. Instrum. and Methods A 358(1995)159

[2] S.V. Benson et al., Nucl. Instrum. and Methods A 429(1999)27

[3] S.V. Benson et al., Nucl. Instrum. and Methods A 375(1996) ABS 4

[4] Conceptual Design of 500 GeV e^+e^- Linear Collider with Integrated X-ray Facility, DESY 1997-048

[5] The Linac Coherent Light Source (LCLS) Design Study Report, SLAC-R-521, 1998

[6] K.-J. Kim et al., LBL preprint Pub-5335(1992)

[7] A.J. Lichtenberg "Phase-Space Dynamics of Particles" John Willey and Sons, INC. New York-London-Sydney-Toronto 1969

[8] E.L. Saldin, E.A. Schneidmiller, and M.V. Yurkov, Nucl. Instrum. and Methods A 429(1999)233

[3] In the present design the beam dump energy is below the photon-neutron production threshold, so the problem of radio-nuclide production in the dump does not exist

[9] "A VUV Free Electron Laser at the TESLA Test Facility: Conceptual Design Report", DESY Print TESLA-FEL 95-03, Hamburg, DESY, 1995

[10] T. Limberg et al., Nucl. Instrum. and Methods A 375(1996)322

[11] C. Pagani et al., "Design considerations of MW-Scale, High-Effisiency, Industrial-Use, Ultraviolet FEL Amplifier" DESY 00-015 (2000)

[12] J. Pflueger, Y.M. Nikitina Nucl. Instrum. and Methods A 381(1996)554

[13] J. Pflueger, H. Lu and T. Teichmann, Nucl. Instrum. and Methods A 429(1999)386

Observation of Self-Amplified Spontaneous Emission in the Wavelength Range from 80 nm to 180 nm at the TESLA Test Facility FEL at DESY

J. Rossbach, for the TESLA FEL Group[1]

Deutsches Elektronen-Synchrotron DESY, Notkestr. 85, 22603 Hamburg

joerg.rossbach@desy.de

ABSTRACT

The first observation of Self-Amplified Spontaneous Emission (SASE) in a free-electron laser (FEL) in the Vacuum Ultraviolet range between 80 nm and 180 nm wavelength is presented. The observed free-electron laser gain (typically above 1000) and the radiation characteristics, such as dependency on bunch charge, angular distribution, spectral width and intensity fluctuations are discussed. Some accelerator issues are covered, and the future plans for the TESLA Test Facility (TTF) FEL are mentioned.

PACS classification: 41.60.Cr, 29.17.+w, 29.27.-a,Fh

keywords: Free-Electron Laser, Self-Amplified Spontaneous Emission, VUV radiation, bunch compression

---

[1] V. Ayvazyan, N. Baboi, R. Brinkmann, M. Castellano, P. Castro, W. Decking, M. Dohlus, H.T. Edwards, B. Faatz, A. Fateev, J. Feldhaus, K. Flöttmann, A. Gamp, T. Garvey, C. Gerth, E. Gluskin, V. Gretchko, U. Hahn, K. Honkavaara, M. Hüning, R. Ischebeck, M. Jablonka, T. Kamps, M. Körfer, J. Krzywinski, J. Lewellen, M. Liepe, A. Liero, T. Limberg, T. Lokajczyk, C. Magne, G. Materlik, J. Menzel, P. Michelato, A. Mosnier, A. Novokhatski, C. Pagani, F. Peters, J. Pflüger, P. Piot, L. Plucinski, K. Rehlich, I. Reyzl, J. Rossbach, S. Roth, E.L. Saldin, W. Sandner, H. Schlarb, G. Schmidt, P. Schmüser, J.R. Schneider, E.A. Schneidmiller, H.J. Schreiber, S. Schreiber, D. Sertore, S. Simrock, B. Sonntag, F. Stephan, K. Sytchev, M. Timm, M Tonutti, E. Trakhtenberg, R. Treusch, D. Trines, V. Verzilov, R. Wanzenberg, T. Weiland, H. Weise, M. M. White, I. Will, K. Wittenburg, M.V. Yurkov, K. Zapfe

1 INTRODUCTION

X-ray lasers are expected to open up new and exciting areas of basic and applied research in biology, chemistry and physics. Due to recent progress in accelerator technology the attainment of the long sought-after goal of wide-range tunable laser radiation in the Vacuum-Ultraviolet and X-ray spectral regions is coming close to realization with the construction of Free-Electron Lasers (FEL) [1] based on the principle of Self-Amplified Spontaneous Emission (SASE) [6,7]. In a SASE FEL lasing occurs in a single pass of a relativistic, high-quality electron bunch through a long undulator magnet structure.

The photon wavelength λ_{ph} of the first harmonic of FEL radiation is related to the period length λ_u of a planar undulator by

$$\lambda_{ph} = \frac{\lambda_u}{2\gamma^2}\left(1+\frac{K^2}{2}\right) \quad , \qquad (1)$$

where $\gamma = E/m_e c^2$ is the relativistic factor of the electrons, $K = eB_u\lambda_u/2\pi m_e c$ the 'undulator parameter' and B_u the peak magnetic field in the undulator.

At very short wavelengths, the generation of an electron beam of extremely high quality in terms of emittance, peak current and energy spread, and a high-precision undulator of sufficient length are the challenge to be met in order to achieve high gain or even laser saturation within a single pass. Provided the spontaneous radiation from the first part of the undulator overlaps the electron beam, the electromagnetic radiation interacts with the electron bunch leading to a density modulation (micro-bunching) which enhances the power and coherence of radiation. In this "high gain mode" [2,3,4], the radiation power $P(z)$ grows exponentially with the distance z along the undulator

$$P(z) = P_0 \cdot A \cdot \exp(2z/L_g) \quad , \qquad (2)$$

where L_g is the field gain length, P_0 the effective input power (see below), and A the input coupling factor [3,4]. A is equal to 1/9 in one-dimensional FEL theory with an ideal electron beam.

The R&D program for the TESLA FEL aims at wavelength far below the visible. Therefore, there is no laser tunable over a wide range to provide the input power P_0. Instead, the spontaneous undulator radiation from the first part of the undulator is used as an input signal to the downstream part. FELs based on this Self-Amplified-Spontaneous-Emission (SASE) principle [5,6] are presently considered the most attractive candidates for delivering extremely brilliant, coherent light with wavelength in the Ångström regime [7-10]. Compared to state-of-the-art synchrotron radiation sources, one expects full transverse coherence, larger average brilliance and, in particular, up to eight or more orders of magnitude larger peak brilliance at pulse lengths of about 200 fs FWHM.

2 EXPERIMENTAL SET-UP

The experimental results presented in this paper have been achieved at the TESLA Test Facility (TTF) Free-Electron Laser [11] at the Deutsches Elektronen-Synchrotron DESY. The TESLA (TeV-Energy Superconducting Linear Accelerator) collaboration consists of 39 institutes from 9 countries and aims at the construction of a 500 GeV (center-of-mass) e+/e- linear collider with an integrated X-ray laser facility [9]. Major hardware contributions to TTF have come from Germany, France, Italy, and the USA. The goal of the TTF FEL is to demonstrate SASE FEL emission in the VUV and, in a second phase, to build a soft X-ray user facility [12,13]. The layout is shown in Fig. 1. The main parameters for FEL operation are compiled in Table 1.

The injector is based on a laser-driven 1½-cell rf gun electron source operating at 1.3 GHz [15]. It uses a Cs_2Te cathode [16] and can generate bunch charges more than 10 nC at 1 MHz repetition rate. A loading system allows mounting and changing of cathodes while maintaining ultra-high vacuum conditions [16]. The cathode is illuminated by a train of UV laser pulses generated in a mode-locked solid-state laser system [17] synchronized with the rf. An energy of up to 50 µJ with a pulse-to-pulse variation of 2 % (rms) is achieved [18]. The UV pulse length measured with a streak camera is σ_t = 7.1 ± 0.6 ps . The rf gun is operated with a peak electric field of 37 MV/m on the photocathode. The rf pulse length was limited to 100 µs and the repetition rate to 1 Hz for machine protection reasons. The gun section is followed by a 9-cell superconducting cavity, boosting the energy to 16 MeV. The superconducting accelerator structure has been described elsewhere [14].

The undulator is a fixed 12 mm gap permanent magnet device using a combined function magnet design [19] with a period length of λ_u = 27.3 mm and a peak field of B_u = 0.46 T, resulting in an undulator parameter of K=1.17. The beam pipe diameter in the undulator (9.5 mm) [20] is much larger than the beam diameter (300µm). Integrated quadrupole structures produce a gradient of 12 T/m superimposed on the periodic undulator field in order to focus the electron beam along the undulator. The undulator system is subdivided into three segments, each 4.5 m long and containing 10 quadrupole sections to build up 5 full focusing-defocusing (FODO) cells. The FODO lattice periodicity runs smoothly from segment to segment. There is a spacing of 0.3 m between adjacent segments for diagnostics [21].

The total length of the system is 14.1 m. The vacuum chamber incorporates 10 beam position monitors and 10 orbit correction magnets per segment, one for each quadrupole [20].

For optimum overlap between the electron and light beams, high precision on the magnetic fields and mechanical alignment are required. The undulator field was adjusted such that the expected rms deviations of the electron orbit should be smaller than 10 μm at 300 MeV [22]. The beam orbit straightness in the undulator is determined by the alignment precision of the superimposed permanent-magnet quadrupole fields which is better than 50 µm in both vertical and horizontal direction. The relative alignment of the three segments is accomplished with a laser interferometer to better than 30 µm [23].

Different techniques have been used to measure the emittance of the electron beam [21,24]: Magnet optics scanning ("quadrupole scans"), tomographic reconstruction of the phase space including space charge effects, and the slit system method. All methods use optical transition radiation emitted from aluminum foils to measure the bunch profiles and yield values for the normalized emittance of $(4 \pm 1)\ \pi$ mrad mm for a bunch charge of 1 nC at the exit of the injector. The emittance in the undulator, as determined from quadrupole scans and from a system of wire scanners was typically between 6 and 10 π mrad mm (in both horizontal and vertical phase space). It should be noted that the measurement techniques applied determine the emittance integrated over the entire bunch length. However, for FEL physics, the emittance of bunch slices much shorter than the bunch length is the relevant parameter. It is likely that, due to spurious dispersion and wakefields, the bunch axis is tilted about a transverse axis such that the projected emittance is larger than the emittance of any slice. Based on these considerations we estimate the normalized slice emittance in the undulator at $(6 \pm 3)\ \pi$ mrad mm.

A bunch compressor is inserted between the two accelerating modules, in order to increase the peak current of the bunch up to 500 A, corresponding to 0.25 mm bunch length (rms) for a 1 nC bunch with Gaussian density profile. Experimentally, it is routinely verified that a large fraction of the bunch charge is compressed to a length below 0.4 mm (rms) [25]. There are indications that the core is compressed even further. We estimate the peak current for the FEL experiment at (400 ± 200) A. Coherent synchrotron radiation in the magnetic bunch compressor may affect the emittance and the energy spread at such short bunch lengths [26,27]. Beam parameters like peak current and slice emittance determine the FEL gain length critically. Thus we consider further improvements of beam diagnostics essential for any precise verification of FEL models at short wavelengths.

For radiation intensity measurements [28] we use a PtSi photdioade integrating over all wavelengths. The detector unit was placed 12 m downstream the undulator exit. A 0.5 mm iris was placed in front of the photodiode in order to avoid saturation effects.

3 FEL MEASUREMENTS

A strong evidence for the FEL process is a large increase in the on-axis radiation intensity if the electron beam is injected such that it overlaps with the radiation during the entire passage through the undulator. Fig. 2 shows the intensity passing a 0.5 mm iris, located on axis 12 m downstream of the undulator, as a function of the horizontal beam position at the undulator entrance. The observed intensity inside a window of ±200 µm around the optimum beam position is a factor of more than 100 higher than the intensity of spontaneous radiation. This intensity gain was first observed with the photodiode and later confirmed with the CCD camera of the spectrometer. The central wavelength for this first SASE demonstration at the TTF FEL was 108.5 nm [29].

SASE gain is expected to depend on the bunch charge in an extremely nonlinear way. An intensity enhancement by a factor of more than 100 was observed when increasing the bunch charge from 0.3 nC to 0.6 nC while keeping the beam orbit constant for optimum gain. The gain did not further increase when the bunch charge exceeded some 0.6 nC. This needs further study, but the most likely reason is that the beam emittance becomes larger for increasing Q thus reducing the FEL gain.

The wavelength of 108.5 nm was consistent with the measured beam energy of (233±5) MeV and the known undulator parameter K=1.17, see Eq. (1). From the user point of view a most important feature of FELs starting from noise is the arbitrary tunability of wavelength. At TTF FEL this was demonstrated by tuning the electron beam energy between 272 MeV and 181 MeV, corresponding to wavelengths from 80 nm to 181 nm. Within this range, SASE was achieved at any energy where the SASE search procedure was performed, see Fig. 3. Typically, a SASE gain (for definition, see below) above 1000 was observed. The spectral width was in most cases in agreement with theory. A possible source of spectral widening was energy jitter, since the spectra were taken by averaging over many bunches.

A characteristic feature of SASE FELs is the concentration of radiation power into a cone much narrower than that of wavelength integrated undulator radiation, whose opening angle is in the order of $1/\gamma$. Measurements done by moving the 0.5 mm iris horizontally together with the photo diode confirm this expectation, see Fig. 4. The spontaneous intensity is amplified by a factor of 30 to be visible on this scale.

In order to study which section of the undulator contributes most to the FEL gain, we applied closed orbit beam bumps to different sections of the undulator, thus disturbing the gain process at various locations along the undulator.

It was seen that practically the entire undulator contributes, but with some variation in local gain. Some improvement in the over-all gain should be possible by optimizing the settings of the 30 orbit correction coils.

The energy flux was 2 nJ/mm² at the location of the detector and the on-axis flux per unit solid angle was about 0.3 J/sr. This value was used as a reference point for the numerical simulation of the SASE FEL at 108.5 nm with the code FAST [30]. The longitudinal profile of the bunch current was assumed to be Gaussian with an rms length of 0.25 mm. The transverse distribution of the beam currrent density was also taken to be Gaussian. Calculations have been performed for a Gaussian energy spread of 0.1%, and the normalized emittance was varied in the simulations between 2 and 10 π mrad mm. Our calculations show that in this range of parameters the value of the effective power of shot noise P_{in} and coupling factor A~0.1 (see eq. 2) are nearly constant. A level of energy flux of 0.3 J/sr is obtained at five field gain lengths Lg. With these parameters the FEL gain can be estimated at $G \approx 3 \cdot 10^3$ with a factor of 3 uncertainty which is mainly due to the imprecise knowledge of the longitudinal beam profile. If we assume that the entire undulator contributes to the FEL amplification process, we estimate the normalized emittance at 8 π mrad mm in reasonable agreement with the measurements. However, as stated before, it is more likely that the normalized (slice) emittance is smaller and the electron orbit is not perfectly straight. This is supported by the observation that in a first systematic attempt of improving the orbit straightness in the undulator, the SASE gain at 109 nm was increased by another factor of 3. Thus, at 109 nm the maximum achieved gain was $G \approx 1 \cdot 10^4$. It should be noted that large SASE gain was achieved in a stable and reproducible way for several weeks.

It is essential to realize that the fluctuations seen in Fig. 2 are not primarily due to unstable operation of the accelerator but are inherent to the SASE process. Shot noise in the electron beam causes fluctuations of the beam density, which are random in time and space [31]. As a result, the radiation produced by such a beam has random amplitudes and phases in time and space and can be described in terms of statistical optics. In the linear regime of a SASE FEL, the radiation pulse energy measured in a narrow central cone (opening angle ±20 µrad in our case) at maximum gain is expected to fluctuate according to a gamma distribution *p(E)* [32],

$$p(E) = \frac{M^M}{\Gamma(M)} \left(\frac{E}{\langle E \rangle} \right)^{M-1} \frac{1}{\langle E \rangle} \exp\left(-M \frac{E}{\langle E \rangle} \right) \quad , \tag{3}$$

where $\langle E \rangle$ is the mean energy, $\Gamma(M)$ is the gamma function with argument M, and $M^{-1} = \langle (E-\langle E \rangle)^2 \rangle / \langle E \rangle^2$ is the normalized variance of E. M corresponds to the number of longitudinal optical modes. Note that the same kind of statistics applies for completely chaotic polarized light, in particular for spontaneous undulator radiation.

For these statistical measurements the signals from 3000 radiation pulses have been recorded at 109 nm wavelength, with the small iris (0.5 mm diameter) in front of the photo diode to guarantee that transversely coherent radiation pulses are selected. As one can see from Fig. 5, the distribution of the energy in the radiation pulses is quite close to the gamma distribution. The relative rms fluctuations are about 26% corresponding to M = 14.4. Similar measurements have been performed at other wavelengths. One should take into account that these fluctuations arise not only from the shot noise in the electron beam, but the pulse-to-pulse variations of the beam parameters can also contribute to the fluctuations. Thus, the value $M \approx 14$ can be considered a lower limit for the number of longitudinal modes in the radiation pulse. Using the width of radiation spectrum we calculate the coherence time [32] and find that the part of the electron bunch contributing to the SASE process is at least 100 µm long. From the quality of the fit with the gamma distribution we can also conclude that the statistical properties of the radiation are described with Gaussian statistics. In particular, this means that there are no FEL saturation effects.

4 SUMMARY

High gain SASE in the VUV has become reality. Wavelength tuning between 80 nm and 181 nm as well as reliable operation was demonstrated at DESY over several weeks. To date, all observations are in agreement with the present SASE FEL models. More precise electron beam diagnostics is desirable for a more detailed verification of FEL models. Now there is more than ever optimism justified in view of the feasibility of future X-ray user facilities. However, there is still a way to go: The SASE gain demonstrated so far is still some orders of magnitude below saturation. Also, stable operation with long pulse trains containing several thousand pulses and flexible timing pattern, as requested by users, remains a challenge for accelerator physicists.

5 ACKNOWLEDGEMENTS

The authors acknowledge that successful FEL operation has been achieved as a joint effort of all members of the TESLA collaboration. A list of participating institutes can be found in Ref. [29].

References

[1] J.M. Madey, *J. Appl. Phys.* **42** 1906 (1971)

[2] K.J. Kim, *Phys. Rev. Lett.* **57** 1871 (1986)

[3] S. Krinsky, L.H. Yu, *Phys. Rev.* **A35** 3406 (1987)

[4] E.L. Saldin, E.A. Schneidmiller, M.V. Yurkov, “The Physics of Free Electron Lasers”, Springer (1999) and references therein

[5] A.M. Kondratenko, E.L. Saldin, *Part. Accelerators* **10**, 207 (1980)

[6] R. Bonifacio, C. Pellegrini, L.M. Narducci, *Opt. Commun.* **50** 373 (1984)

[7] H. Winick, et al., *Proc. PAC Washington* and SLAC-PUB-6185 (1993)

[8] R. Brinkmann, et al., *Nucl. Instr. and Meth.* **A 393** 86-92 (1997)

[9] R. Brinkmann, G. Materlik, J. Rossbach, A. Wagner (eds.), DESY 1997-048 and ECFA 1997-182 (1997)

[10] H.-D. Nuhn, J. Rossbach, *Synchrotron Radiation News* Vol. 13, No. 1, 18 – 32 (2000)

[11] W. Brefeld, et al., *Nucl. Instr. and Meth.* **A393** 119-124 (1997)

[12] T. Åberg, et al., A VUV FEL at the TESLA Test Facility at DESY, Conceptual Design Report, DESY Print TESLA-FEL 95-03 (1995)

[13] J. Rossbach, *Nucl. Instr. and Meth.* **A 375** 269 (1996)

[14] H. Weise, *Proc. 1998 Linac Conf.* Chicago, 674-678 (1998)

[15] J.-P. Carneiro, et al., *Proc. 1999 Part. Acc. Conf.*, New York 2027-2029 (1999)

[16] P. Michelato, et al., *Nucl. Instr. and Meth*. **A445,** *422* (2000)

[17] I. Will, S. Schreiber, A. Liero, W. Sandner, *Proc. 1999 FEL Conf*, Hamburg , II-99 (1999)

[18] S. Schreiber, et al., *Nucl. Instr. and Meth*. **A445** *427* (2000)

[19] Y. M. Nikitina, J. Pflüger, *Nucl. Instr. and Methods* **A375** 325 (1996)

[20] U. Hahn, et al., *Nucl. Instr. and Meth*. **A445,** *442* (2000)

[21] G. Schmidt, et al., this conference

[22] J. Pflüger, P. Gippner, A. Swiderski, T. Vielitz, *Proc. 1999 FEL Conf*, Hamburg, II-87 (1999)

[23] J. Pflüger, H. Lu, T. Teichmann, *Nucl. Instr. and Methods* **A429** 386 (1999)

[24] H. Edwards, et al., *Proc. 1999 FEL Conf.*, Hamburg, II-75 (1999)

[25] M. Geitz, G. Schmidt, P. Schmüser, G. v. Walter, *Nucl. Instr. and Meth*. **A445,** *343* (2000)

[26] M. Dohlus, A. Kabel, T. Limberg, *Proc. 1999 Part. Acc. Conf*., New York 1650-1652 (1999)

[27] P. Piot, et al., this conference

[28] Ch. Gerth, et al., this conference

[29] J. Andruszkow, et al. , accepted for publication in Phys. Rev. Lett. (2000)

[30] E. L. Saldin, E. A. Schneidmiller, M. V. Yurkov, *Nucl. Instr. and Meth.* **A 429** 233 (1999)

[31] R. Bonifacio, et al., *Phys. Rev. Lett*. **73** 70 (1994)

[32] E. L. Saldin, E. A. Schneidmiller, M. V. Yurkov, *Opt. Commun.* **148** 383 (1998)

Figure Captions:

Figure 1: Schematic layout of phase 1 of the SASE FEL at the TESLA Test Facility at DESY, Hamburg. The linac contains two 12.2 m long cryogenic modules each equipped with eight 9-cell superconducting accelerating cavities [14]. The total length is 100 m.

Figure 2: Sensitivity of radiation power to horizontal electron beam position at the undulator entrance. The dots represent mean values of the radiation intensity for each beam position. The horizontal error bars denote the rms beam position instability while the vertical error bars indicate the standard deviation of intensity fluctuations, which are due to the statistical character of the SASE process, see Eq. (3).

Figure 3: Wavelength of the central radiation cone (collimation angle ±0.2 mrad) as a function of electron beam energy. The FEL gain was typically >1000. The bunch charge was 1 nC.

Figure 4: Horizontal intensity profile of SASE FEL and spontaneous undulator radiation (x30), measured with a photodiode behind a 0.5 mm aperture in a distance of 12 m from the end of the undulator. The dotted line is the result of numerical simulation.

Fig. 5: Probability distribution of SASE intensity at 109 nm wavelength. The rms fluctuation yields a number of longitudinal modes M = 14. The solid curve is the gamma distribution for M = 14.4. The bunch charge is 1 nC.

Parameter	**Unit**	**Measured value for FEL experiment**
beam energy at undulator	MeV	181 - 272 MeV
rms energy spread	MeV	0.3 ± 0.2 MeV
rms transverse beam size	μm	100 ± 30 μm
ε_n (normalized emittance) in the undulator	π mrad mm	6 ± 3 π mrad mm
electron bunch charge	nC	1 nC
peak electron current	A	400 ± 200 A
bunch spacing	μs	1 μs
repetition rate	Hz	1 Hz
λ_u (undulator period)	mm	27.3 mm
undulator peak field	T	0.46 T
effective undulator length	m	13.5 m
typical betatron function horizontal/vertical		1.1 m
λ_{ph} (radiation wavelength)	nm	80 – 181 nm
FEL gain		10^3 - 10^4
FEL radiation pulse length	ps	0.4 – 1 ps

Table 1: Main parameters of the TESLA Test Facility for FEL experiments (TTF FEL, phase 1).

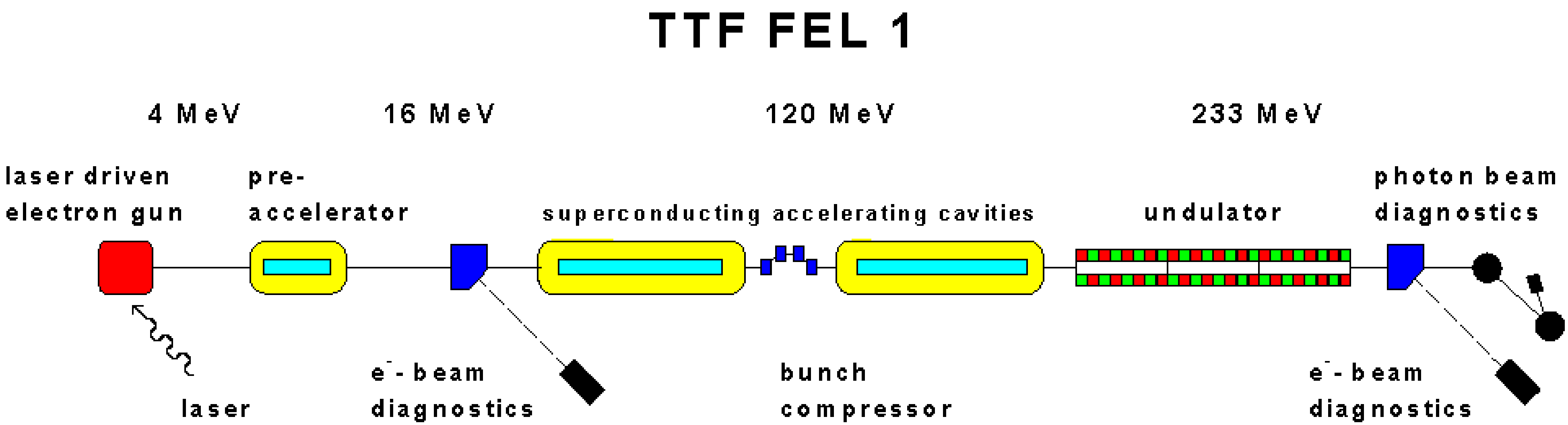
TTF FEL 1
4 MeV
16 MeV
120 MeV
233 MeV
laser driven electron gun
pre-accelerator
superconducting accelerating cavities
undulator
photon beam diagnostics
laser
e$^-$- beam diagnostics
bunch compressor
e$^-$- beam diagnostics

Figure 1

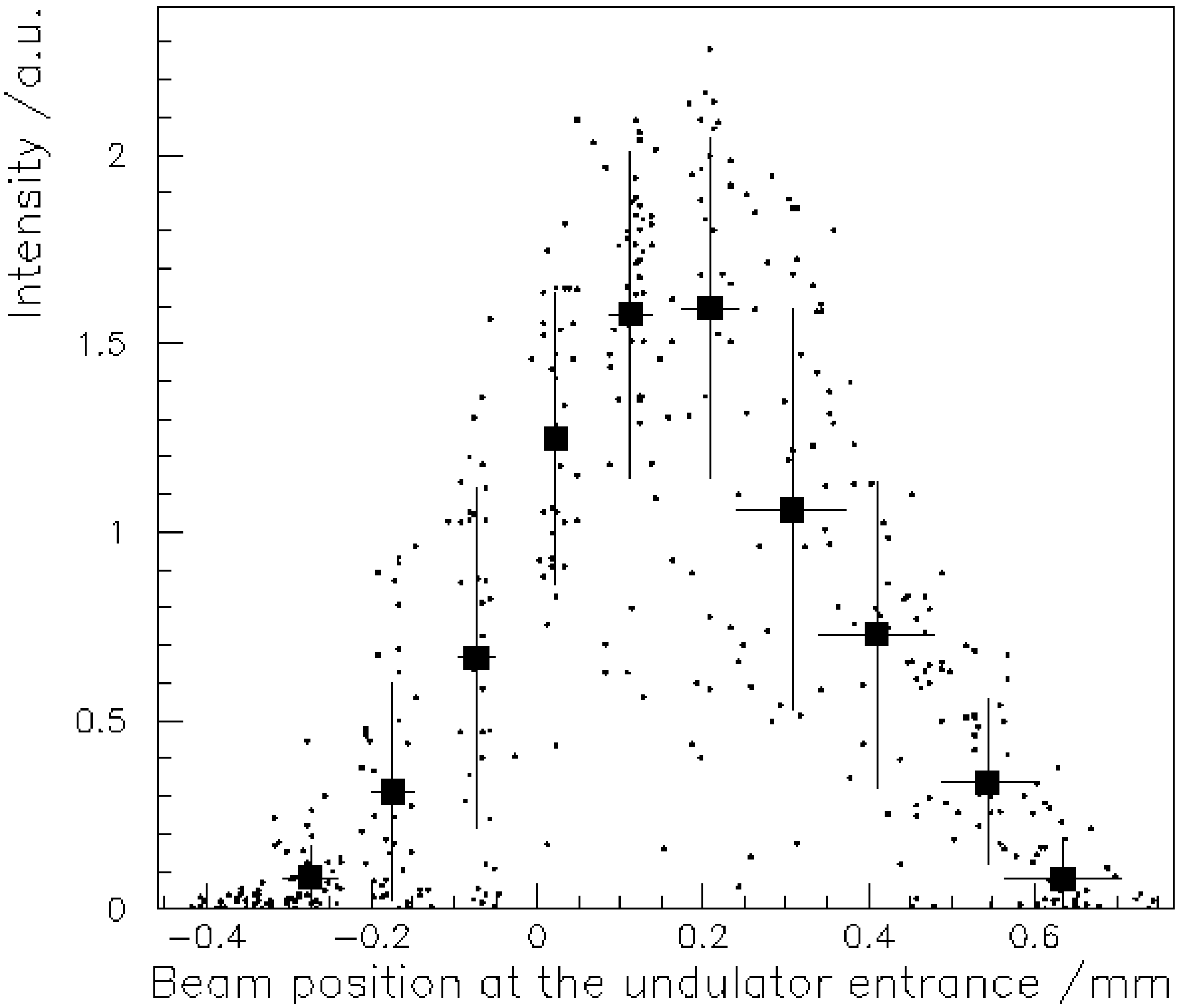

Intensity /a.u.
2
1.5
1
0.5
0
−0.4
−0.2
0
0.2
0.4
0.6
Beam position at the undulator entrance /mm

Figure 2

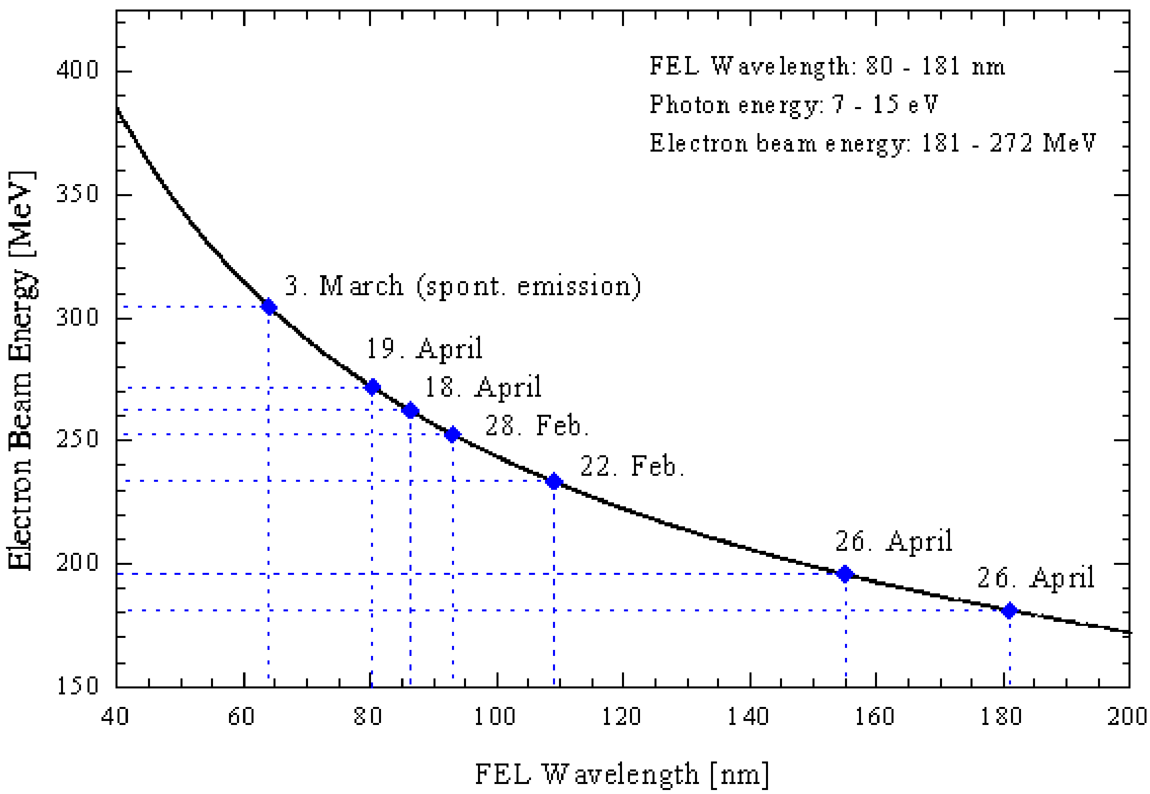
FEL Wavelength: 80 - 181 nm
Photon energy: 7 - 15 eV
Electron beam energy: 181 - 272 MeV
3. March (spont. emission)
19. April
18. April
28. Feb.
22. Feb.
26. April
26. April
Electron Beam Energy [MeV]
FEL Wavelength [nm]
400
350
300
250
200
150
40
60
80
100
120
140
160
180
200

Figure 3

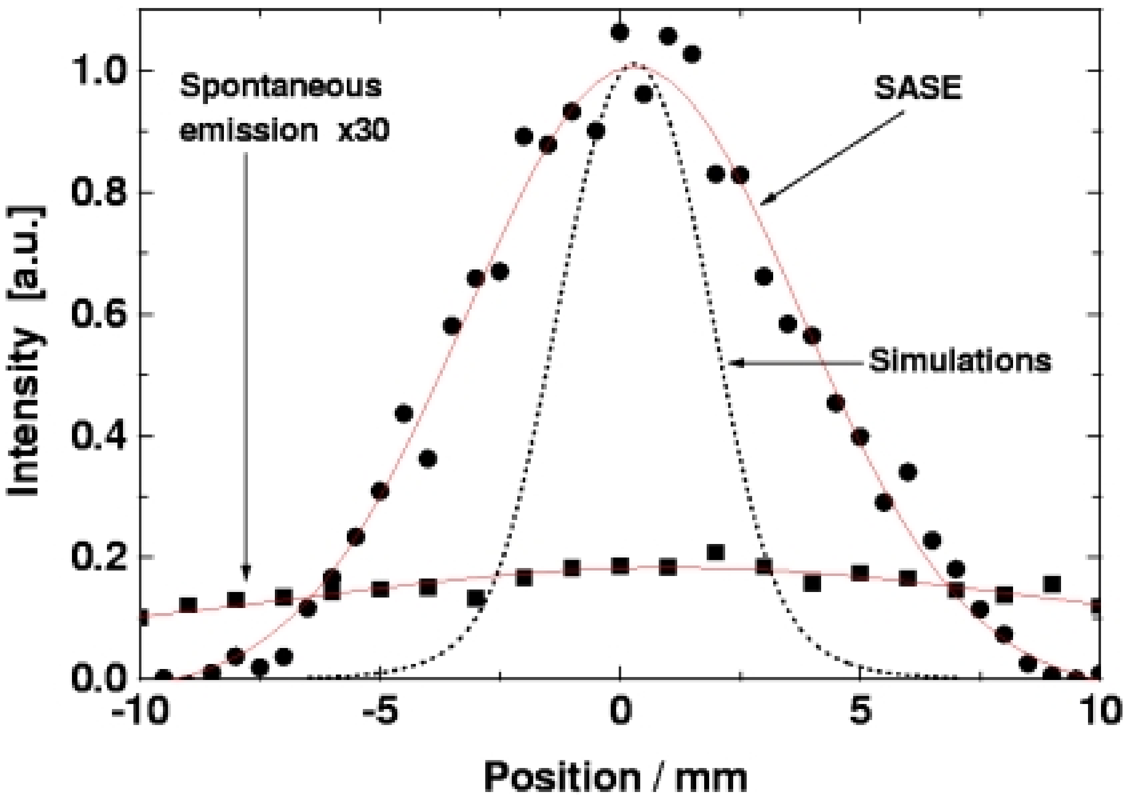

Spontaneous
emission x30
SASE
Simulations
Intensity [a.u.]
Position / mm
1.0
0.8
0.6
0.4
0.2
0.0
-10
-5
0
5
10

Figure 4

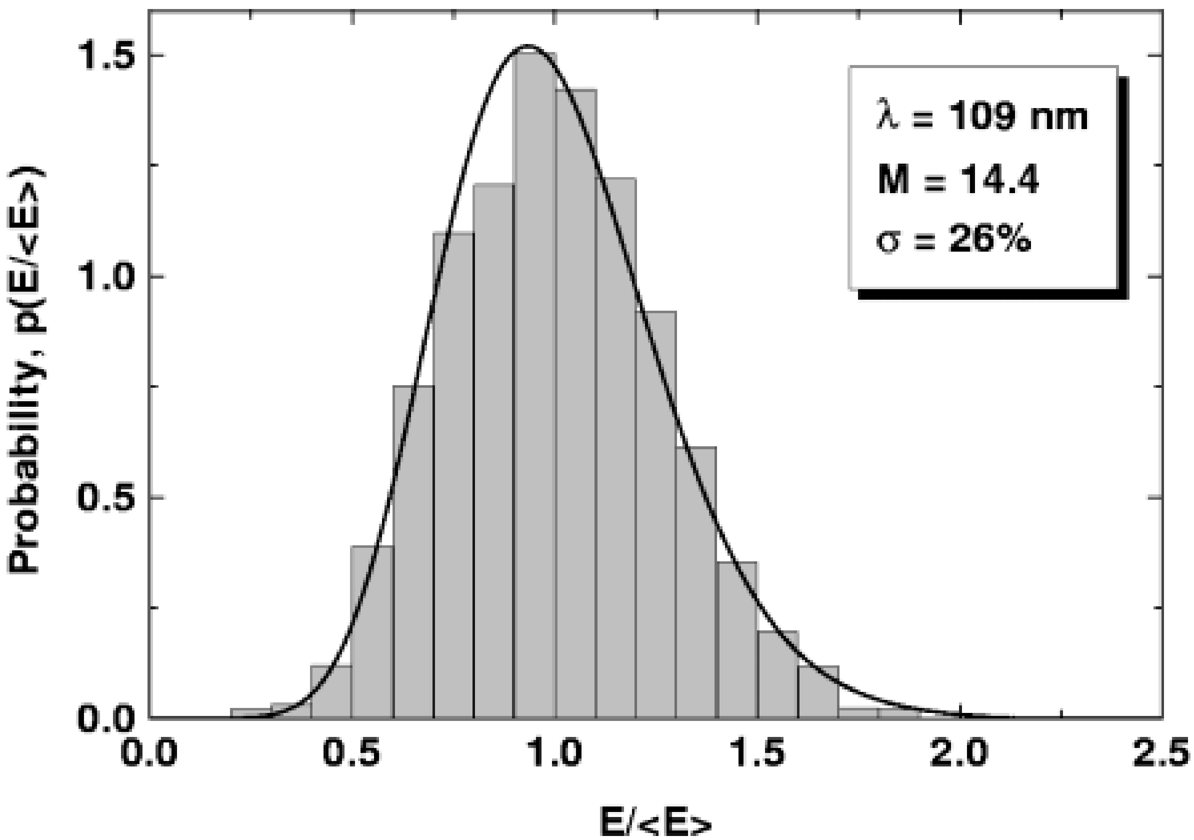

Figure 5

A Test of the Laser Alignment System ALMY at the TTF-FEL

S. Roth [a], S. Schael [b,1], G. Schmidt [a]

[a] *Deutsches Elektronen-Synchrotron DESY, Notkestraße 85, D-22603 Hamburg, Germany*

[b] *Max-Planck-Institut für Physik, Föhringer Ring 6, D-80805 München, Germany*

Abstract

The laser alignment system ALMY was tested at the 15 m long undulator section of the TESLA test facility. The positions of the undulator modules relative to each other have been determined with a precision of 0.1 mm, limited by the accuracy of the mechanical support of the sensors. Additionally, ALMY allows to measure movements or drifts over several days and we found that the undulator components are stable within 10 μm. The resolution of the sensors is better than 2 μm over a distance of 15 m.

[1] now at I. Phys. Inst., RWTH Aachen, D-52056 Aachen, Germany

1 Introduction

New alignment techniques have to be established for the construction of a future linear collider or light source. For the proposed TESLA collider [1] the integration of a X-ray free electron laser (FEL) is planned. It will use the effect of Self Amplified Spotanous Emission (SASE). In such SASE FEL a tightly focused electron beam of high charge density is sent through a long undulator. The focussing is achieved by separated or integrated quadrupoles. The SASE effect results from the interaction of the electron bunch with its own radiation field created by the motion inside the undulator. This interaction can only take place if the electron and the photon beams overlap. To keep the electron beam inside the undulator on a straight line the precise alignment of the individual undulator modules and the focusing elements with respect to each other is crucial.

A FEL working in the vacuum ultraviolett (VUV) has been constructed at the TESLA Test Facility (TTF). At the TTF-FEL [2] the electron beam position must be straight with transverse deviations of less than 10 μm rms over the entire 15 m long undulator. Therefore the magnetic axis of the undulator with a superimposed FODO structure must be aligned with about the same accuracy. For the alignment of the three individual undulator segments a commercially available interferometer system has been used which reaches a precision of the order of 5 μm. The alignment system uses reference marks on the undulator which have a known offset to the magnetic axis of the undulator. The magnetic axis of the whole undulator is estimated to be straight within 30 μm [3].

As the laser interferometer is a manual system it has the disadvantage that it cannot be used during operation of the machine. Therefore it cannot deliver a continous monitoring of the positions of the undulator components. As an alternative we tested the ALMY [5] system. It is a multi-point alignment system that has been developed for the muon spectrometer of the ATLAS detector at the Large Hadron Collider. It uses an infrared laser beam, acting as alignment reference, which transverses several transparent silicon sensors. The sensors measure the laser beam position in both transverse coordinates. Thermal effects like density fluctuations of the air can influence the straightness of the laser beam. Such effects are shielded by means of an aluminium tube around the laser beam.

2 The Transparent Silicon Sensors and the ALMY System

The optical sensors have to combine high position resolution and high light transmission. To optimize the transmission thin films of amorphous silicon (a-Si) are used as photo-sensitive material. The amorphous silicon strip sensors were produced at Heimann Optoelectronics and provide high precision position measurement at relatively low cost. CVD techniques are used to deposit the 1 μm thick photo-sensitive layers onto a 0.5 mm thick glass substrate. High-quality polished parallel glass wafers minimise uncertainties in the deflection of the transversing laser beam. The a-Si film is sandwiched by two 0.1 μm thick electrodes of indium-tin oxide (ITO) which are segmented into two orthogonal strip rows. The bottom electrode acts as ohmic contact while the top electrode forms a Shottky diode which is operated at about 3 V bias voltage. The strip pitch of about 300 μm has been optimized to the typical laser beam diameters of 3–5 mm. The structure of the sensors is shown in Fig. 1. Position resolutions of 1 μm over the whole sensor surface have been measured and transmission rates above 90% at $\lambda = 790$nm have been achieved [5].

The readout electronics is integrated inside the sensor module. In Fig. 2 a complete sensor module is shown. The photocurrents of all strips are multiplexed, amplified and digitized. These values are stored into a memory which can be readout by a VME bus system. The system can be read out with a rate which is limited to about one measurement per second at maximum.

3 The Test Setup

The undulator of the TTF-FEL consists of three undulator modules interspersed with four diagnostic modules containing wire scanners and beam position monitors [4]. The magnetic axis of the individual undulator modules itself has been measured using a 12 m long bench [3]. To build the undulator section inside the linac tunnel both ends of each undulator module and the diagnostic modules have to be lined up. As the alignment is done seperatly for the horizontal and the vertical coordinate this gives in total 20 reference marks.

In Fig. 3 a view along the TTF undulator section is shown. For a first test of the ALMY system the sensors were placed at the alignment marks which determine the horizontal positions. Because of lack of space the last alignment mark has been used for installation of the laser optics. The laser sends a collimated laser beam with a diameter of 3–5 mm through all nine sensors. The laser beam is shielded against temperature gradients and fluctuations using aluminium tubes.

The readout of the silicon strip detectors is done by each sensor module individually and the digitized signal height of each strip is sent via RS232 connection to a data aquisition program running on a PC. Here a Gauss fit is performed to the shape of the measured beam profiles. The mean value from this fit is taken as the position measurement.

4 Measurement Results

The laser alignment system ALMY has shown that it works within the background of radiation and electronic noise of the linac tunnel. It took data without any interruption during five days of linac operation with electron beam. Nine detectors were installed.The positions and movements of the sensors could be monitored all the time during this period.

A comparison between the measured positions and the design positions of the alignment marks can be seen in Fig. 4. The design position of the reference marks contains the offset of the reference mark to the magnetic axis of the undulator. The difference of measurement and design gives the displacement of the individual components to the magnetic axis of the undulator. It is shown in the lower part of Fig. 4. The measurement error is influenced mainly by the mechanical assembly of the sensors onto the alignment marks which has a precision in the range of 0.1 mm. Within this error one would conclude from this measurement that the undulator forms a straight line with exception of the components at both ends of the undulator section.

The setup has been operated in the linac for 4 days. Every 30 seconds a measurement was performed and the result written to disk. This allowed us to monitor the sensor positions continously and to look for movements of the individual components, either in form of oscillations or in form of drifts. The result is shown in Fig. 5. One observes oscillations of the measured result with amplitudes of up to 50 μm and periods of about 40 minutes. As can be seen in Fig. 6 these oscillations are correlated with the temperature variations in the climatized hut, where the undulator is placed. The amplitude is proportional to the distance of the sensor from the laser.

The observed oscillations are caused by changes of the laser beam direction by 3 nrad due to the temperature change of 0.3 °C. As we are not interested in movements of the reference laser beam but in potential movements of the undulator components with respect to each other we put again a straight line through two of the components. The difference of the measured position from the straight line is then independent of changes in the laser beam direction. The result is shown in the bottom part of Fig. 5 and shows that the corrected measurements show a reduced dependence on the temperature variations.

During a period of about one hour we took data every second. These data are analysed in Fig. 7. First all measurements are shown corrected for the changes of the laser beam direction as explained before. The next plot of Fig. 7 gives the mean value of these single measurements averaged over five minutes. The resulting curve is much smoother than before and movements in the micron range are easily detectable. The resulting curves are showing the movement of the individual sensors to the reference axis. The spatial resolution of the sensors is calculated out of the position noise and it varies between 0.7 μm near the tail of the laser beam and 2 μm at both ends of the alignment distance.

A comparision with other alignment methods is shown in Fig. 8. In between the expectable errors the measurements show good agreement. Only at both ends of the undulators some deviations are visible. Further investigations are needed to understand if there are systematic errors explaining this effect.

5 Conclusions

The laser alignment system ALMY was shown to work within the background of radiation and electronic noise inside the linac tunnel. With an improved fixation of the sensors to the undulator and individually calibrated sensors the ALMY system it will be possible to measure online the position of the undulator components with an accuracy of better than 0.03 mm. Nevertheless further test should be done here at DESY to investigate if the number of sensors can be increased without reducing the accuracy of the measurement and to check the usable distance where the ALMY system works.

However it should be possible to use ALMY as a fast alignment system for complete beam line sections which could be up to 15 m long.

6 Acknowledgments

We would like to thank J. Brehling and the HASYLAB workshop for the construction of the detector mounting and T. Vielitz for his help during the installation of the test setup at the TTF undulator section.

References

[1] R. Brinkmann, G. Materlik, J. Rossbach, A. Wagner (eds.), DESY 1997–048 and ECFA 1997–182, May 1997.

[2] TTF-FEL Conceptual Design Report, TESLA-FEL 95-03, DESY, June 1995; J. Rossbach *et al.*, Nucl. Instr. and Meth. **A375** (1996) 269.

[3] J. Pflüger, H. Lu, T. Teichmann, Nucl. Instr. and Meth. **A429** (1999) 386.

[4] U. Hahn, J. Pflueger, G. Schmidt, Nucl. Instr. and Meth. **A429** (1999) 276.

[5] W. Blum, H. Kroha, P. Widmann, Nucl. Instr. and Meth. **A377** (1996) 404. M. Fernandez Garcia *et al.*, "Semi-Transparent Silicon Strip Sensors for the Precision Alignment of Tracking Detectors", Contribution to "Frotier Detectors for Frontier Physics", La Biodola, Isola d'Elba, May 21-27, 2000.

[6] J. Pflüger *et al.*, DESY group HASYLAB, private communication.

[7] J. Prenting *et al.*, DESY group ZMEA, private communication.

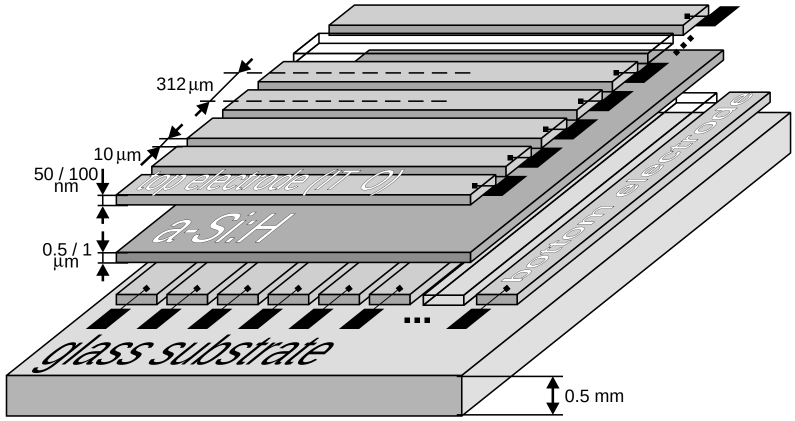

Fig. 1. Cross section of the photosensitive detector.

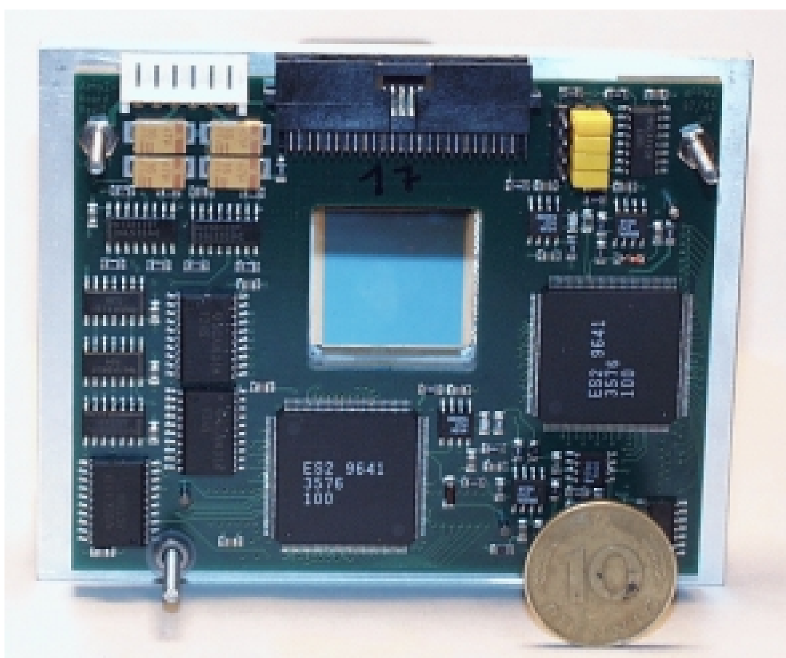

Fig. 2. Complete module including sensor and readout electronics is shown.

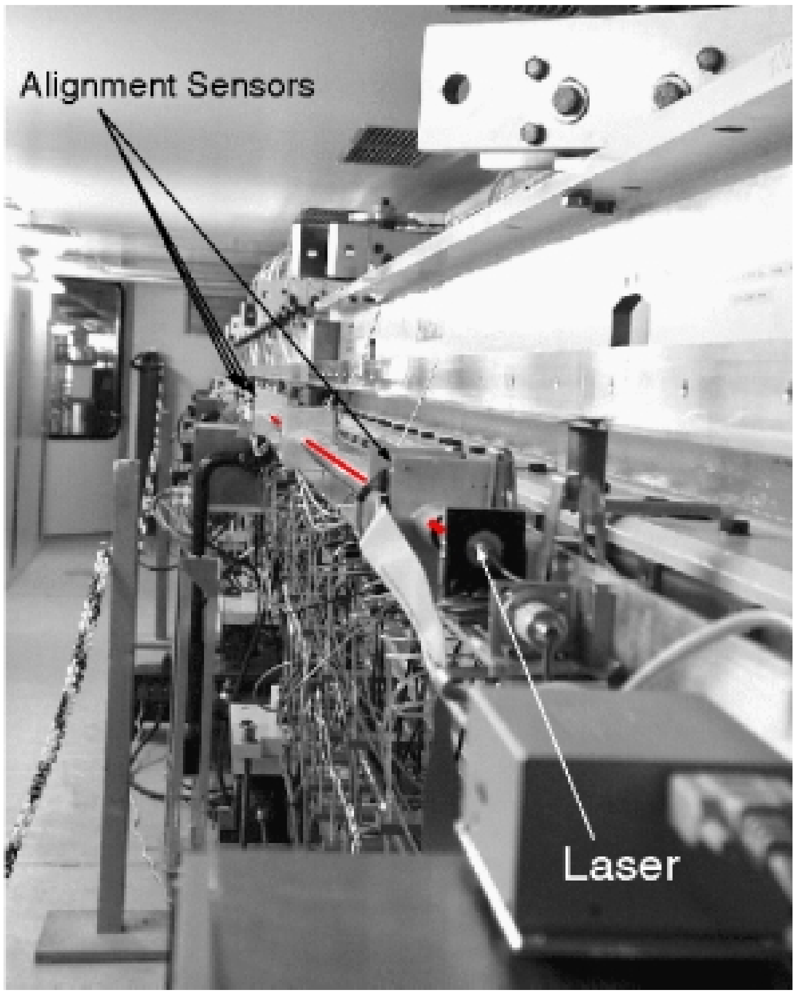

Fig. 3. Test setup of the laser alignment system at the TTF undulator

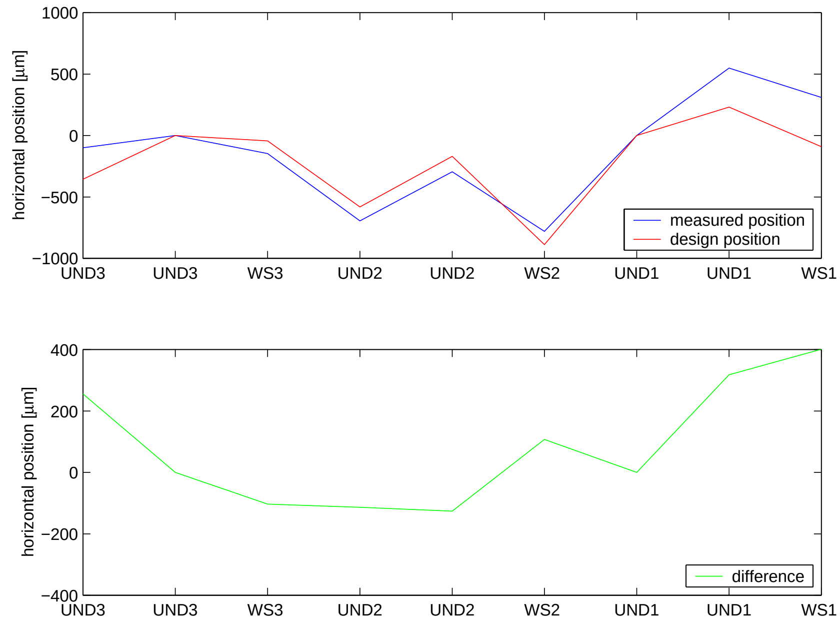

Fig. 4. Result of the alignment measurement. Shown are the positions of the three undulator modules (UND1, UND2, UND3) and of three of the four diagnostic monitors (WS1, WS2, WS3)

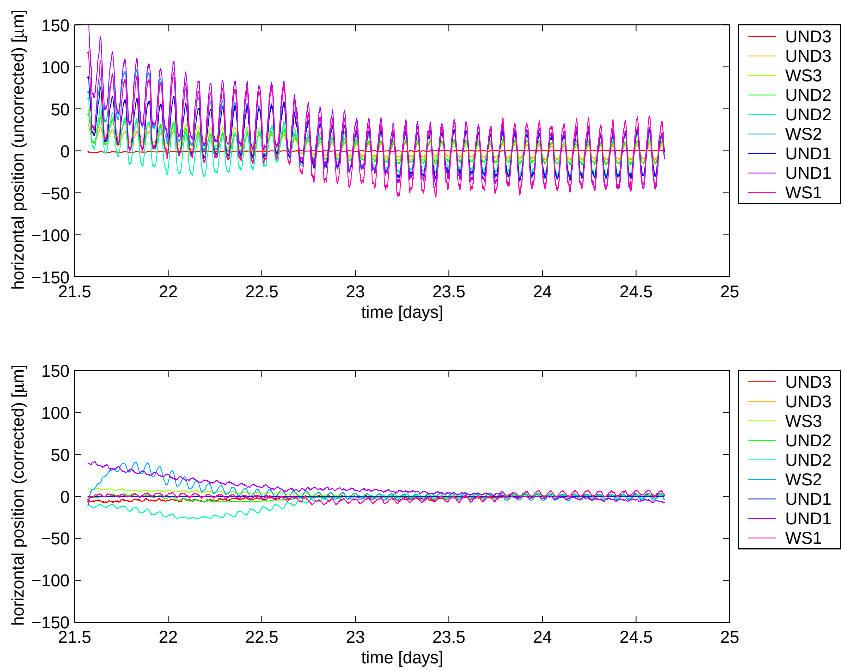

Fig. 5. Comparison between raw data and corrected data.

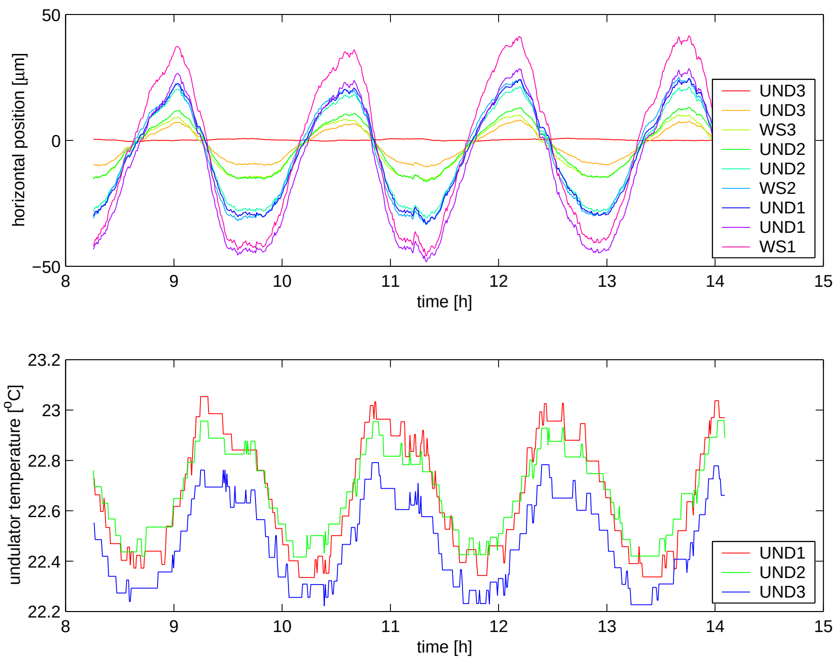

Fig. 6. Correlation between sensor alignment and temperature.

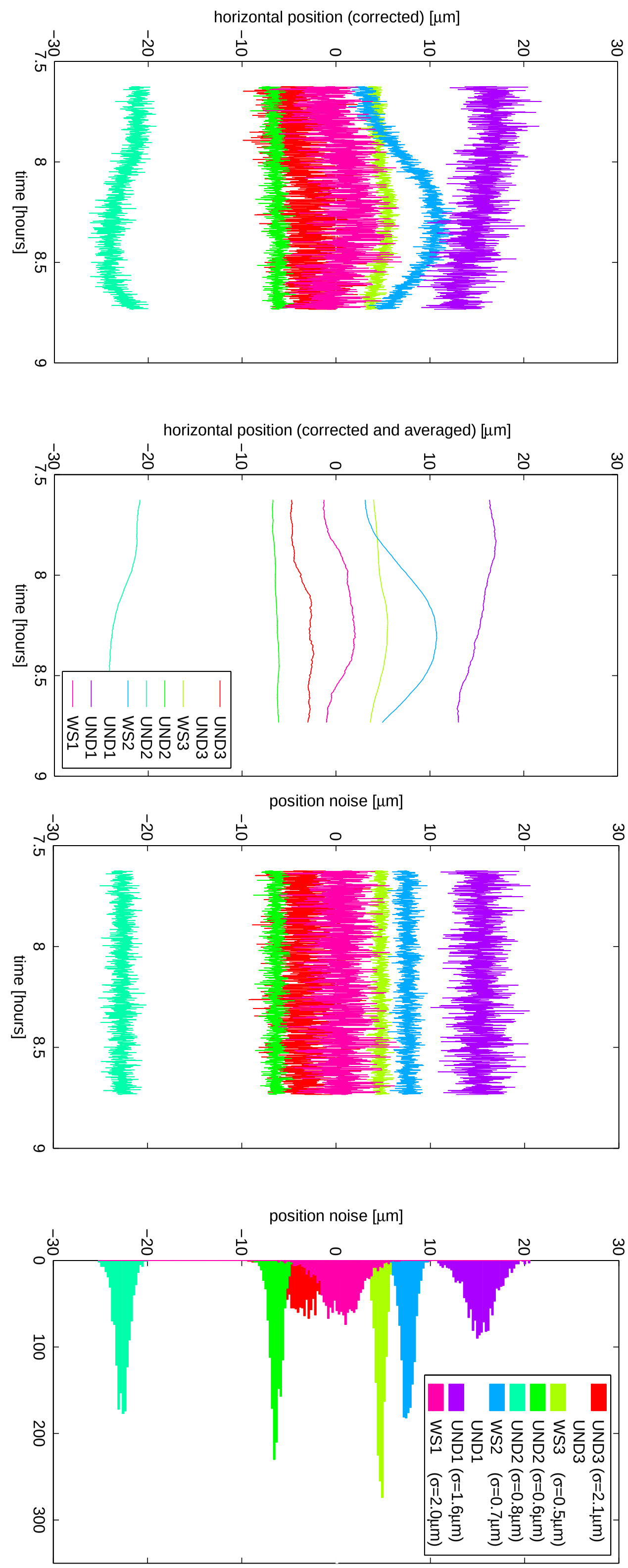

Fig. 7. Sensitivity and spatial resolution of the sensors in the current alignment setup.

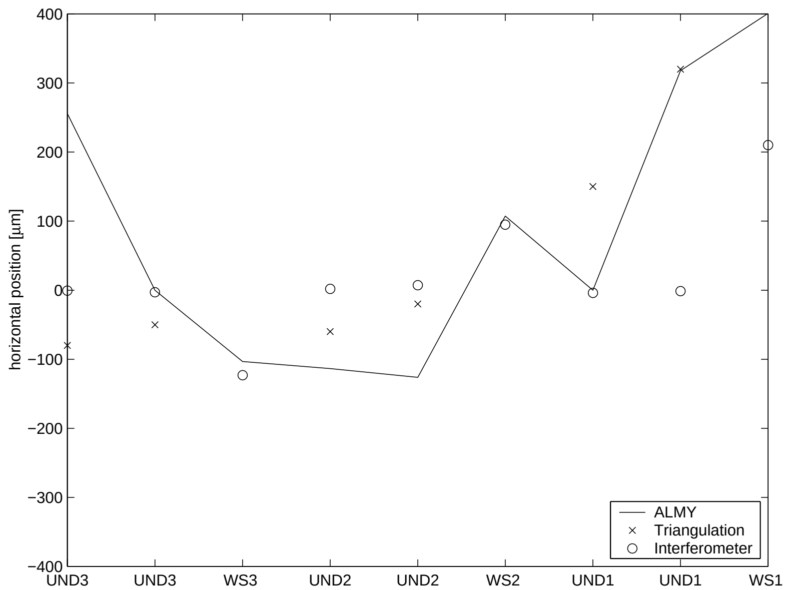

Fig. 8. Comparison of three different alignment measurements

X-ray FEL with a meV Bandwidth

E.L. Saldin [a], E.A. Schneidmiller [a], Yu.V. Shvyd'ko [b], M.V. Yurkov [c]

[a] *Deutsches Elektronen-Synchrotron (DESY), Notkestrasse 85, D-22607 Hamburg, Germany*

[b] *II. Institut für Experimentalphysik, Universität Hamburg, D-22761 Hamburg, Germany*

[c] *Joint Institute for Nuclear Research, Dubna, 141980 Moscow Region, Russia*

Abstract

A new design for a single pass X-ray Self-Amplified Spontaneous Emission (SASE) FEL was proposed in [1] and named two-stage SASE FEL. The scheme consists of two undulators and an X-ray monochromator located between them. For the Angström wavelength range the monochromator could be realized using Bragg reflections from crystals. Proposed scheme of monochromator is illustrated for the 14.4 keV X-ray SASE FEL being developed in the framework of the TESLA linear collider project. The spectral bandwidth of the radiation from two-stage SASE FEL (20 meV) is defined by the finite duration of the electron pulse. The shot-to-shot fluctuations of energy spectral density are dramatically reduced in comparison with the 100 % fluctuations in a SASE FEL. The peak and average brilliance are by three orders of magnitude higher than the values which could be reached by a conventional X-ray SASE FEL.

1. Introduction

A single pass X-ray SASE FEL [2,3] can be modified as proposed in [1] in order to reduce significantly the bandwidth and the fluctuations of the output radiation. The proposed scheme consists of two undulators and an X-ray monochromator located between them. The first undulator operates in the linear regime of amplification starting from noise and the output radiation has the usual SASE properties. After the exit of the first undulator the electron is guided through a bypass and the X-ray beam enters the monochromator which selects a narrow band of radiation. At the entrance of the second undulator the monochromatic X-ray beam is combined with the electron beam and is amplified up to the saturation level.

The electron micro-bunching induced in the first undulator should be destroyed prior to its arrival at the second one. This is achieved automatically due to the natural energy spread when the electron beam goes through a bypass. At the entrance of the second undulator the radiation power from the monochromator dominates significantly over the shot noise and the residual electron bunching, so that the second stage of the FEL amplifier will operate in a regime when the input signal bandwidth is small with respect to the FEL amplifier bandwidth.

The monochromatization of the radiation is performed at a relatively low level of radiation power which allows one to use conventional X-ray optical elements for the monochromator design. X-ray grating techniques can be used successfully down to wavelengths of several Å and at shorter wavelengths crystal monochromators could be used.

The proposed scheme possesses two significant advantages. First, it opens a perspective to achieve monochromaticity of the output radiation close to the limit given by the finite duration of the electron pulse and to increase the brilliance of the SASE FEL. Second, shot-to-shot fluctuations of the energy spectral density could be reduced from 100 % to less than 10 % when the second undulator section operates at saturation. Since it is a single bunch scheme, it does not require any special time diagram of the accelerator operation.

The conditions that are necessary and sufficient for the effective operation of a two-stage SASE FEL were discussed in [1] and can be summarized as follows

$$P_{\mathrm{in}}^{(2)}/P_{\mathrm{shot}} = G^{(1)} R_{\mathrm{m}} (\delta\lambda/\lambda)_{\mathrm{m}}/(\delta\lambda/\lambda)_{\mathrm{SASE}} \gg 1 \ , \tag{1}$$

$$\lambda/\pi\sigma_{\mathrm{z}} < (\delta\lambda/\lambda)_{\mathrm{m}} \ll (\delta\lambda/\lambda)_{\mathrm{SASE}} \ , \tag{2}$$

$$G^{(1)} \ll G_{\mathrm{sat}}(\mathrm{SASE}) \ . \tag{3}$$

Here $P_{\mathrm{in}}^{(2)}$ is the input radiation power at the entrance to the second undulator, P_{shot} is the effective power of shot noise, $G^{(1)}$ is the power gain in the first undulator, R_{m} is the integral reflection coefficient of the mirrors and the dispersive elements of the monochromator, $(\delta\lambda/\lambda)_{\mathrm{m}}$ is the resolution of the monochromator, $(\delta\lambda/\lambda)_{\mathrm{SASE}}$ is the radiation bandwidth of the SASE FEL at the exit of the first undulator, σ_{z} is the rms length of the electron bunch, and $G_{\mathrm{sat}}(\mathrm{SASE})$ is the power gain of SASE FEL at saturation.

An application of such a two-stage scheme to 6 nm SASE FEL at the TESLA Test Facility at DESY [4] was discussed in [1,5]. Now it is funded and is expected to be the main option for operation of the user facility. In this paper we consider a possible design of the two-stage FEL operating in the Angström range for the X-ray laboratory integrated into the TESLA linear collider project [6]. To be specific we consider the FEL optimized for 14.4 keV X-rays (0.86 Å). Special interest for the 14.4 keV X-rays is due to additional possibilities which the powerful and diverse nuclear resonance scattering techniques with the highly monochromatic 14.4 Mössbauer radiation [7] open for studies of structure and dynamics of solids, biological molecules, etc.

Table 1
Parameters of the electron beam and the undulators

Electron beam	
Energy, $\mathcal{E}_0$	25 GeV
Peak current, I_0	5 kA
rms bunch length, σ_z	23 μm
Normalized rms emittance, ϵ_n	1.6π mm mrad
rms energy spread (entrance)	2.5 MeV
External β-function	45 m
Bunch separation	93 ns
Number of bunches per train	11315
Repetition rate	5 Hz
Undulator	
Type	Planar
Period, λ_w	4.5 cm
Peak magnetic field, H_w	9.5 kGs

2. Parameters of the two-stage X-ray FEL

Main parameters of the electron beam and the undulators are presented in Table 1 and coincide with those of usual SASE FEL at 14.4 keV being designed for TESLA. The SASE FEL bandwidth at the exit of the first stage is about 7×10^{-4} and weakly depends on the gain. We require the monochromator FWHM bandwidth to be about 20 meV, or 1.4×10^{-6} (see (2)). The integral reflection coefficient of all the crystals of the monochromator is expected to be in a range of 0.3 - 0.5. Requiring the excess of the input radiation power at the entrance to the second undulator $P_{\mathrm{in}}^{(2)}$ over the effective power of shot noise P_{shot} to be two orders of magnitude (see (1) and [5]) we end up with the gain of 1.5×10^5 in the first undulator. The SASE FEL gain at the saturation would be about 4×10^6 so that the condition (3) is satisfied.

Parameters of the first and the second stages are presented in Table 2. They has been calculated with the FEL simulation code FAST [8]. Let us note that when calculating these parameters we have taken into account the growth of energy spread in the electron beam due to the quantum fluctuations of undulator radiation [9,10]. The peak and average brilliance of the X-ray beam at the exit of the second stage are 500 times larger than in the case of usual SASE FEL. The shot-to-shot fluctuations of the energy spectral density are reduced to the 10% level due to nonlinear stabilization mechanism [5].

The distance between the two undulators is mainly defined by parameters of the electron beam bypass (chicane) that must compensate a path delay of X-rays in the monochromator. The latter is assumed to be of the order of 1 cm. For the bending angle of chicane magnets equal to 3×10^{-3} the total length of the chicane will be about 40 m. The electron beam microbunching will be completely destroyed at the end of the bypass due to the uncorrelated energy spread in the beam and reasonable longitudinal dispersion of the chicane [1]. Due to the small angular divergence of radiation coming out of the first un-

Table 2
Parameters of the first and the second stages

1st stage	
Wavelength, λ	0.860 Å
Effective power of shot noise, $P_{\rm shot}$	5 kW
Length of undulator, $L_{\rm w}^{(1)}$	140 m
FWHM bandwidth , $(\delta\lambda/\lambda)_{\rm SASE}$	7×10^{-4}
Radiation spot size (FWHM)	50 μm
Angular divergence (FWHM)	1 μrad
Peak power	0.75 GW
Average power	4 W
2nd stage	
Input power, $P_{\rm in}^{(2)}$	0.5 MW
Length of undulator, $L_{\rm w}^{(2)}$	170 m
FWHM bandwidth , $\delta\lambda/\lambda$	1.4×10^{-6}
Angular divergence (FWHM)	0.7 μrad
Radiation spot size (FWHM)	110 μm
Peak power	20 GW
Average power	110 W
Peak brilliance	3×10^{36} Phot./(sec$\times$mrad$^2\times$mm$^2\times$0.1 % bandw.)
Average brilliance	2×10^{28} Phot./(sec$\times$mrad$^2\times$mm$^2\times$0.1 % bandw.)

Table 3
Parameters of the monochromator and the electron beam bypass

Monochromator	
Nominal energy	14.4 keV
Bandwidth	20 meV
Tunability range	2-4 keV
Total reflection coefficient	0.3 - 0.5
Absorbed average power	$<$ 200 mW
Absorbed average power density	$<$ 50 W/mm^2
Electron beam bypass (chicane)	
Total length	40 m
Bending angle of magnets	0.03
Path lengthening	1 cm

dulator, the focusing of this radiation is not necessary. Indeed, calculations show that the input coupling factor [11] to the eigenmode in the second undulator decreases by about 30% with respect to the case of optimal focusing. Main parameters of the monochromator and the electron beam bypass are presented in Table 3.

3. High energy-resolution, high heat-load, tunable X-ray monochromator

The main requirements to the X-ray monochromator of the two stage XFEL are
i. degree of monochromatization: $\lambda/\delta\lambda = E/\delta E = 0.7 \times 10^6$;
ii. tunability range: a few keV;

iii. resistance to the high heatload.

To reach the required value of monochromatization alone is not a problem. Nowadays a monochromatization of 10^7 and more is possible. Bragg diffraction is the main tool used for such purposes. For a recent review of the techniques used and achievements in this field see, e.g., [12]. However, the combination of the three requirements renders the realization of such a monochromator not so straightforward.

3.1. Spectral width of Bragg reflections and tunability range.

Tunability of an X-ray monochromator for a given monochromaticity will be addressed first.

The relative energy width of a Bragg reflection in a thick nonabsorbing crystal (like silicon, diamond, etc) is given in the dynamical theory of diffraction in perfect crystals (see, e.g., [13]) by

$$\frac{\delta E}{E} = \frac{\delta\lambda}{\lambda} = \frac{|\chi_{\mathrm{g}}|}{\sin^2\theta}.$$

Here θ is the glancing angle of the radiation plane wave to the reflecting atomic planes (hkl) with the interplanar distance d_{hkl} and the related reciprocal vector $\mathbf{g}$ where $|\mathbf{g}| = 2\pi/d_{hkl}$. The relation between the wavelength λ of the reflected x rays and θ is given by the Bragg law $2d_{hkl}\sin\theta = \lambda$.

$$\chi_{\mathrm{g}} = -\frac{r_{\mathrm{e}}\lambda^2}{\pi V} Z\, f\left(\frac{\sin\theta}{\lambda}\right) \exp\left(-\frac{\langle u^2\rangle}{\lambda^2} 8\pi^2\sin^2\theta\right)$$

is the Fourier component of the electric susceptibility corresponding to the reciprocal vector $\mathbf{g}$. The expression is valid for a single atom crystal. Here the following notations are used: V is the volume of the crystal unit cell; Z is atomic number; r_{e} is the classical electron radius; $f(\ldots)$ is the atomic scattering formfactor; and $\exp(\ldots)$ is the Debye-Waller factor with $\langle u^2\rangle$ as the mean square displacement of atoms in the direction of the scattering vector $\mathbf{g}$ due to thermal vibrations. The combination of the both equations gives

$$\frac{\delta E}{E} = \frac{r_{\mathrm{e}}\lambda_{hkl}^2}{\pi V} Z\, f\left(\lambda_{hkl}^{-1}\right) \exp\left(-8\pi^2\frac{\langle u^2\rangle}{\lambda_{hkl}^2}\right). \tag{4}$$

Here the Bragg wavelength $\lambda_{hkl} = 2d_{hkl}$ is introduced - the largest wavelength of X-rays allowed to be reflected from the (hkl) atomic planes by the Bragg law.

An important and very favorable implication of eq. (4) for our applications is that the relative spectral width for the given Bragg reflection (hkl) is independent of the energy or glancing angle of X-rays and defined merely by properties of the crystal and reflecting atomic planes. In particular it implies that the choice of a crystal, reflecting atomic planes and crystal temperature determines the spectral resolution. Figure 1 shows results of evaluations of the monochromaticity $E/\delta E$ of X-rays reflected from different atomic planes (hkl) in diamond (C) and silicon (Si) single crystals at room temperature. The range of tunability is limited only by the lowest X-ray energy allowed by the Bragg law - the Bragg energy $E_{hkl} = hc/\lambda_{hkl}$.

The 1 μrad divergency (FWHM) of X-rays from the first undulator were also taken into account, which shows up in the decreasing monochromaticity with raising X-ray energy. This occurs when the angular acceptance of Bragg reflections approaches the angular divergence of the incoming beam.

As it is seen from Fig. 1 the number of possible reflections which provide required monochromaticity and tunability range is rather limited. In case of diamond (C), these are (137) or (117) and equivalent ones. In case of silicon single crystals these are (139) or (339) and equivalent ones.

We are discussing here only silicon and diamond single crystals. There are two reasons for this. Si single crystals are the most perfect crystals available nowadays. This is an important feature which ensures the preservation of the coherent properties of the radiation from the first undulator. Diamond although not so perfect as silicon, nevertheless sufficiently large $\approx 10 \times 10 \times 1$ mm^3 perfect crystals are available already now [14]. The greatest advantage of diamond is its ability to withstand the high heat load due to the extremely high thermal conductivity, low thermal expansion, small X-ray absorption, and high reflectivity.

3.2. Actual scheme

We have chosen the 4-bounce scheme of the X-ray monochromator as shown in Fig. 2. This solution is advantageous as it allows to keep the direction and the position of the X-ray beam at the exit the same as at the entrance of the monochromator.

This solution is advantageous also due to the possibility to use the first two Bragg reflectors as a high-heat load premonochromator, which withdraws the major heat load from the actual high energy-resolution monochromator - the third and the forth crystals. In the pre-monochromator part one can use, e.g., diamond crystal plates of a 100 μm thickness and the reflection C(004). Given the crystal is perfect, it reflects 99% of the incident X-rays within a band of 132 meV. Only 5% of the off-band radiation is absorbed, and the rest passes through. The absorbed power is thus 20 times less than the incident one and is about 200 mW. The absorbed power density is about 50 W/mm^2. It is comparable with that at the monochromators of the 3rd generation synchrotron sources [15]. The radiation power which reaches the high resolution monochromator crystals is $\simeq 1.3\%$ of the initial value. The latter can be reduced by a factor of two if to use the reflection C(133) with a bandwidth of 75 meV.

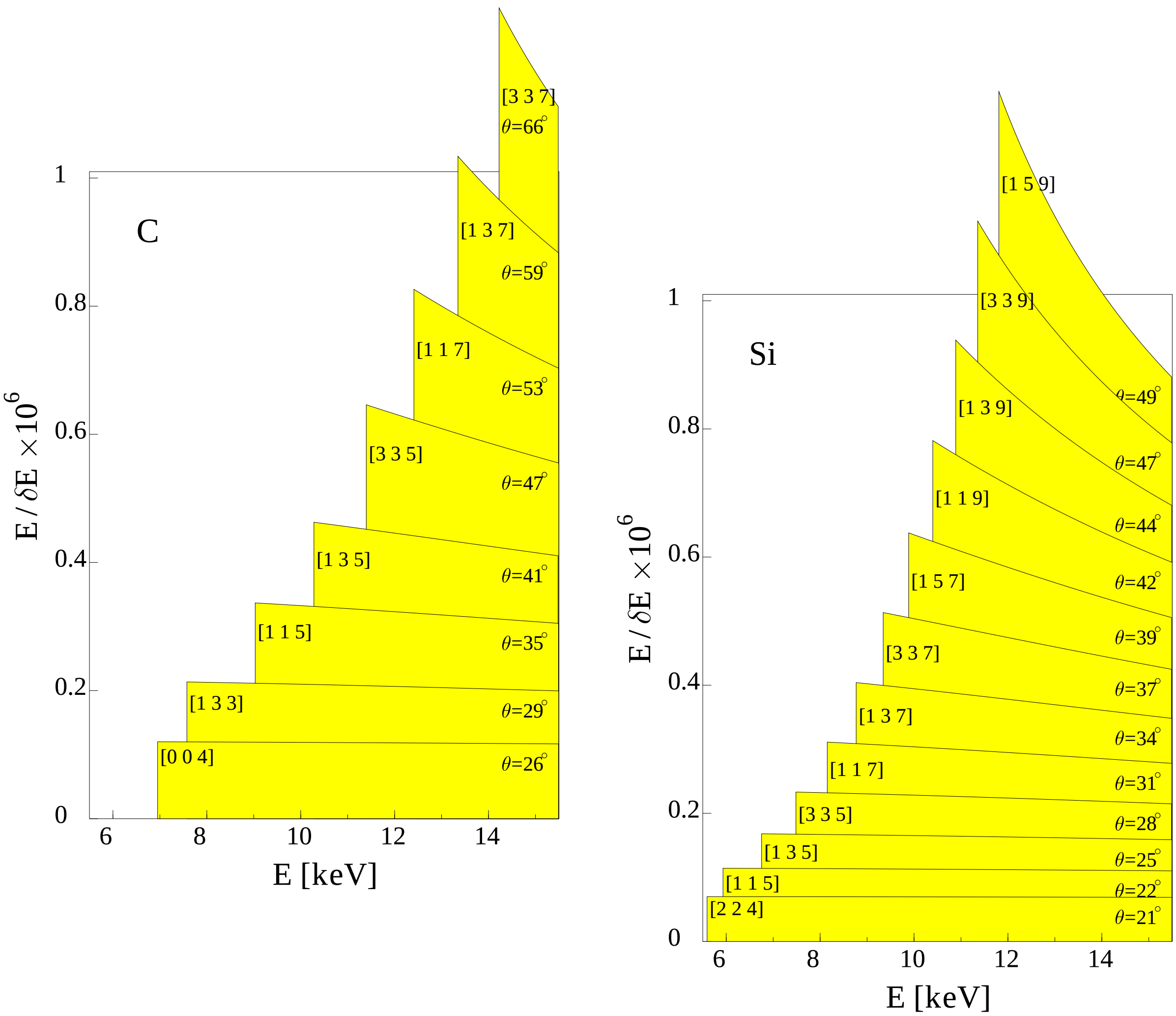

Fig. 1. Degree of monochromatization $E/\delta E$ of X-rays reflected from the atomic planes (hkl) in diamond (C) and silicon (Si) single crystals at room temperature. The divergence of the incident X-rays is assumed to be 1 μrad. At the right end of each graph the glancing angle θ is given corresponding to the highest X-ray energy $E = 15.5$ keV considered.

The final monochromatization to the required level takes place by a high-index reflection in the third and the forth crystals. The required monochromatization $E/\delta E = 0.7 \times 10^6$ of the 14.4 keV X-rays can be achieved, according to Fig. 1, by only a very limited number of reflections. The final choice of the reflection should be dictated by the requirements of tunability and heatload. The Bragg reflection in diamond has a smaller tunability range. On the other hand it has higher reflectivity and angular acceptance as well as better thermal properties. Fine adjustment of the angular acceptance and the energy bandwidth can be performed by using asymmetric Bragg reflections.

An important technical issue is a path delay (with respect to the straight path) which

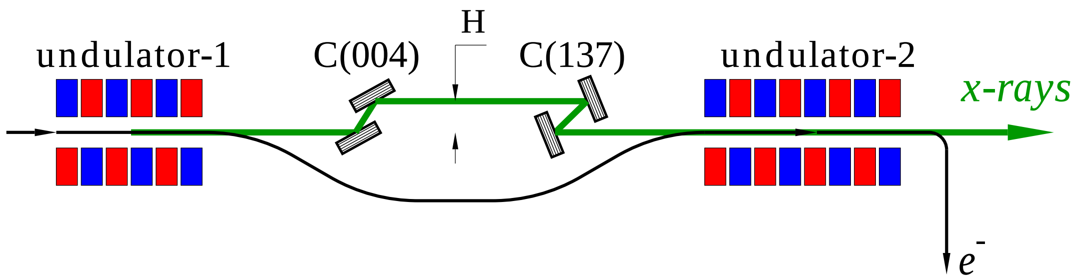

Fig. 2. The two-stage XFEL with the 4-bounce X-ray monochromator: C(004) × C(004) – C(137) × C(137). Additional path length acquired by the X-rays in the monochromator is $\delta L = 3.0H$. Alternative realization is C(004) × C(004) – Si(139) × Si(139) with silicon crystals as a high-energy resolution monochromator. The additional path length is $\delta L = 1.7H$.

the X-ray pulse acquires in the monochromator. The path delay equals to

$$\delta L = H\,(\tan\theta_{HKL} + \tan\theta_{hkl}), \qquad (5)$$

where H is the beam shift, θ_{HKL} in the Bragg angle of the reflections in the high heat-load part (the first two crystals), and θ_{hkl} in the Bragg angle of the reflections in the high energy-resolution part of the monochromator (the third and the forth crystals). By varying H one can keep the delay δL constant in the whole tunability range of the monochromator. For the proposed monochromator schemes the actual values of δL are given in Fig. 2 caption and can be about 1 cm.

4. Conclusion

Our analysis shows that the construction of the high-brilliant two-stage SASE FEL in the Angström spectral range is feasible. We have considered an ultimate case when the spectral bandwidth is defined by the finite duration of the electron bunch (lower limit in (2)). By increasing the bahdwidth one can increase the tunability range and reduce the power density incident on crystals. The final choice of parameters will be dictated by needs of potential users of intense monochromatic X-rays.

Acknowledgements

We thank G. Materlik, J. Pflüger and J. Rossbach for their interest in this work. We are grateful to J. Feldhaus and J.R. Schneider for many useful discussions on the two-stage SASE FEL.

References

[1] J. Feldhaus et al., Opt. Commun. **140**(1997)341.

[2] Ya.S. Derbenev, A.M. Kondratenko, and E.L. Saldin, Nucl. Instrum. and Methods **193**(1982)415.

[3] J.B. Murphy and C. Pellegrini, Nucl. Instrum. and Methods **A237**(1985)159.

[4] J. Rossbach, Nucl. Instrum. and Methods **A375**(1996)269.

[5] E.L. Saldin, E.A. Schneidmiller, and M.V. Yurkov, Nucl. Instrum. and Methods **A375**(1996)269.

[6] "Conceptual Design of a 500 GeV e+e− Linear Collider with Integrated X-ray Laser Facility" (Editors R.Brinkmann, G. Materlik, J. Rossbach, A. Wagner), DESY 97-048, Hamburg, 1997.

[7] *Nuclear Resonant Scattering of Synchrotron Radiation*, edited by E. Gerdau and H. de Waard, Hyperfine Interactions **123/124** (1999) and **125** (2000).

[8] E.L. Saldin, E.A. Schneidmiller, and M.V. Yurkov, Nucl. Instrum. and Methods **A429**(1999)233.

[9] E.L. Saldin, E.A. Schneidmiller, and M.V. Yurkov, Nucl. Instrum. and Methods **A374**(1996)401.

[10] E.L. Saldin, E.A. Schneidmiller, and M.V. Yurkov, Nucl. Instrum. and Methods **A381**(1996)545.

[11] E.L. Saldin, E.A. Schneidmiller, and M.V. Yurkov, *The Physics of Free Electron Lasers*, Springer, Berlin, 1999.

[12] T. Toellner, Hyperfine Interactions **125** (2000) 3.

[13] Z.G. Pinsker, *Dynamical Scattering of X rays in Crystals*, Springer, Berlin, 1978.

[14] T. Ishikawa, Private communication.

[15] D.H. Bilderback et al., J. Synchrotron Rad. **7**(2000)53

Diffraction Effects in the SASE FEL: Numerical Simulation and Theory

E.L. Saldin [a], E.A. Schneidmiller [a], M.V. Yurkov [b]

[a] *Deutches Elektronen Synchrotron (DESY), 22607 Hamburg, Germany*

[b] *Joint Institute for Nuclear Research, Dubna, 141980 Moscow Region, Russia*

Abstract

In this paper we present a systematic approach for analytical description of SASE FEL in the linear mode. We calculate the average radiation power, radiation spectrum envelope, angular distribution of the radiation intensity in far zone, degree of transverse coherence etc. Using the results of analytical calculations presented in reduced form, we analyze various features of the SASE FEL in the linear mode. The general result is applied to the special case of an electron beam having Gaussian profile and Gaussian energy distribution. These analytical results can be serve as a primary standard for testing the codes. In this paper we present numerical study of the process of amplification in the SASE FEL using three-dimension time-dependent code FAST. Comparison with analytical results shows that in the high-gain linear limit there is good agreement between the numerical and analytical results. It has been found that even after finishing the transverse mode selection process the degree of transverse coherence of the radiation from SASE FEL visibly differs from unity. This is consequence of the interdependence of the longitudinal and transverse coherence. The SASE FEL has poor longitudinal coherence which develops slowly with the undulator length thus preventing a full transverse coherence.

1. Introduction

A complete description of the SASE FEL can be performed only with three-dimensional (3-D) time-dependent numerical simulation codes. Application of the numerical calculations allows one to describe the general case of the SASE FEL operation, including the case of an arbitrary axial and transverse profile of the electron bunch, the effects of finite pulse duration and nonlinear effects. Since construction of the 3-D time-dependent codes is a rather complicated problem, significant attention should be devoted to the testing the codes. On the other hand, testing the numerical simulation codes would be difficult without the use of analytical results of SASE FEL linear theory as a primary standard.

With the design and construction of VUV and X-ray FELs, many 3-D time-dependent codes (GINGER [1], GENESIS [2], FAST [3]) have been developed over the years in order to describe FEL amplifier start-up from shot noise. Nevertheless, it should be emphasized that despite these codes are widely used in the design of X-ray FELs [4–7], there are no comparison between numerical simulation and analytical results of 3-D SASE FEL theory.

From the theoretical point of view the SASE FEL, is a rather complicated object, so it is important to find a model which provides the possibility of an analytical description without loss of essential information about the features of the SASE process. When deriving analytical results we used the model of a long electron bunch with rectangular axial profile of the current. Investigation of the SASE FEL process is preformed with steady-state spectral Green's function connecting the Fourier amplitudes of the output field and the Fourier amplitudes of the input noise signal. Since in the linear regime all the harmonics are amplified independently, we can use the result of steady-state theory for each harmonic and calculate the corresponding Fourier harmonics of output radiation field. In the framework of this model it becomes possible to describe analytically all the statistical properties of the radiation from the SASE FEL.

When the FEL amplifier operates in the steady-state linear regime, the driving electron beam can be considered as an active medium whose properties do not depend on the longitudinal coordinate z. Let us analyze the nature of the self-consistent solution of Maxwell's equations and the Vlasov equation at a fixed frequency ω. The electric field of the wave radiated in the helical undulator may be represented in the complex form:

$$E_x + \mathrm{i}\, E_y = \tilde{E}(z, \vec{r}_\perp) \exp[\mathrm{i}\, \omega(z/c - t)] \ , \qquad (1)$$

At a sufficient distance from the undulator entrance the radiation can be presented as a superposition of the exponentially growing guided modes

$$\tilde{E}(z, \vec{r}_\perp) = \sum_j A_j \Phi_j(\vec{r}_\perp) \exp(\lambda_j z) \ ,$$

where λ_j and $\Phi_j(\vec{r}_\perp)$ are the eigenvalues and the eigenfunctions of the guiding modes, respectively, and $\mathrm{Re}(\lambda_j) > 0$. The rigorous solution of the eigenvalue problem for an axisymmetric electron beam with stepped profile was obtain in [8]. The model of the FEL amplifier considered in that paper is based on a full three-dimensional description of electromagnetic field, but the electron motion is considered to be one-dimensional. Later the initial-value problem was solved in [9] in framework of the same model of the electron beam. An effects similar to the optical guiding effects occurs in optical fibers. However, unlike guided modes in fiber optics, FEL guided modes are not orthogonal. To solve the initial value problem in the case of arbitrary gradient beam profile, approaches other than direct mode expansion must be used. The first step in this direction was taken by Kim [10], who has applied a method of solution, originally introduced by van Kampen [11]. A Laplace transform method was employed by Krinsky and Yu [12], leading to a Green's function. This Green's function can still be expanded in terms of orthonormal eigenfunctions of the associated two-dimension Schrödinger equation with non-self-adjoint Hamiltonian. In the high-gain limit, the asymptotic representation of the Green's function is found to be dominated by the contribution of the guided modes. The eigenvalue problem for the case of an arbitrary gradient axisymmetric profile is solved by means of the multilayer approximation method [13]. Based on these solutions, complete information on the eigenfunctions and eigenvalues can be extracted, and used, for calculations of the output radiation field. General solution for Green's function [12] gives us input coupling factors A_j.

In this paper we present a systematic approach for calculations of the average radiation power, radiation spectrum envelope, and angular distribution of the radiation intensity in the far zone, and degree of transverse coherence. These analytical results serve as a primary standard for testing the codes. Numerical simulations have been performed with 3-D time-dependent code FAST [3]. Comparison with analytical results shows that in the high-gain linear limit there is a good agreement between the numerical and analytical results.

2. Analytical Description of the Steady-State Linear Regime

Let us consider electron beam moving along the z axis in the field of a helical undulator. The magnetic field of the undulator may be written in the complex form: $H_x = H_\mathrm{w} \cos(k_\mathrm{w} z)$, $H_y = -H_\mathrm{w} \sin(k_\mathrm{w} z)$. We neglect the transverse variation of the undulator field and assume the electrons move along constrained helical trajectories in parallel with the z axis. The electron rotation angle is considered to be small and the longitudinal electron velocity v_z is close to the velocity of light c. Let us consider a axisymmetric electron beam with gradient profile of the current density. The general form of the transverse distribution of the beam current density of axisymmetric electron beam (in cylindrical coordinates (r, φ, z)) is

$$j_0(r) = I_0 S(r/r_0) \left[2\pi \int\limits_0^\infty r S(r/r_0) \,\mathrm{d}\, r \right]^{-1} , \qquad (2)$$

where r_0 is the beam profile parameter (typical transverse size of the beam) and I_0 is the beam current. To be specific, we set $S(0) = 1$.

We describe the electron motion using energy-phase variables $P = \mathcal{E} - \mathcal{E}_0$ and $\psi = k_\mathrm{w} z + \omega(z/c - t)$, where $\mathcal{E}$ is the kinetic energy of the electron, $\mathcal{E}_0$ is the nominal energy. The evolution of the distribution function of the electron beam is governed by the Vlasov equation. We solve this equation using the perturbation method, so the beam current density is given by:

$$j_z = -j_0(r) + \sum_{n=-\infty}^{n=+\infty} \tilde{j}_1^{(n)}(z,r) \mathrm{e}^{-\mathrm{i}\, n\varphi + \mathrm{i}\,\psi} + \mathrm{C.C.} \ ,$$

At a sufficient distance from the undulator entrance the output radiation can be presented as a superposition of the "self-reproducing" field configurations. It is reasonable to represent $\tilde{E}$ as a Fourier series in the angle φ:

$$\tilde{E}(z,r,\varphi) = \sum_{n=-\infty}^{n=+\infty} \tilde{E}^{(n)}(z,r) \mathrm{e}^{-\mathrm{i}\, n\varphi} \ ,$$

and write $\tilde{E}^{(n)}$ in dimensionless form

$$\hat{E}^{(n)}(\hat{z},\hat{r}) = \sum_j A_j^{(n)} \Phi_{nj}(\hat{r}) \exp(\lambda_j^{(n)} \hat{z}) \ . \qquad (3)$$

In this paper we consider the specific, but important practical case of the following initial conditions: - the electron beam is modulated only in density at the undulator entrance; - the field amplitude of the electromagnetic wave $\tilde{E}$ takes the value $\tilde{E}|_{z=0} = 0$ at the undulator entrance. The input coupling factors $A_j^{(n)}$ are given by the expression [10,12]:

$$A_j^{(n)} = 2u_j^{(n)} \int\limits_0^\infty \hat{a}_{\mathrm{ext}}^{(n)}(\hat{r}) S(\hat{r}) \Phi_{nj}(\hat{r}) \hat{r} \,\mathrm{d}\,\hat{r} \ ,$$

where $u_j^{(n)}$ can be written in the following form:

$$u_j^{(n)} = \hat{D}_0(\lambda_j^{(n)}) \left[B \int\limits_0^\infty \Phi_{nj}^2(\hat{r}) \hat{r} \,\mathrm{d}\,\hat{r} - \left(\frac{\mathrm{d}\,\hat{D}}{\mathrm{d}\,p} \right)_{p=\lambda_j^{(n)}} \int\limits_0^\infty \Phi_{nj}^2(\hat{r}) S(\hat{r}) \hat{r} \,\mathrm{d}\,\hat{r} \right]^{-1} \ .$$

Here the following notation is introduced: $C = k_{\mathrm{w}} - \omega/(2c\gamma_z^2)$ is the detuning of the electron with the nominal energy $\mathcal{E}_0$,

$$\theta_{\mathrm{s}} = eH_{\mathrm{w}}/(\mathcal{E}_0 k_{\mathrm{w}}) = K/\gamma \ , \quad \gamma_z^{-2} = \gamma^{-2} + \theta_{\mathrm{s}}^2, \quad \gamma = \mathcal{E}_0/(m_{\mathrm{e}} c^2) \ ,$$

$\hat{z} = \Gamma z$, $\hat{r} = r/r_0$, $\hat{C} = C/\Gamma$ is the detuning parameter, $B = r_0^2 \Gamma \omega / c$,

$$\Gamma = \left[I_0 \omega^2 \theta_{\mathrm{s}}^2 \left(2 I_{\mathrm{A}} c^2 \gamma_z^2 \gamma \int\limits_0^\infty \zeta S(\zeta) \,\mathrm{d}\,\zeta \right)^{-1} \right]^{1/2}$$

$I_{\mathrm{A}} \simeq 17$ kA is the Alfven current. The complex amplitudes $\tilde{E}^{(n)}$ and $\hat{E}^{(n)}$ are connected by the relation $\hat{E}^{(n)} = \tilde{E}^{(n)}/E_0$, $\quad E_0 = \rho\mathcal{E}_0\Gamma/(e\theta_{\mathrm{s}})$, $\quad \rho = c\gamma_z^2\Gamma/\omega$. The complex amplitude of the first harmonic of the beam current density $\tilde{j}_1^{(n)}$ is connected with $\hat{a}_1^{(n)}$ by the relation

$$\hat{a}_1^{(n)}(\hat{z},\hat{r}) = -\tilde{j}_1^{(n)}(\hat{z},\hat{r})/j_0(\hat{r}) \ , \quad \hat{a}_{\mathrm{ext}}^{(n)}(\hat{r}) = \hat{a}_1^{(n)}(\hat{z},\hat{r})|_{z=0} \ .$$

For a Gaussian energy spread in the electron beam

$$F(\mathcal{E}-\mathcal{E}_0) = (2\pi\langle(\Delta\mathcal{E})^2\rangle)^{-1/2}\exp\left(-\frac{(\mathcal{E}-\mathcal{E}_0)^2}{2\langle(\Delta\mathcal{E})^2\rangle}\right) \ ,$$

the functions $\hat{D}(p)$ and $\hat{D}_0(p)$ are given by

$$\begin{pmatrix}\hat{D}\\ \hat{D}_0\end{pmatrix} = \int\limits_0^\infty \begin{pmatrix}\mathrm{i}\,\xi\\ 1\end{pmatrix}\exp\left[-\hat{\Lambda}_{\mathrm{T}}^2\xi^2/2-(p+\mathrm{i}\,\hat{C})\xi\right]\mathrm{d}\,\xi \ ,$$

where $\hat{\Lambda}_{\mathrm{T}}^2 = \langle(\Delta\mathcal{E})^2\rangle/(\rho^2\mathcal{E}_0^2)$.

An important characteristic of the FEL amplifier is the output power. In the paraxial approximation the power of the radiation with azimuthal index n, can be written in the following normalized form:

$$\hat{W}^{(n)} = \frac{W^{(n)}}{\rho W_{\mathrm{b}}} = \frac{c}{2\rho W_{\mathrm{b}}}\int\limits_0^\infty|\tilde{E}^{(n)}|^2 r\,\mathrm{d}\,r = \frac{B}{4}\int\limits_0^\infty|\hat{E}^{(n)}(\hat{z},\hat{r})|^2\hat{r}\,\mathrm{d}\,\hat{r}\left[\int\limits_0^\infty\zeta S(\zeta)\,\mathrm{d}\,\zeta\right]^{-1} \ , \quad (4)$$

where $W_{\mathrm{b}} = \mathcal{E}_0 I_0/e$ is the electron beam power. Thus, the exact solution of the initial-value problem for FEL amplifier with arbitrary gradient profile has been derived. As a result, if we have information on the eigenfunctions and eigenvalues, we are able to calculate radiation properties of the FEL amplifier which operates in high gain linear regime. The eigenvalue problem for the case of an arbitrary gradient axisymmetric profile is solved by means of the multilayer approximation method (see [13,14] for more details).

3. Start-up from Shot Noise

We start with the calculation of the average radiation power at the undulator exit. Under the accepted limitations we obtain that the contribution of the radiation with azimuthal index n to the total radiation power can be written in the following form [10,12]:

$$\langle\hat{W}^{(n)}\rangle = \frac{B}{\pi N_{\mathrm{c}}}\int\limits_{-\infty}^{\infty}\mathrm{d}\,\hat{C}\left\{\sum_{k,j}u_k^{(n)}(u_j^{(n)})^*\exp\left\{[\lambda_k^{(n)}+(\lambda_j^{(n)})^*]\hat{z}\right\}\right.$$

$$\times \int_0^\infty \Phi_{nk}(\hat r)\Phi^*_{nj}(\hat r)S(\hat r)\hat r \,\mathrm{d}\,\hat r \int_0^\infty \Phi_{nk}(\hat r)\Phi^*_{nj}(\hat r)\hat r \,\mathrm{d}\,\hat r \Bigg\} \ , \tag{5}$$

where $N_\mathrm{c} = N_\lambda/(2\pi\rho)$, $N_\lambda = 2\pi I_0/(e\omega_0)$. The averaging symbol $\langle\cdots\rangle$ means the ensemble average over bunches.

At a sufficiently large undulator length the spectrum of the SASE radiation is concentrated within the narrow band near the resonance frequency ω_0. Therefore, the electric field of the wave can be presented as

$$E_x + \mathrm{i}\, E_y = \tilde E(\vec r_\perp, z, t)\, \mathrm{e}^{\mathrm{i}\,\omega_0(z/c-t)} + \mathrm{C.C.} \ ,$$

where $\tilde E$ is the slowly varying complex amplitude. Taking into account Parseval's theorem, and using the notation $\vec\rho = \vec r_\perp - \vec r\,'_\perp$ and $\vec R = (\vec r_\perp + \vec r\,'_\perp)/2$, we can write the average angular spectrum in the form:

$$h(\vec k_\perp, z) = \frac{1}{(2\pi)^2}\int \gamma^{\mathrm{eff}}(\vec\rho, z)\exp(-\,\mathrm{i}\,\vec k_\perp \vec\rho)\,\mathrm{d}\,\vec\rho \ ,$$

where we introduce the definition of effective transverse correlation function:

$$\gamma^{\mathrm{eff}}(\vec\rho, z) = \frac{\int\langle \tilde E(\vec R + \vec\rho/2, z, t)\tilde E^*(\vec R - \vec\rho/2, z, t)\rangle\,\mathrm{d}\,\vec R}{\int\langle|\tilde E(\vec R, z, t)|^2\rangle\,\mathrm{d}\,\vec R} \ .$$

Let us consider a axisymmetric electron beam. Using cylindrical coordinates we represent output power as a Fourier series in the azimuthal angle. In this case the angular spectrum can be written in the following dimensionless form:

$$h(\hat\theta, \hat z) = \left[\sum_{n,k,j}\int_{-\infty}^{\infty}\mathrm{d}\,\hat C\left(\Omega^{(n)}_{kj}\int_0^\infty \Phi_{nk}(\hat r)J_n(\hat\theta\hat r)\hat r\,\mathrm{d}\,\hat r\int_0^\infty \Phi^*_{nj}(\hat r')J_n(\hat\theta\hat r')\hat r'\,\mathrm{d}\,\hat r'\right)\right]$$
$$\times\left[2\pi\sum_{n,k,j}\int_{-\infty}^{\infty}\mathrm{d}\,\hat C\left(\Omega^{(n)}_{kj}\int_0^\infty \Phi_{nk}(\hat r)\Phi^*_{nj}(\hat r)\hat r\,\mathrm{d}\,\hat r\right)\right]^{-1} \ . \tag{6}$$

To simplify this expression, we use the following notations: $\hat\theta = \theta\omega_0 r_0/c$,

$$\Omega^{(n)}_{kj} = u^{(n)}_k (u^{(n)}_j)^* \exp\left\{[\lambda^{(n)}_k + (\lambda^{(n)}_j)^*]\hat z\right\}\int_0^\infty \Phi_{nk}(\hat r)\Phi^*_{nj}(\hat r)S(\hat r)\hat r\,\mathrm{d}\,\hat r \ .$$

4. Comparison of analytical and simulation results

One can easily obtain that identical physical approximations have been used for analytical description of the high-gain linear regime and for numerical simulation algorithm.

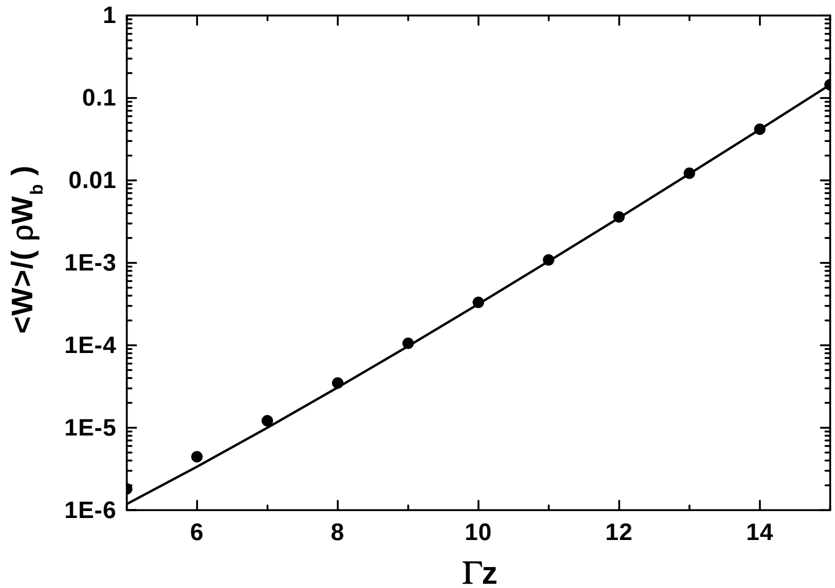

Fig. 1. Averaged power versus undulator length for the FEL amplifier starting from shot noise. Here $B = 1$, $\Lambda_{\mathrm{p}}^2 \to 0$, $\Lambda_{\mathrm{T}}^2 = 0$, and $N_{\mathrm{c}} = 7 \times 10^7$. Solid curve represents analytical results calculated with (5) for nine beam radiation modes ($m, n = 0, 1, 2$). The circles are the results obtained with linear simulation code FAST

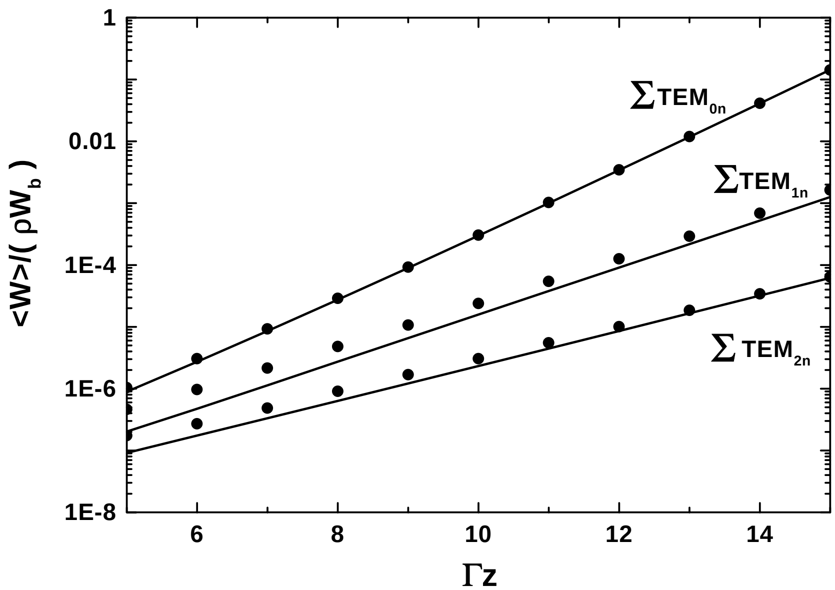

Fig. 2. Partial contributions to the total power (see 1) of three azimuthal modes with $m = 0, 1$, and 2. Here $B = 1$, $\Lambda_{\mathrm{p}}^2 \to 0$, $\Lambda_{\mathrm{T}}^2 = 0$, and $N_{\mathrm{c}} = 7 \times 10^7$. Solid curves represent analytical results calculated with (5) for sum of three radial modes ($n = 0, 1, 2$). The circles are the results obtained with linear simulation code FAST

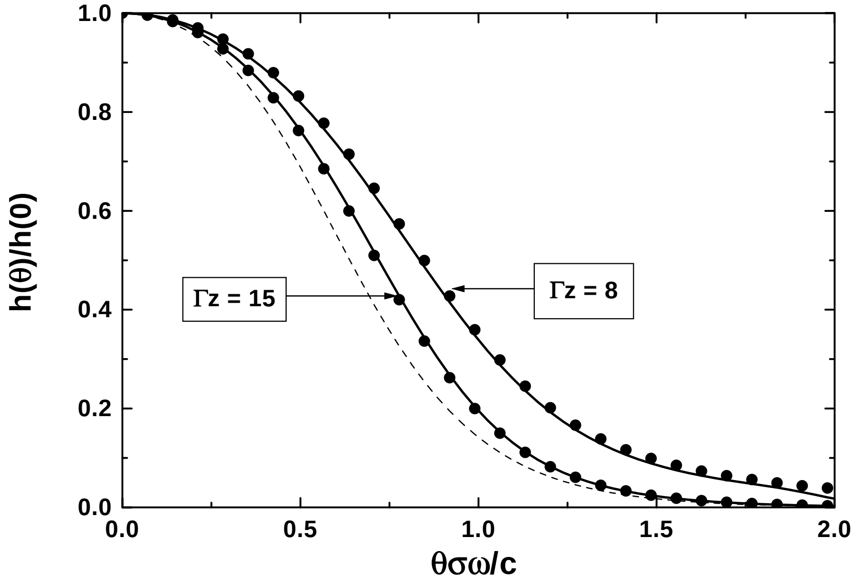

Fig. 3. Averaged angular distribution of the radiation intensity in the far zone for the FEL amplifier starting from shot noise. Here $B = 1$, $\Lambda_{\mathrm{p}}^2 \to 0$, and $\Lambda_{\mathrm{T}}^2 = 0$. Solid curves are the results of analytical calculations with (6), and the circles are the results obtained with linear simulation code FAST. Dashed line represents angular distribution of the fundamental TEM_{00} mode for maximum growth rate calculated in the framework of the steady-state theory

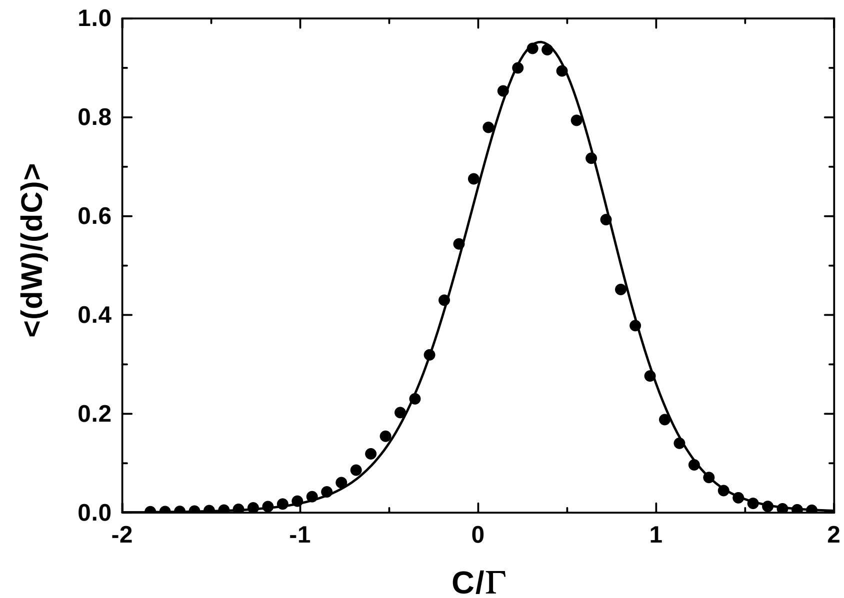

Fig. 4. Averaged spectrum of the radiation from the FEL amplifier starting from shot noise at the undulator length $\hat{z} = 15$. Here $B = 1$, $\Lambda_{\mathrm{p}}^2 \to 0$, $\Lambda_{\mathrm{T}}^2 = 0$, and $N_{\mathrm{c}} = 7 \times 10^7$. Solid curve represents analytical results calculated with (5) for nine beam radiation modes ($m, n = 0, 1, 2$). The circles are the results obtained with linear simulation code FAST

So, we should expect full agreement of the results in the high-gain linear regime. In other words, analytical results should serve as a primary standard for testing numerical simulation code. Figure 1 shows the evolution of the total radiation power from SASE FEL versus the undulator length. Simulation results have been obtained by means of averaging of the radiation power along the bunch. It is seen that analytical and simulation results agree well at $\hat{z} \gtrsim 7$. Another interesting topic is partial contribution of different beam radiation modes into the total radiation power (see Fig 2). It is seen that both numerical and analytical results agree well at an increase of the undulator length. One can obtain that numerical simulations always give the value of the radiation power higher than analytical results. The reason is that the numerical simulation code calculates total gain, while the analytical formulae describe only the high-gain asymptote.

Analytical predictions for the averaged angular distribution of the radiation power are given by (6). Similar characteristic can be also calculated with numerical simulation code. Numerical simulation code produces an array containing values for the radiation field in the near zone. Using the values for the radiation field in the near zone, we find the radiation field propagating at any angle in the far diffraction zone. It is seen from Fig. 3 that both approaches agree well in the high-gain linear regime. It is important to stress that even after finishing the transverse mode selection process (which takes place after $\hat{z} \gtrsim 10$ for the considered numerical example) the distribution in the far zone differs visibly from the angular distribution of the fundamental TEM_{00} mode for maximum growth rate calculated in the framework of the steady-state theory (dotted line in Fig. 3). Analytical results give predictions for the averaged radiation spectrum (see (5)). To obtain averaged spectrum from numerical simulation code, we performed large number of statistically independent simulation runs. Average of a large number of radiation spectra is presented in Fig. 4. It is seen that the analytical and simulation results for the averaged radiation spectrum agree well in the high-gain linear regime.

5. Transverse coherence

In the case of axisymmetric electron beam the radiation field statistically isotropic. For such a field the effective correlation function depends only on the modulus $|\vec{\rho}|$ and the angular spectrum depends on the modulus $|\vec{k}_\perp|$. It is natural to define the area of coherence in this case as:

$$\pi \hat{r}^2_{\mathrm{coh}} = 2\pi \int\limits_0^\infty |\gamma_1^{\mathrm{eff}}(\hat{\rho},\hat{z})|^2 \hat{\rho} \, \mathrm{d}\,\hat{\rho} \ , \quad \gamma_1^{\mathrm{eff}}(\hat{\rho},\hat{z}) = 2\pi \int\limits_0^\infty J_0(\hat{\rho}\hat{\theta}) h(\hat{\theta}) \hat{\theta} \, \mathrm{d}\,\hat{\theta} \ , \tag{7}$$

where $\hat{\rho} = |\vec{\rho}|/r_0$. To describe the formation of the transverse coherence, we should define the degree of coherence. One possible definition can be made as follows. After statistical analysis of the numerical results we find $\hat{r}_{\mathrm{coh}}$. Then we find the radius of coherence $\hat{r}_{\max}$ for the fully coherent radiation which is represented by the fundamental $\Phi_{00}(\hat{r})$ mode for maximum growth rate. The field distribution of this mode for Gaussian density distribu-

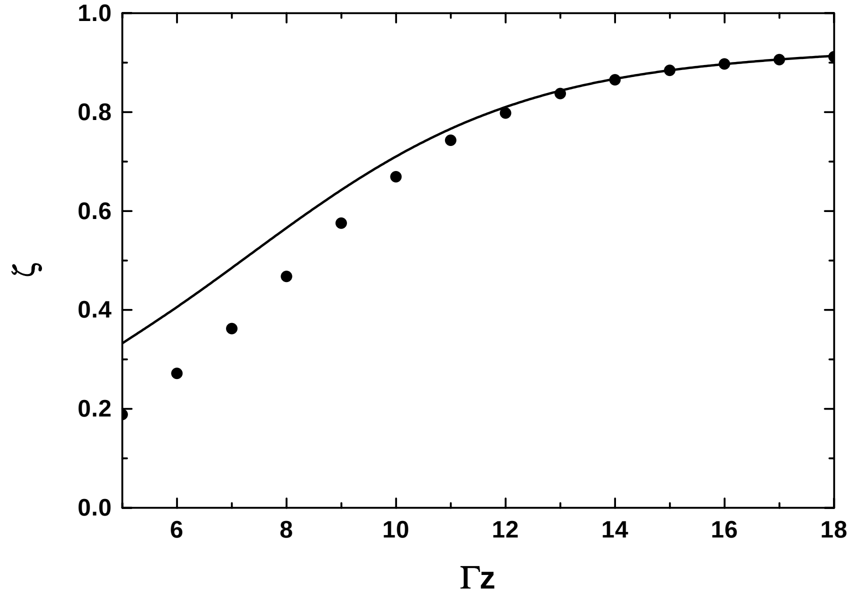

Fig. 5. Degree of transverse coherence of the radiation from the FEL amplifier versus the undulator length. Solid curve represents analytical results, and the circles are the results obtained with linear simulation code FAST. Here $B = 1$, $\Lambda_{\mathrm{p}}^2 \to 0$, $\Lambda_{\mathrm{T}}^2 = 0$, and $N_{\mathrm{c}} = 7 \times 10^7$

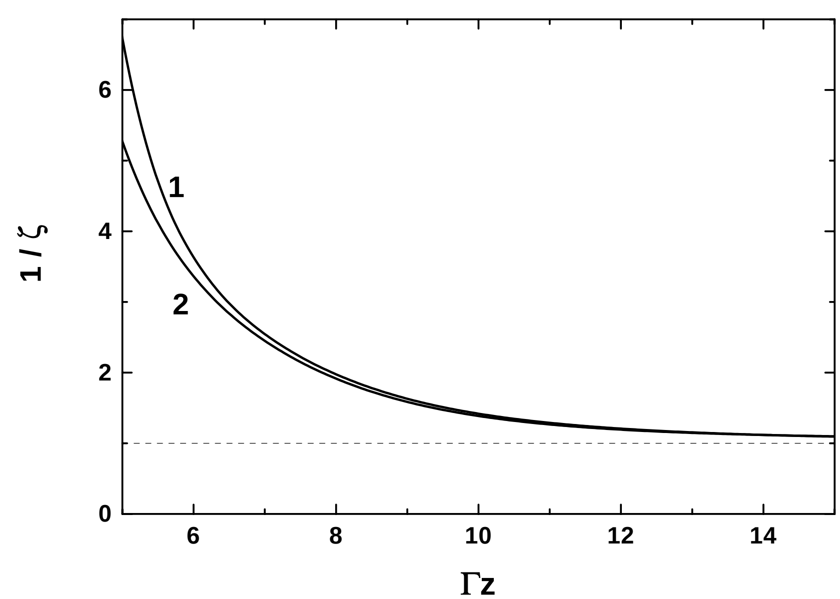

Fig. 6. Inverse value of transverse coherence versus undulator length. Here $B = 1$, $\Lambda_{\mathrm{p}}^2 \to 0$, $\Lambda_{\mathrm{T}}^2 = 0$, and $N_{\mathrm{c}} = 7 \times 10^7$. Calculations have been performed with linear simulation code FAST. Curve 1 is calculated using instantaneous fluctuations of the radiation power. Curve 2 is calculated using angular distribution of the radiation power in far zone.

tion in the electron beam can be found by the multilayer approximation method described in section 2.2. The degree of coherence, ζ, may be defined as $\zeta = \hat{r}^2_{\mathrm{coh}}/\hat{r}^2_{\mathrm{max}}$. Using angular distributions of the radiation field in the far diffraction zone we can trace the dependence of the degree of transverse coherence versus undulator length. Solid line in Fig. 5 is the results of analytical calculations, and the circles are the results obtained with numerical simulation code. We can state that there is good agreement between analytical and simulation results. It is clearly seen that the degree of coherence differs visibly from the unity in the high-gain linear regime, $\zeta \simeq 0.9$ at $\hat{z} = 15$.

Another possible way to define the degree of coherence is based on the statistical analysis of fluctuations of the instantaneous power. Since in the linear regime we deal with a Gaussian random process, the power density at fixed point in space fluctuates in accordance with the negative exponential distribution [14]. If there is full transverse coherence then the same refers to the instantaneous power W equal to the power density integrated over cross section of the radiation pulse. If the radiation is partially coherent, then we have a more general law for instantaneous power fluctuations, namely the gamma distribution [14,15]:

$$p(W) = \frac{M^M}{\Gamma(M)} \left(\frac{W}{\langle W \rangle} \right)^{M-1} \frac{1}{\langle W \rangle} \exp \left(-M \frac{W}{\langle W \rangle} \right) \ , \tag{8}$$

where $\Gamma(M)$ is the gamma function and $M = \langle W \rangle^2 / \langle (W - \langle W \rangle)^2 \rangle$. The parameter M of this distribution can be considered as the number of transverse modes. Then the degree of coherence in the linear regime, may be defined as follows $\zeta = 1/M$. The value of M should be calculated with numerical simulation code producing time-dependent results for the radiation power. In Fig. 6 we present the dependence of the number of transverse modes on the undulator length for the specific value $B = 1$ of the diffraction parameter. It is seen that both definitions for the degree for the transverse coherence are consistent in the high-gain linear regime.

Let us discuss asymptotical behaviour of the degree of transverse coherence. At a large value of the undulator length it approaches to unity asymptotically as $(1 - \zeta) \propto 1/z$, but not exponentially, as one can expect from simple physical assumption that transverse coherence establishes due to the transverse mode selection. That is why the degree of coherence grows quickly at an early stage of amplification. Starting from some undulator length the contribution to the total power of the fundamental mode becomes to be dominant (see Fig. 2). However, one should take into account that the spectrum width has always finite value (see Fig. 4). Actually this means that in the high gain linear regime the radiation of the SASE FEL is formed by many fundamental TEM_{00} modes with different frequencies. The transverse distribution of the radiation field of the mode is also different for different frequencies. As a result of interference of these modes we do not have full transverse coherence. Taking into account this consideration, we can simply explain asymptotical behaviour of the degree of transverse coherence – this is reflection of the slow evolution of the width of the radiation spectrum as $z^{-1/2}$ with the undulator length.

All the results presented above have been obtained in the framework of the linear theory. Simulations with nonlinear code shows that for the considered numerical example the saturation occurs at $\hat{z} \simeq 18$. Using the plot presented in Fig. 5 we find that the value of the transverse coherence is less than 0.9 in the end of the linear regime. A typical range of the values of N_c is 10^6-10^9 for the SASE FEL of wavelength range from X-ray up to infrared. The numerical example presented in this paper is calculated for $N_c = 7 \times 10^7$ which is typical for a VUV FEL. It is worth to mention that the dependence of the saturation length of the SASE FEL on the value of N_c is rather weak, in fact logarithmic (see (5)). Therefore, we can state that obtained effect limiting the value of transverse coherence might be important for practical SASE FELs.

References

[1] W.M. Fawley, An Informal Manual for GINGER and its post-processor XPLOTGIN", LBID-2141,CBT Tech Note-104, UC-414(1995).

[2] S. Reiche, Nucl. Instrum. and Methods A 429(1999)243

[3] E. L. Saldin, E. A. Schneidmiller, and M. V. Yurkov, Nucl. Instrum. and Methods A 429(1999)233

[4] "A VUV Free Electron Laser at the TESLA Test Facility: Conceptual Design Report", DESY Print TESLA-FEL 95-03, Hamburg, DESY, 1995

[5] J. Rossbach, Nucl. Instrum. and Methods A **375**(1996)269

[6] R. Brinkmann et al. (Eds), "Conceptual Design of 500 GeV e^+e^- Linear Collider with Integrated X-ray Facility", DESY 1997-048, ECFA 1997-182, Hamburg, May 1997

[7] "Linac Coherent Light Sorce (LCLS) Design Study Report", The LCLS Design Study Group, Stanford Linear Accelerator Center (SLAC) Report No. SLAC-R-521, 1998

[8] G.T. Moore, Opt. Commun. 52(1984)46

[9] G.T. Moore, Nucl. Instrum. and Methods A 250(1986)381

[10] K.J. Kim, Phys. Rev. Lett. 57(1986)1871

[11] N.G. van Kampen, Physica 21(1951)949

[12] S. Krinsky and L.H. Yu, Phys. Rev. A 35(1987)3406

[13] E. L. Saldin, E. A. Schneidmiller, and M. V. Yurkov, Opt. Commun. 97(1993)272

[14] E. L. Saldin, E. A. Schneidmiller, and M. V. Yurkov, "The Physics of Free Electron Laser" Springer-Verlag Berlin Heidelberg New York 1999

[15] E. L. Saldin, E. A. Schneidmiller, and M. V. Yurkov, Nucl. Instrum. and Methods **A429**(1999)229

The General Solution of the Eigenvalue Problem for a High-Gain FEL

E.L. Saldin [a], E.A. Schneidmiller [a], M.V. Yurkov [b]

[a] *Deutsches Elektronen-Synchrotron, Notkestrasse 85, 22607 Hamburg, Germany*

[b] *Joint Institute for Nuclear Research, Dubna, 141980 Moscow Region, Russia*

Abstract

The exact solution of the eigenvalue equation for a high-gain FEL derived in [1] is generalized in order to include the space charge effects. This solution is valid not only for weak focusing (natural undulator focusing) but also for alternating-gradient focusing under some condition that is presented. At such, the obtained solution includes all the important effects in the system of axially homogeneous electron beam and undulator: diffraction, betatron motion, energy spread, space charge and frequency detuning. It is valid for ground TEM_{00} mode as well as for high-order modes and can be used for calculation of high-gain FEL amplifiers operating in the wavelength regions from far infrared down to X-ray. In addition, a computationally efficient approximate solution for TEM_{00} mode is derived providing high accuracy (better than 1% in the whole range of parameters). It can be used for quick optimization of FEL amplifiers.

1. Introduction

The solution of an eigenvalue problem is the first and very important step in the design and optimization of a high-gain FEL. The first solution of the eigenvalue problem was obtained in [2] in the frame of one-dimensional model taking into account space charge, energy spread, and frequency detuning. Diffraction effects for a parallel electron beam (no betatron oscillations) were considered in [3] and [4] neglecting space charge and energy spread. In [3] the asymptotical solutions for weak and strong diffraction regimes were obtained, and in [4] the exact solution was derived for the first time for a stepped transverse profile of the axisymmetric electron beam. In the proceeding papers [5,6] the eigenvalue problem for the model of parallel electron beam, including diffraction of radiation, was studied extensively in order to include different transverse profiles of the electron beam, high-order modes of the radiation, energy spread and space charge effects.

A more difficult task was the eigenvalue problem that includes diffraction of radiation and a transverse motion of electrons (betatron oscillations). The integro-differential equation, taking into account both these effects as well as frequency detuning and energy spread, was derived in [7,8]. Different methods to find an approximate solution of the eigenvalue problem were used in [1,9–11] for different phase space distributions of the electron beam. The exact solution (in a sense that it can be evaluated numerically with any desirable accuracy) for all the eigenmodes was obtained in [1].

In this paper we generalize the exact solution derived in [1] in order to include the space charge effect. Although this effect is negligible in X-ray wavelength range [12–14], it can be important for infrared [15–17], visible and ultraviolet [18,19] high-gain FELs. Thus, our solution is a universal tool for calculation and optimization of high-gain FELs. Indeed, it includes all the important effects in a system of axially homogeneous electron beam and undulator: diffraction, betatron motion, energy spread, space charge and frequency detuning. [1] In addition, we derive here an approximate solution for the ground TEM_{00} mode. The numerical algorithm for finding this solution is very fast and accurate, so it can be used for quick optimization of high-gain FELs.

It is worth noticing that the authors of [1,8–11] assumed natural undulator focusing. Actually, the validity region of the obtained results (including the results of this paper) is wider: they can also be used in the case of an alternating-gradient external focusing. In this case the following condition should be satisfied [20]:

$$\frac{L_f}{2\pi\beta} \ll \min\left(1, \frac{\lambda}{2\pi\epsilon}\right) \ ,$$

where L_f is a period of the external focusing structure, β is an average beta-function, ϵ is rms emittance of an electron beam, and λ is a radiation wavelength. This condition is met in many practical situations.

2. Basic equation

Let us have at the undulator entrance a continuous electron beam with the current I_0, with the Gaussian distribution in energy

$$F(\mathcal{E}-\mathcal{E}_0) = \left(2\pi\langle(\Delta\mathcal{E})^2\rangle\right)^{-1/2} \exp\left(-\frac{(\mathcal{E}-\mathcal{E}_0)^2}{2\langle(\Delta\mathcal{E})^2\rangle}\right) \ , \qquad (1)$$

[1] We do not touch here the eigenvalue problem for a waveguide FEL where an additional parameter appears [21].

and in a transverse phase plane

$$f(x, x') = (2\pi\sigma^2 k_\beta)^{-1} \exp\left[-\frac{x^2 + (x')^2/k_\beta^2}{2\sigma^2}\right] \ , \tag{2}$$

the same in y phase plane. Here $k_\beta = 1/\beta$ is the wavenumber of betatron oscillations and $\sigma = \sqrt{\epsilon\beta}$.

Using cylindrical coordinates, in the high-gain limit we seek the solution for a slowly varying complex amplitude of the electric field of the electromagnetic wave in the form [21]:

$$\tilde{E}(z, r, \varphi) = \Phi_n(r) \exp(\Lambda z) \begin{pmatrix} \sin(n\varphi) \\ \cos(n\varphi) \end{pmatrix} \ , \tag{3}$$

where n is an integer, $n \geq 0$. For each n there are many radial eigenmodes that differ by eigenvalue Λ and eigenfunction $\Phi_n(r)$. The integro-differential equation for radiation field eigenmodes [1,8] taking into account the space charge effect [21] can be written in the following normalized form:

$$\begin{aligned}
&\left[\frac{\mathrm{d}^2}{\mathrm{d}\,\hat{r}^2} + \frac{1}{\hat{r}}\frac{\mathrm{d}}{\mathrm{d}\,\hat{r}} - \frac{n^2}{\hat{r}^2} + 2\,\mathrm{i}\,B\hat{\Lambda}\right]\Phi_n(\hat{r}) = -4\int\limits_0^\infty \mathrm{d}\,\hat{r}'\hat{r}'\,\Big\{\Phi_n(\hat{r}') \\
&+\frac{\hat{\Lambda}_{\mathrm{p}}^2}{2}\left[\frac{\mathrm{d}^2}{\mathrm{d}\,\hat{r}'^2} + \frac{1}{\hat{r}'}\frac{\mathrm{d}}{\mathrm{d}\,\hat{r}'} - \frac{n^2}{\hat{r}'^2} + 2\,\mathrm{i}\,B\hat{\Lambda}\right]\Phi_n(\hat{r}')\Big\} \\
&\times\int\limits_0^\infty \mathrm{d}\,\zeta\frac{\zeta}{\sin^2(\hat{k}_\beta\zeta)}\exp\left[-\frac{\hat{\Lambda}_{\mathrm{T}}^2\zeta^2}{2} - (\hat{\Lambda} + \mathrm{i}\,\hat{C})\zeta\right] \\
&\times\exp\left[-\frac{(1 - \mathrm{i}\,B\hat{k}_\beta^2\zeta/2)(\hat{r}^2 + \hat{r}'^2)}{\sin^2(\hat{k}_\beta\zeta)}\right] \\
&\times I_n\left[\frac{2(1 - \mathrm{i}\,B\hat{k}_\beta^2\zeta/2)\hat{r}\hat{r}'\cos(\hat{k}_\beta\zeta)}{\sin^2(\hat{k}_\beta\zeta)}\right] \ ,
\end{aligned} \tag{4}$$

where I_n is the modified Bessel function of the first kind. The following notations are used here: $\hat{r} = r/(\sigma\sqrt{2})$, $B = 2\sigma^2\Gamma\omega/c$ is the diffraction parameter, $\hat{k}_\beta = k_\beta/\Gamma$ is the betatron motion parameter, $\hat{\Lambda}_{\mathrm{p}}^2 = 2c^2(A_{\mathrm{JJ}}\theta_{\mathrm{s}}\sigma\omega)^{-2}$ is the space charge parameter, $\hat{\Lambda}_{\mathrm{T}}^2 = \langle(\Delta\mathcal{E})^2\rangle/(\rho^2\mathcal{E}^2)$ is the energy spread parameter, $\hat{C} = [k_{\mathrm{w}} - \omega/(2c\gamma_z^2)]\,/\Gamma$ is the detuning parameter, $\Gamma = \left[A_{\mathrm{JJ}}^2 I_0\omega^2\theta_{\mathrm{s}}^2\,(I_{\mathrm{A}}c^2\gamma_z^2\gamma)^{-1}\right]^{1/2}$ is the gain parameter, $\rho = c\gamma_z^2\Gamma/\omega$ is the efficiency parameter, ω is the frequency of the electromagnetic wave, $\theta_{\mathrm{s}} = K_{\mathrm{rms}}/\gamma$, K_{rms} is the rms undulator parameter, γ is relativistic factor, $\gamma_z^{-2} = \gamma^{-2} + \theta_{\mathrm{s}}^2$, k_{w} is the undulator wavenumber, $I_{\mathrm{A}} = 17$ kA is the Alfven current, $A_{\mathrm{JJ}} = 1$ for helical undulator and $A_{\mathrm{JJ}} = J_0(K_{\mathrm{rms}}^2/2(1+K_{\mathrm{rms}}^2)) - J_1(K_{\mathrm{rms}}^2/2(1+K_{\mathrm{rms}}^2))$ for planar undulator. Here J_0 and J_1 are the Bessel functions of the first kind. The space charge effect is included into (4) under the condition $\sigma^2 \gg c^2\gamma_z^2/\omega^2$.

3. Exact solution

As suggested in [1] we apply to (4) the Hankel transformation defined by the following transform pair:

$$\bar{\Phi}_n(p) = \int\limits_0^\infty \mathrm{d}\,\hat{r}\hat{r}J_n(p\hat{r})\Phi_n(\hat{r}) \ , \qquad \Phi_n(\hat{r}) = \int\limits_0^\infty \mathrm{d}\,ppJ_n(p\hat{r})\bar{\Phi}_n(p) \ .$$

Then we obtain the integral equation for the Hankel transform $\bar{\Phi}_n(p)$:

$$\begin{aligned} \bar{\Phi}_n(p) = & -\frac{1}{2\,\mathrm{i}\,B\hat{\Lambda} - p^2}\int\limits_0^\infty \mathrm{d}\,p'p'\bar{\Phi}_n(p')\left[1 + \frac{\hat{\Lambda}_{\mathrm{p}}^2(2\,\mathrm{i}\,B\hat{\Lambda} - p'^2)}{2}\right] \\ & \times \int\limits_0^\infty \mathrm{d}\,\zeta \frac{\zeta}{(1-\mathrm{i}\,B\hat{k}_\beta^2\zeta/2)^2}\exp\left[-\frac{\hat{\Lambda}_{\mathrm{T}}^2\zeta^2}{2} - (\hat{\Lambda}+\mathrm{i}\,\hat{C})\zeta\right] \\ & \times \exp\left[-\frac{p^2+p'^2}{4(1-\mathrm{i}\,B\hat{k}_\beta^2\zeta/2)}\right] I_n\left[\frac{pp'\cos(\hat{k}_\beta\zeta)}{2(1-\mathrm{i}\,B\hat{k}_\beta^2\zeta/2)}\right] \ . \end{aligned} \tag{5}$$

When the space charge field is negligible, $\hat{\Lambda}_{\mathrm{p}}^2 \to 0$, this equation is reduced to one obtained in [1].

To solve (5) we discretize it:

$$p_i = \Delta(i - \frac{1}{2}) \ , \qquad i = 1, 2, ..., K \ ,$$

$$p'_j = \Delta(j - \frac{1}{2}) \ , \qquad j = 1, 2, ..., K \ ,$$

where Δ and K should be chosen in such a way that the required accuracy is provided. Then we obtain a matrix equation

$$\bar{\Phi}_n(i) = M_n(i,j)\bar{\Phi}_n(j) \ ,$$

or, $[M_n - I]\bar{\Phi}_n = 0$, where I is a unit matrix. Matrix M_n depends on an eigenvalue $\hat{\Lambda}$ as well as on the problem parameters: B, $\hat{k}_\beta$, $\hat{\Lambda}_{\mathrm{T}}^2$, $\hat{\Lambda}_{\mathrm{p}}^2$, and $\hat{C}$. The eigenvalues of all radial

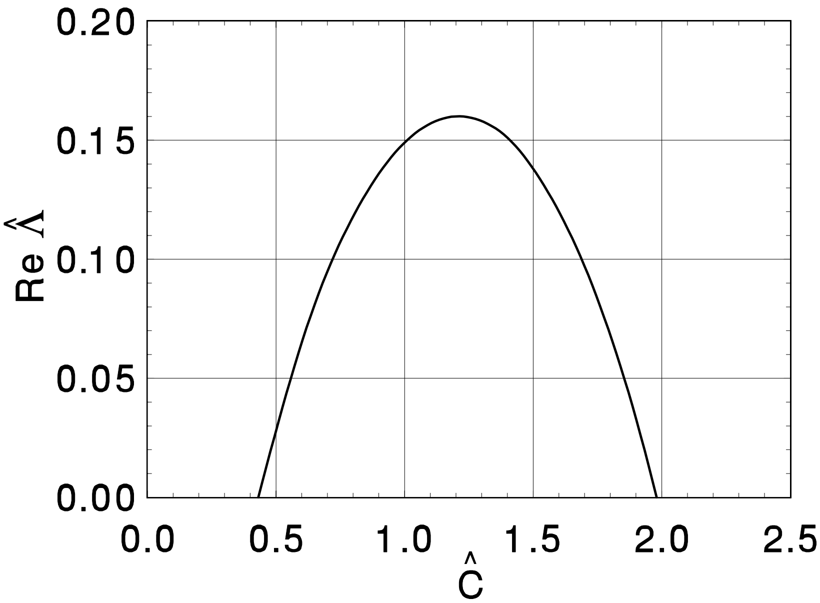

Fig. 1. Reduced growth rate of TEM_{00} mode versus detuning parameter. Here $B = 1$, $\hat{k}_\beta = 1$, $\hat{\Lambda}_\mathrm{p}^2 = 0.5$, and $\hat{\Lambda}_\mathrm{T}^2 = 0.2$

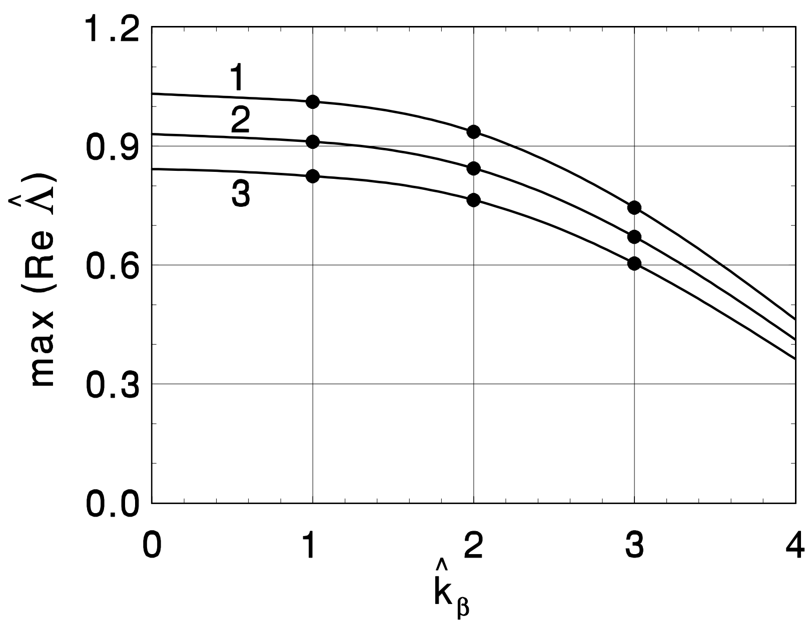

Fig. 2. Reduced growth rate of TEM_{00} mode at the optimal detuning versus betatron motion parameter. Here $B = 0.1$ and $\hat{\Lambda}_\mathrm{p}^2 \to 0$. Curve (1): $\hat{\Lambda}_\mathrm{T}^2 = 0$, Curve (2): $\hat{\Lambda}_\mathrm{T}^2 = 0.1$, Curve (3): $\hat{\Lambda}_\mathrm{T}^2 = 0.2$. Curves are the results of approximate solution and circles are the results of exact solution

modes for a given azimuthal index n can be found by solving the equation $|M_n - I| = 0$. Then the calculation of the eigenmodes is straightforward.

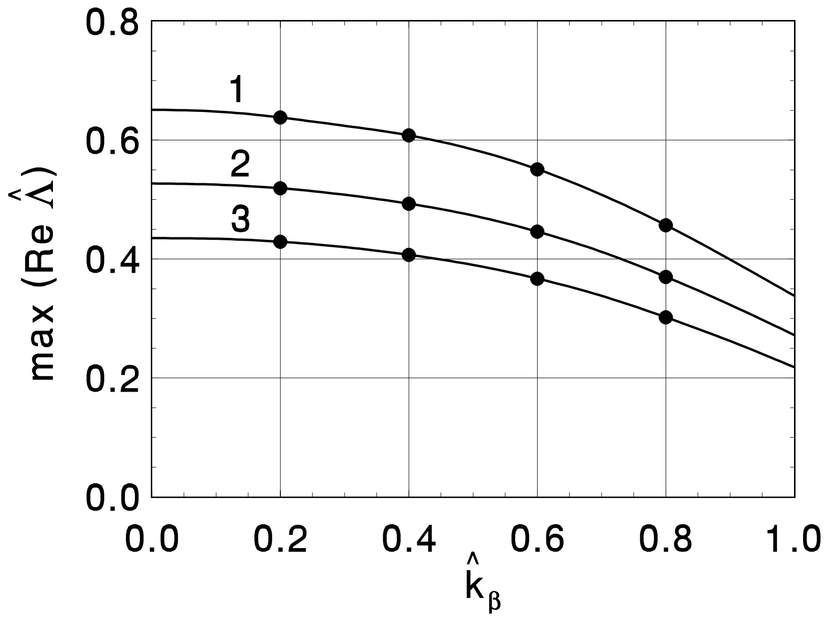

Fig. 3. Reduced growth rate of TEM_{00} mode at the optimal detuning versus betatron motion parameter. Here $B = 1$ and $\hat{\Lambda}_{\mathrm{p}}^2 \to 0$. Curve (1): $\hat{\Lambda}_{\mathrm{T}}^2 = 0$, Curve (2): $\hat{\Lambda}_{\mathrm{T}}^2 = 0.1$, Curve (3): $\hat{\Lambda}_{\mathrm{T}}^2 = 0.2$. Curves are the results of approximate solution and circles are the results of exact solution

This algorithm allows one to find with any desirable accuracy the eigenvalues and eigenfunctions of a high-gain FEL including all the important effects: diffraction, betatron motion, energy spread, space charge, and frequency detuning (see Fig. 1 as an example). Therefore, it can be considered as a universal tool for calculation and optimization of FEL amplifiers of wavelength range from infrared down to X-ray. The only disadvantage is that the algorithm becomes time-consuming when one needs a reasonable accuracy of calculations.

4. Approximate solution for TEM_{00} mode

For quick optimization of high-gain FELs one needs fast and, at the same time, pretty accurate procedure for the determination of eigenvalues. Usually the eigenvalue of ground TEM_{00} mode is the subject of optimization because FELs are designed in such a way that only this mode survives in the end of amplification process. Thus, we will look for an approximate solution only for the ground mode. Different approaches for obtaining approximate solutions have been developed [1,9,10]. We consider here the one described in [1] and then we introduce the new method allowing us to improve the accuracy of the solution.

As it has been done in [1], we construct a variational functional from (4), use a trial

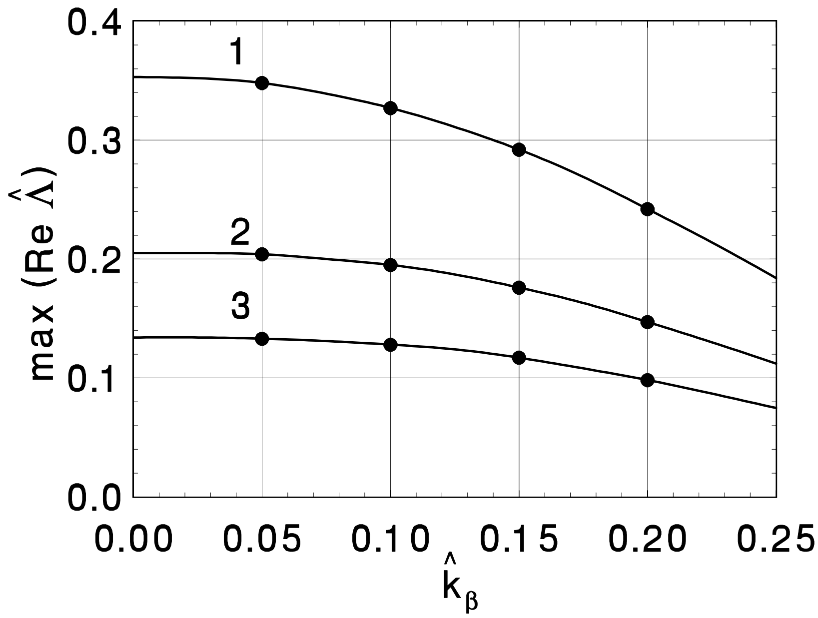

Fig. 4. Reduced growth rate of TEM_{00} mode at the optimal detuning versus betatron motion parameter. Here $B = 10$ and $\hat{\Lambda}_{\mathrm{p}}^2 \to 0$. Curve (1): $\hat{\Lambda}_{\mathrm{T}}^2 = 0$, Curve (2): $\hat{\Lambda}_{\mathrm{T}}^2 = 0.1$, Curve (3): $\hat{\Lambda}_{\mathrm{T}}^2 = 0.2$. Curves are the results of approximate solution and circles are the results of exact solution

function in the form

$$\Phi_0(\hat{r}) = \exp(-a\hat{r}^2) \ , \tag{6}$$

and apply the variational condition, $\delta\hat{\Lambda}/\delta a = 0$. As a result, we obtain two equations for two unknown quantities, $\hat{\Lambda}$ and a:

$$1 - \frac{\mathrm{i}\, B\hat{\Lambda}}{a} - 2\int\limits_0^\infty \mathrm{d}\,\zeta\zeta \frac{\exp\left[-\hat{\Lambda}_{\mathrm{T}}^2\zeta^2/2 - (\hat{\Lambda} + \mathrm{i}\,\hat{C})\zeta\right]}{f_2(\zeta)} = 0 \ , \tag{7}$$

$$\frac{\mathrm{i}\, B\hat{\Lambda}}{a^2} + 4\int\limits_0^\infty \mathrm{d}\,\zeta\zeta \frac{f_1(\zeta)\exp\left[-\hat{\Lambda}_{\mathrm{T}}^2\zeta^2/2 - (\hat{\Lambda} + \mathrm{i}\,\hat{C})\zeta\right]}{f_2^2(\zeta)} = 0 \ , \tag{8}$$

where

$$f_1(\zeta) = 1 - \mathrm{i}\, B\hat{k}_\beta^2\zeta/2 + a\sin^2(\hat{k}_\beta\zeta) \ ,$$

$$f_2(\zeta) = (1 - \mathrm{i}\, B\hat{k}_\beta^2\zeta/2)^2 + 2a(1 - \mathrm{i}\, B\hat{k}_\beta^2\zeta/2) + a^2\sin^2(\hat{k}_\beta\zeta) \ .$$

These equations are obtained under the condition $\hat{\Lambda}_{\mathrm{p}}^2 \to 0$. The solution of the system of equations (7) and (8) is accurate at large values of the diffraction parameter, $B \gg 1$, when the radiation field is concentrated inside the electron beam and is well described by function (6). On the other hand, it becomes highly inaccurate at small values of B. For instance, in the limit of parallel beam, $\hat{k}_\beta = 0$, negligible energy spread, $\hat{\Lambda}_{\mathrm{T}}^2 = 0$, and small diffraction parameter, $B \to 0$, we get $\max(\mathrm{Re}\,\hat{\Lambda}) \to \sqrt{2}$ (at the optimal detuning $\hat{C}$) instead of the well-known logarithmic asymptote [3,4]. In this limit the mode size is much larger than the electron beam size and the actual behaviour of the field at large $\hat{r}$ is $\Phi_0(\hat{r}) \propto \exp(-g\hat{r})$ [21] rather than (6).

In order to improve the accuracy of the solution in the whole range of parameters we propose to find the second approximation to the eigenvalue and the eigenfunction in the following way. We modify the r.h.s. of (4) assuming the function $\Phi_0(\hat{r})$ to be of the form (6) with the definite value of the parameter a that is already found by solving the system of equations (7) and (8). As a result, we approximate the integro-differential equation (4) by a differential equation (the space charge effect is again neglected here):

$$\left[\frac{\mathrm{d}^2}{\mathrm{d}\,\hat{r}^2} + \frac{1}{\hat{r}}\frac{\mathrm{d}}{\mathrm{d}\,\hat{r}} + \mu^2(\hat{r})\right]\Phi_0(\hat{r}) = 0 \ , \tag{9}$$

where

$$\mu^2(\hat{r}) = -g^2 + 2\exp(-\hat{r}^2)\int\limits_0^\infty \mathrm{d}\,\zeta\zeta f_1^{-1}(\zeta)\exp\left[-\frac{\hat{\Lambda}_{\mathrm{T}}^2\zeta^2}{2} - (\hat{\Lambda} + \mathrm{i}\,\hat{C})\zeta\right]$$
$$\times\exp\left[\frac{\mathrm{i}\,B\hat{k}_\beta^2\zeta/2(1 - \mathrm{i}\,B\hat{k}_\beta^2\zeta/2) + a(1+a)\sin^2(\hat{k}_\beta\zeta)}{f_1(\zeta)}\hat{r}^2\right] \ , \tag{10}$$

and $g^2 = -2\,\mathrm{i}\,B\hat{\Lambda}$. In the limit of parallel beam, $\hat{k}_\beta \to 0$, equation (9) is reduced to the well-known one [21].

New approximations to the eigenvalue $\hat{\Lambda}$ and the eigenfunction $\Phi_0(\hat{r})$ should be determined from (9). To do this we use the multilayer approximation method [6,21] that allows us to solve the equation (9) for an arbitrary function $\mu(\hat{r})$. We cut out the density distribution $\exp(-\hat{r}^2)$, entering $\mu^2(\hat{r})$, at some point $\hat{r} = \hat{r}_{\mathrm{b}}$ so that $\mu^2 = -g^2$ for $\hat{r} > \hat{r}_{\mathrm{b}}$. We divide the region $0 < \hat{r} < \hat{r}_{\mathrm{b}}$ into K layers. The function $\mu(\hat{r})$ is assumed to be constant within each layer. The solution for the eigenfunction within each layer is

$$\Phi_0^{(j)} = A_j J_0(\mu_j\hat{r}) + D_j N_0(\mu_j\hat{r}) \ ,$$

where $(j-1)/K < \hat{r} < j\hat{r}_{\mathrm{b}}/K$, A_j and D_j are constants, $\mu_j = \mu(\hat{r}_{j-1/2})$ and $\hat{r}_{j-1/2} = \hat{r}_{\mathrm{b}}(j-1/2)/K$, J_0 and N_0 are the Bessel functions of the first and of the second kind, respectively. To avoid a singularity of the eigenfunction at $\hat{r} = 0$, we should let $D_1 = 0$. All the other coefficients are obtained from the continuity conditions for the eigenfunction and its derivative at the boundaries between the layers. These equations can be written in the matrix form:

$$\begin{pmatrix} A_{j+1} \\ D_{j+1} \end{pmatrix} = T_j \begin{pmatrix} A_j \\ D_j \end{pmatrix} , \qquad j = 1,\ 2,\ \ldots\ ,\ K-1 \ , \tag{11}$$

where the coefficients T_j are given by ($\hat{r}_j = \hat{r}_\mathrm{b} j/K$):

$$\begin{aligned}
(T_j)_{11} &= (\pi/2)\hat{r}_j\, [\mu_j J_1(\mu_j \hat{r}_j) N_0(\mu_{j+1}\hat{r}_j) \\
&\quad - \mu_{j+1} J_0(\mu_j \hat{r}_j) N_1(\mu_{j+1}\hat{r}_j)] \ , \\
(T_j)_{12} &= (\pi/2)\hat{r}_j\, [\mu_j N_1(\mu_j \hat{r}_j) N_0(\mu_{j+1}\hat{r}_j) \\
&\quad - \mu_{j+1} N_0(\mu_j \hat{r}_j) N_1(\mu_{j+1}\hat{r}_j)] \ , \\
(T_j)_{21} &= -(\pi/2)\hat{r}_j\, [\mu_j J_1(\mu_j \hat{r}_j) J_0(\mu_{j+1}\hat{r}_j) \\
&\quad - \mu_{j+1} J_0(\mu_j \hat{r}_j) J_1(\mu_{j+1}\hat{r}_j)] \ , \\
(T_j)_{22} &= -(\pi/2)\hat{r}_j\, [\mu_j N_1(\mu_j \hat{r}_j) J_0(\mu_{j+1}\hat{r}_j) \\
&\quad - \mu_{j+1} N_0(\mu_j \hat{r}_j) J_1(\mu_{j+1}\hat{r}_j)] \ .
\end{aligned} \tag{12}$$

The solution for the eigenfunction outside the beam, $\hat{r} > \hat{r}_\mathrm{b}$, satisfying the condition of quadratic integrability is

$$\Phi_0(\hat{r}) = F_1 K_0(g\hat{r}) \ , \quad \mathrm{Re}\, g > 0 \ ,$$

where K_0 is the modified Bessel function of the second order. At the beam boundary, at $\hat{r} = \hat{r}_\mathrm{b}$, the continuity condition gives the following relations:

$$A_K J_0(\mu_K \hat{r}_\mathrm{b}) + D_K N_0(\mu_K \hat{r}_\mathrm{b}) = F_1 K_0(g\hat{r}_\mathrm{b}) \ ,$$

$$\mu_K A_K J_1(\mu_K \hat{r}_\mathrm{b}) + \mu_K D_K N_1(\mu_K \hat{r}_\mathrm{b}) = g F_1 K_1(g\hat{r}_\mathrm{b}) \ ,$$

which can also be written in the matrix form:

$$T_K \begin{pmatrix} A_K \\ D_K \end{pmatrix} = F_1 \begin{pmatrix} 1 \\ 1 \end{pmatrix} \ . \tag{13}$$

The coefficient F_1 can be expressed in terms of the coefficient A_1 by multiple use of (11). The coefficient A_1 may be chosen arbitrarily, so without loss of generality we let $A_1 = 1$. Then we can write the following matrix equation:

$$T_K \times T_{K-1} \times\ \ldots\ \times T_1 \begin{pmatrix} 1 \\ 0 \end{pmatrix} = T \begin{pmatrix} 1 \\ 0 \end{pmatrix} = F_1 \begin{pmatrix} 1 \\ 1 \end{pmatrix} \ , \tag{14}$$

where the matrix T depends on the unknown quantity $\hat{\Lambda}$. Another unknown quantity in

(14) is the coefficient F_1, which can be easily excluded. Thus, we obtain the eigenvalue equation

$$(T)_{11} = (T)_{21} \ , \tag{15}$$

which allows one to find the eigenvalue $\hat{\Lambda}$. The eigenfunction is calculated using (11) and (13).

The accuracy of this algorithm was tested by comparison with the exact solution described above. For any set of parameters chosen the accuracy was better than 1%. This can be explained as follows. As we have already mentioned, at large values of the diffraction parameter B the eigenfunction is correctly described by (6) and the variational method gives accurate result. The second approximation (solution of the differential equation (9)) almost does not differ from the variational solution. In the opposite limit, $B \to 0$, the variational method gives a wrong shape of the eigenfunction. Nevertheless, this does not matter for our solution because in this limit the field is much wider than the electron beam and, therefore, is almost constant within the beam. In other words, in this limit the source term (r.h.s. of equation (4)) is independent of the first approximation to $\Phi_0(\hat{r})$ obtained from variational method. Then, solving (9) one gets accurate eigenfunction and eigenvalue. Thus, our solution has correct behaviour in both limits of weak and strong diffraction. In addition, it is always correct in the limit of parallel beam. In fact, the approximate solution presented here fits very well the exact solution in the whole region of parameters. At the same time, the numerical algorithm to find the approximate solution is much faster than in case of the exact solution. In Figs. 2-4 we present some results of the eigenvalue calculation obtained with both methods.

References

[1] M. Xie, Nucl. Instrum. and Methods **A445**(2000)59

[2] N.M. Kroll and W.A. McMullin, Phys. Rev. **A17**(1978)300

[3] A.M. Kondratenko and E.L. Saldin, Part. Acc. **10**(1980)207

[4] G.T. Moore, Opt. Comm. **52**(1984)46

[5] M. Xie and D. Deacon, Nucl. Instrum. and Methods **A250**(1986)426

[6] E.L. Saldin, E.A. Schneidmiller and M.V. Yurkov, Opt. Commun. **97**(1993)272

[7] K.J. Kim, Phys. Rev. Lett. **57**(1986)1871

[8] L.H. Yu and S. Krinsky, Physics Lett. **A129**(1988)463

[9] L.H. Yu, S. Krinsky and R.L. Gluckstern, Phys. Rev. Lett. **64**(1990)3011

[10] Y.H. Chin, K.J. Kim and M. Xie, Nucl. Instrum. and Methods **A318**(1992)481

[11] M. Xie, Nucl. Instrum. and Methods **A445**(2000)67

[12] J. Rossbach, Nucl. Instrum. and Methods **A375**(1996)269

[13] "Conceptual Design of a 500 GeV e+e− Linear Collider with Integrated X-ray Laser Facility" (Editors R.Brinkmann, G. Materlik, J. Rossbach, A. Wagner), DESY 97-048, Hamburg, 1997.

[14] "Linac Coherent Light Source Design Study Report", SLAC-R-521, Stanford, 1998

[15] M. Hogan et al., Phys. Rev. Lett. **81**(1998)4867

[16] E.L. Saldin, E.A. Schneidmiller and M.V. Yurkov, Nucl. Instrum. and Methods **A429**(1999)197

[17] E.L. Saldin et al., "Photon Linear Colliders of TeV Energy Range", preprint JINR E-9-94-74, Dubna, 1994

[18] B. Faatz et al., preprint DESY-00-095, Hamburg, 2000

[19] C. Pagani et al., Nucl. Instrum. and Methods **A423**(1999)190

[20] E.L. Saldin, E.A. Schneidmiller and M.V. Yurkov, "The General Solution of the Eigenvalue Problem for a High-Gain FEL Including Alternating-Gradient Focusing", to be published

[21] E.L. Saldin, E.A. Schneidmiller and M.V. Yurkov, "The Physics of Free Electron Lasers", Springer, Berlin, 1999

First Results of the High Resolution Wire Scanners for Beam Profile and absolute Beam Position Measurement at the TTF

G. Schmidt, U. Hahn, M. Meschkat, F. Ridoutt

Deutsches Elektronen-Synchrotron DESY, Notkestr. 85, 22603 Hamburg, Germany

Abstract

In the TESLA Test Facility (TTF), wire scanners are used to measure the electron beam profile and position. Especially the intended use of the wire scanners to centre the electron beam in the Free Electron Laser (FEL) undulator needs a precise alignment of the wire scanners in respect to the undulator axis.

The wire scanners should define a reference axis with respect to the external reference system of the undulator with an accuracy better than 30 µm.

The wire scanners allow a beam profile measurement which will be used to optimise and match the beam optics for the undulator. First experimental results of beam position and profile will be presented and discussed.

1. INTRODUCTION

The undulator at the TTF-FEL consists of three undulator modules.

The narrow space between and at both ends of the undulator modules is used for diagnostic.

Two types of monitors are included in a so-called diagnostic block.

RF type cavity monitors for horizontal and vertical beam position measurement and vertical and horizontal wire scanners allow to measure the beam profile and position [1].

The beam position can be measured with respect to external reference marks so that the position of the beam before, after and in between the undulator segments at several fix points is known.

Figure 1 shows a photograph of the diagnostic block between two undulator sections.

The principle set-up of the wire scanners is sketched in figure 2. Each wire scanner fork (wire holder) is equipped with 3 wires. One tungsten wire of a diameter of 20 µm, and two carbon wires of a diameter of 5 µm. This allows to select the wire as a function of beam size, beam intensity and required resolution. Electrons hitting a wire produce scattered electrons, which are detected by scintillation counters.

Behind each pair of wire scanners, a scintillation counter is installed covering nearly 360° around the beam tube [2].

The main difficulties that had to be overcome were:

- *The cleaning and assembly of the complicated diagnostic block.* Together with the attached components like rf Feedthroughs, the assembly had to take place under clean room conditions according to TTF specifications (clean room better than class 100) [3].
- *The alignment and stretching of wires.* The tightening of the wires in the fork is very critical. It is difficult to stretch the wires to a straight line and fix them. After installation the wires have to pass the narrow rf shielding slit (width 1.5 mm) in the diagnostic block during the scan of the beam profile. The alignment is extremely crucial since small deviations from the centre of the slit cause the damage of all wires.
- *The calibration of the wire scanner in the diagnostic block.* The goal of this calibration is to measure the position of the wires with respect to the reference planes of the diagnostic block smaller than 30 μm in both planes. This calibration was done using a vertical coordinate measuring machine (CMM). A local clean room was installed in front of the machine. The diagnostic block was under clean room conditions during the entire calibration measurement. To measure the wire position a microscope was mounted to the CMM. It allowed to see the thin wires and to measure the distance of the wires to the reference planes. Reproducibility was achieved by a linear encoder connected to the linear driving system of the wire scanner.

2. RESULTS

Figure 3 presents the results of all eight wire scanner measurements recorded during FEL operation of the TTF linac. The electron beam profile measurements were done with the 20 μm thick tungsten wire. The tungsten wire was chosen to get sufficient intensity on the scintillation counter.

The signal from the carbon wires wasto small to be detected. By reducing the background (less beam loss before and inside the undulator area) and reducing the electron beam spot size, the signal-to-noise ratio can be improved.

The measured profiles indicate that the beam offset along the entire undulator stays below 300 μm during SASE operation.

The spot size is somewhat larger than expected. Measurements have shown that a part of the spot size is generated by dispersion.

Each undulator has a superimposed FODO structure of 10 quadrupoles per undulator [4]
In addition to the wire scanners ten beam position monitors (BPM), which allow the measurement of the beam position inside the quadrupoles, are installed along the undulator chamber [5].

Figure 4 gives a comparison between the beam position measured by the wire scanners and the BPMs inside the first two undulators. It is clear that the BPMs show some random position deviations due to the fact that they had not been calibrated. The fit of a betatron motion to both, the 20 BPMs and the four wire scanner readings, results in a similar betatron amplitude and phase of the beam motion.
The measurement of a difference orbit, implemented by a kick before the undulator, allows to verify the beam optics inside the undulator by comparison of the expected and measured betatron motion.
Figure 5 shows the good agreement of the measured and calculated difference orbits.
The betatron motion is just fitted in amplitude and phase to the measured difference orbit.
Both measurements (wire scanner and BPMS) result in the same difference orbit. The agreement with the calculated betatron motion is very good (~50 μm).

3 CONCLUSION

The eight wire scanner allow to measure the beam profile and the beam position with high reproducibility and accuracy (better than 30 μm). Good agreement between the calculated and measured phase advance inside the undulator was observed. The position measurements of the wire scanners are in good agreement with the 20 distributed BPMs.

4 REFERENCES

[1] U. Hahn, J. Pflüger, G. Schmidt, Nucl. Instr. Meth. A429 (1999) 276.

[2] S. Striganov. G. Schmidt, K. Wittenburg, Estimation of the Signal from the Wire Scanner in the TTF, TESLA Report, TESLA 99-08.

[3] D. Edwards et al., Proposed cleaning procedures for the Vacuum Components for the TESLA Test Facility, TESLA Report 15 (1997)

[4] Y. Nikitina and J. Pflüger, Nucl. Instr. And Meth. A375,325 (1996)

[5] Hahn et al., Design and Performance of the Vacuum Chambers for the Undulator for the VUV FEL at the TESLA Test Facility at DESY, Proceedings FEL Conference 2000.

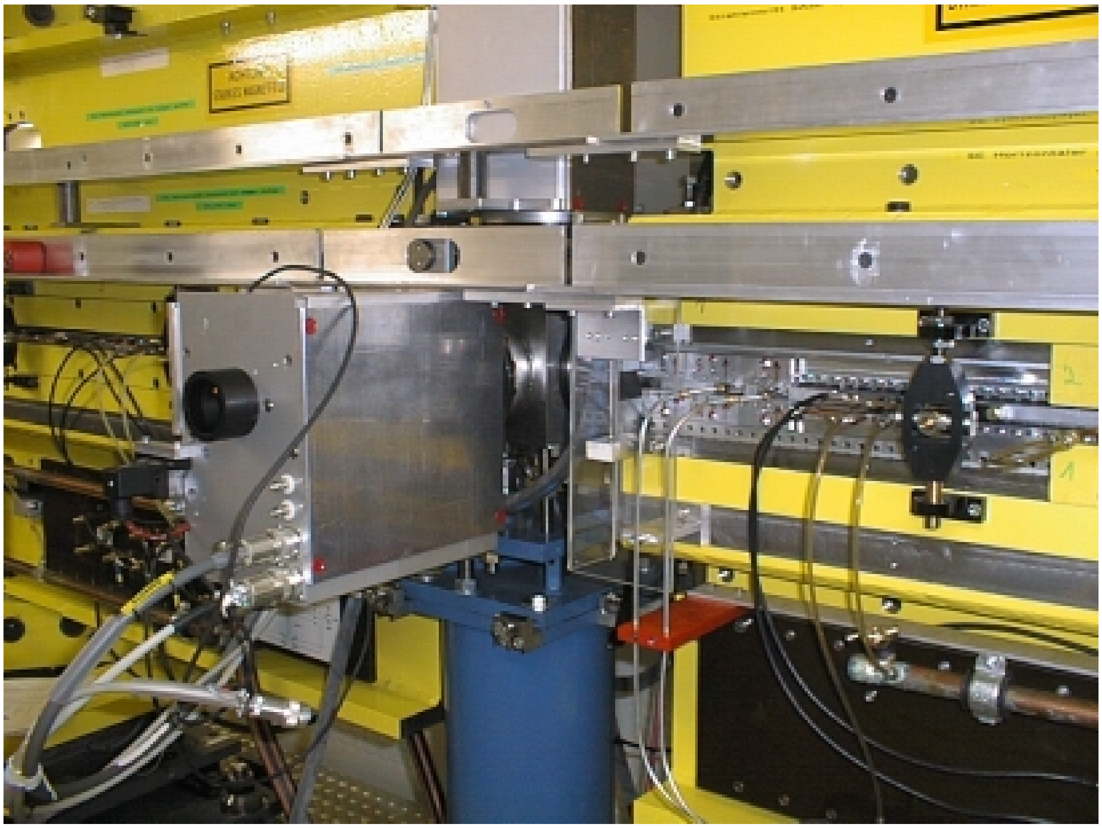

Fig.1: Diagnostic block between two undulator sections.

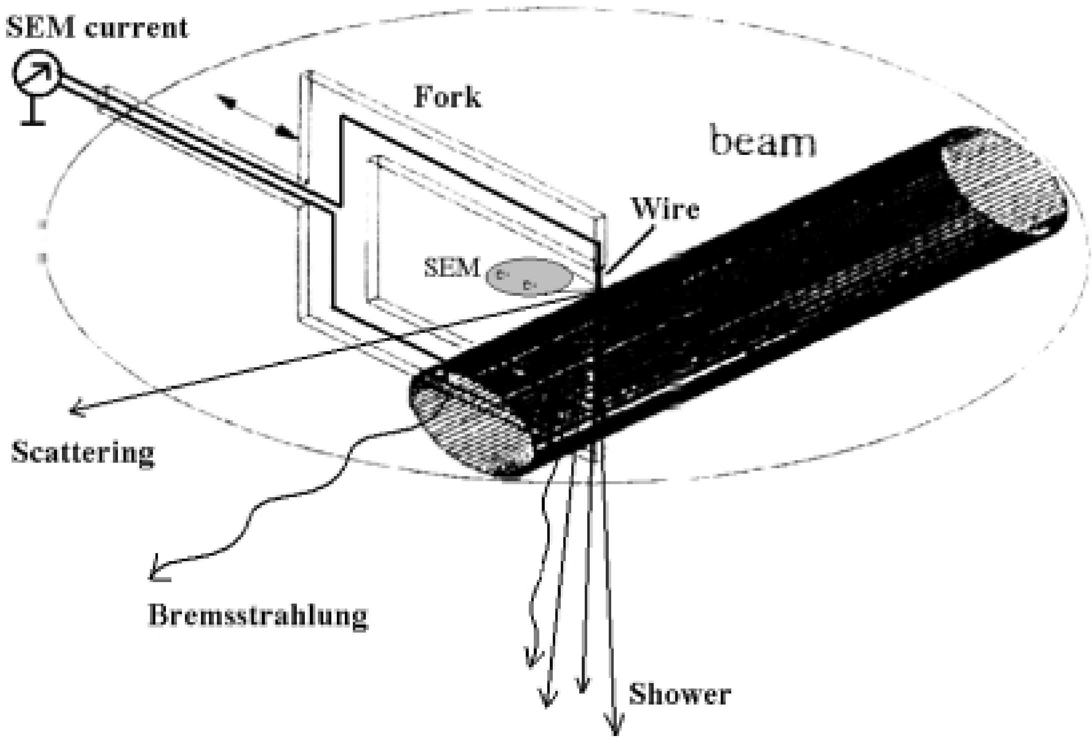

Fig.2: Possibilities to detect the wire scanner signals

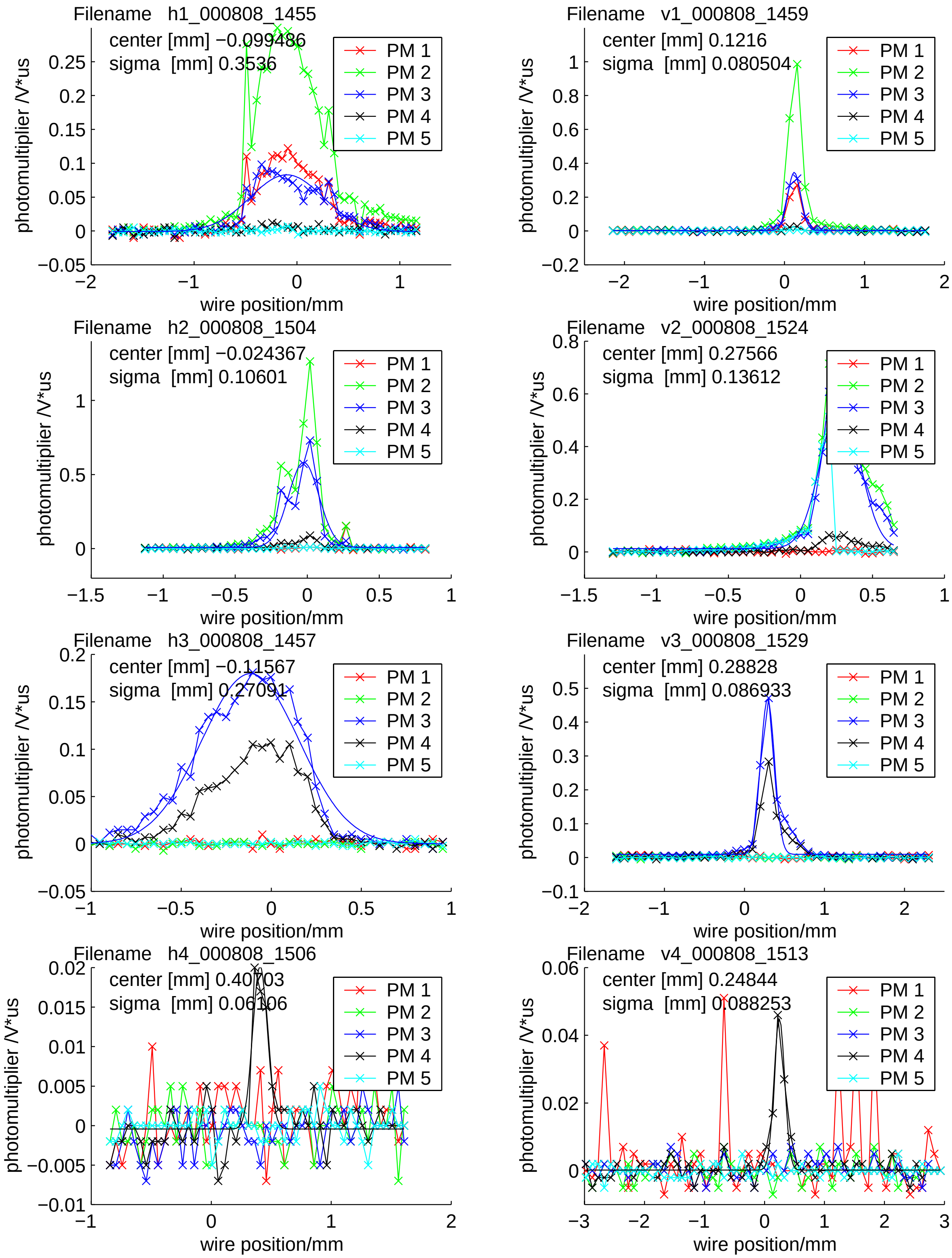

Fig . 3: Measurement of beam profiles using the wire scanner.

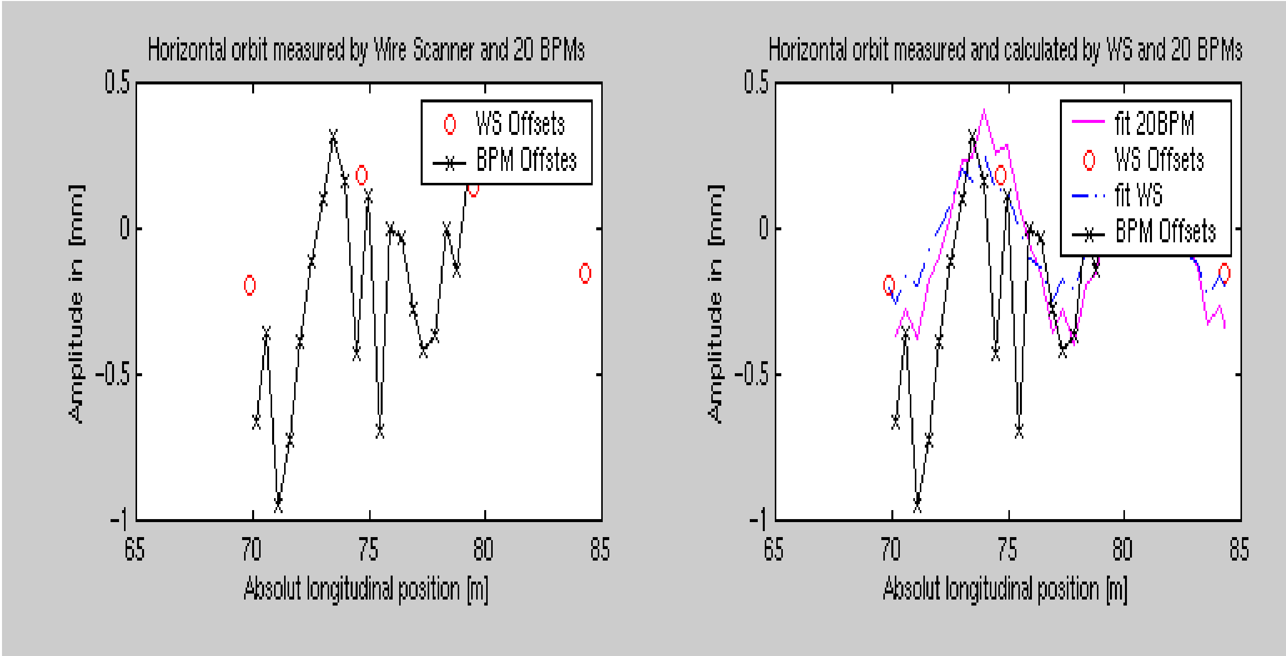

Fig.4: BPM and Wire Scanner Measurement

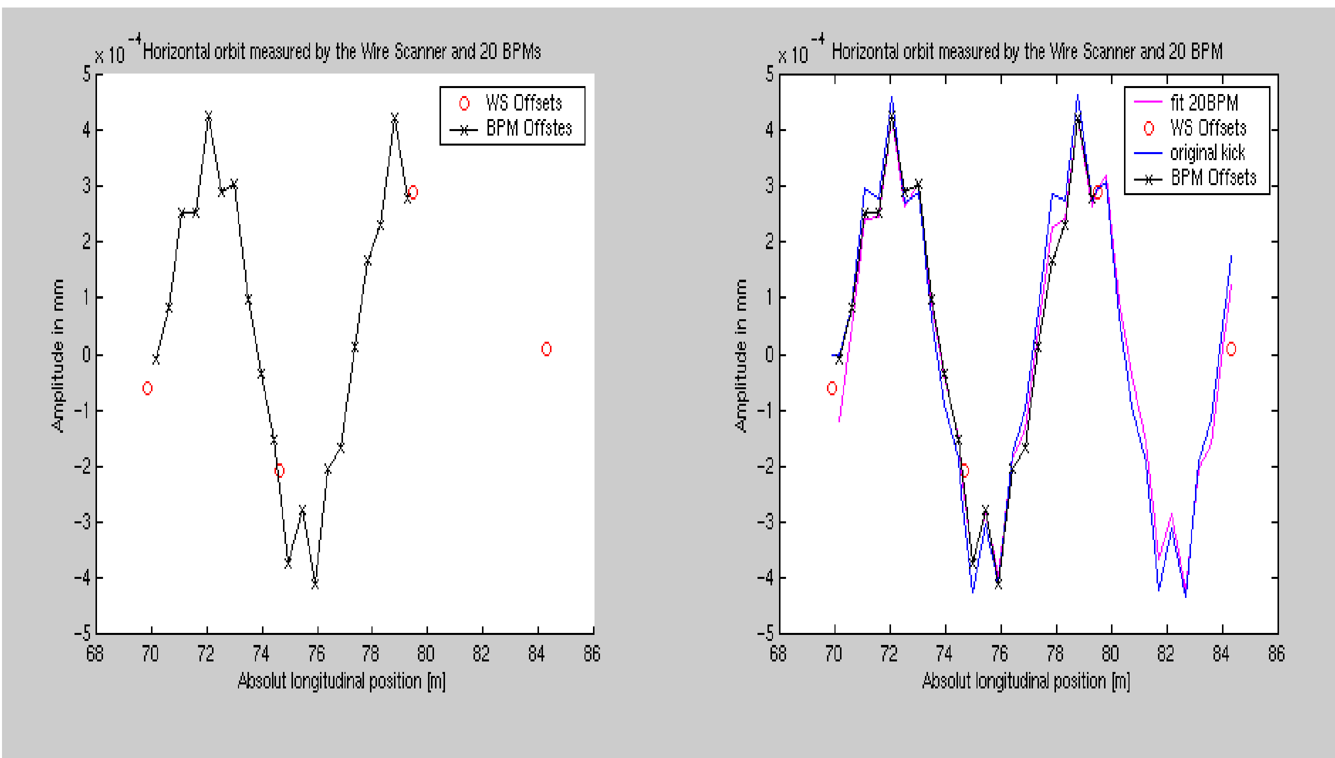

Fig.5: Difference orbit by implementing a kick to the beam before it enters the undulator

Dark current at TTFL rf-gun

D. Sertore[a], S. Schreiber[a] K. Zapfe[a] D. Hubert[a] and P. Michelato[b]

[a]Deutsches Elektronen Synchrotron,
Notkestrasse 85,D-22603 Hamburg, Germany

[b]INFN Milano-LASA, Via F.lli Cervi 201, I-20090 Segrate, Italy

During the last run, dark current measurements have been routinely done at TTFL rf-gun. Effects on beam performance and linac operation are presented.

1. Introduction

The TESLA Test Facility Linac (TTFL)[1] uses an RF photoinjector and a superconducting linac to accelerate electrons for the TTF free electron laser (TTF-FEL)[2]. The photoinjector is based on an RF gun operated at 35 MV/m, 100 μs rf flat top pulse length. The electron source is a Cs_2Te photocathodes illuminated by UV laser light. The 4^{th} harmonic (λ= 262 nm) of a Nd:YLF laser[3]is used. Usually a train of bunches, with bunch charge between 1 nC and 8 nC, is generated. The bunch spacing in the train is 1 μs. Dark current is produced along the rf pulse. A possible source of dark current are tips or needles on surfaces exposed to high electric field. The current density due to this field emission is given by the Fowler-Nordheim relation [4]:

$$j \propto (\beta E)^{\frac{5}{2}} exp(-\frac{B}{\beta E}) \tag{1}$$

where E is the electric field amplitude, β is an enhancement factor due to the geometry of the source and B is a material dependent parameter. The dark current is source of undesired beam halo and radiation along the linac. Therefore is important to understand dark current sources in order to reduce them as much as possible.

2. Measurements

The dark current is measured with a Faraday cup that can be inserted at the gun exit. The signal from the Faraday cup is detected with an oscilloscope. A typical signal is reported in Fig. 1. The rising and falling edge of the rf pulse are

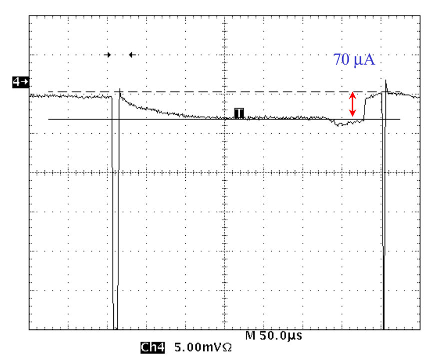

Figure 1. Oscilloscope trace used for dark current measurement. The spikes at the begin and at the end are due to multipactoring during Rf start and stop. The pedestal is due to dark current.

clearly visible as spikes at the beginning and at the end of the pulse. They are due to multipactoring during rise and fall of rf. In between the spikes, a pedestal is visible that grows along the pulse. This pedestal is due to the dark current produced during the Rf pulse. We measure the dark current by measuring the height of the pedestal at the end of the pulse, before the rf stop signal as shown in Fig. 1. From simulations, the source of the dark current is the gun backplane and mainly the region around the cathode. The Rf contact between the cathode and the body of the gun is assured by a CuBe spring. It is possible to image the dark current on a screen downstream from the gun and resolve the spring convolutions. The contribution to the dark current from the photoemissive material is lower than the Faraday Cup sensitivity. The dark current history for the cathodes used is reported in Fig. 2 [5]. The typical initial value of the dark current is below 100 μA after the cathode insertion in the gun. The dark current then rises slowly. Often an abrupt increase is observed that can reach also some mA. Reused cathodes have always an initial dark current value higher than their fresh value and the current rise is earlier and faster. On the contrary, degradation of quantum efficiency has not been observed. The experimental evidences collected till now can be summerized as follows:

- Removing the cathode from the gun and pumping the cathode region lowers the dark current but only for short time.
- The dark current value after the cathode insertion depends on the pumping time.
- Reused cathodes have an earlier and faster dark current rise than new cathodes.
- No clear indication of dark current from the photoemissive area has been collected.

The main effect related to dark current during linac operation is radiation losses in the linac components. In addition, beam jumps were observed. These were due to dark current induced charging of the dielectric mirrors used to point the laser to the cathode. The problem has been solved replacing them with mirror having a metallic bulk material.

3. Conclusions

Measurements and induced effects of dark current have been reported. Studies are in progress in order to find and eliminate the dark current sources. New materials and coatings for the spring are investigated. An activity is in progress also for studying new finishing of the Molybdenum cathode plug.

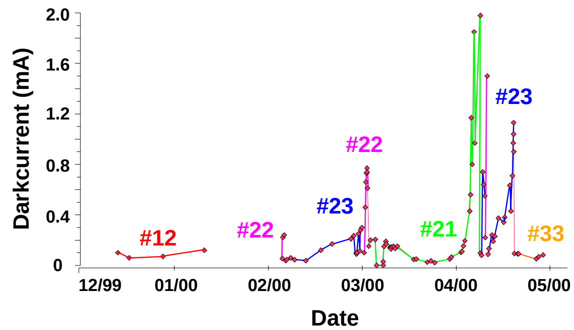

Figure 2. Dark current history for the cathodes used in the gun during the last run. Different cathodes are rappresented by different colors. Note that some cathodes have been used more than once.

REFERENCES

1. D. A. Edwards (Ed.), TESLA-Collaboration, TESLA Test Facility Linac - Design Report, DESY Print March 1995, TESLA 95-01.
2. J. Andruszkow et al., “First Observation of Self-Amplified Spontaneus Emission in Free-Electron Laser at 109 nm Wavelength”, to be published in Phys. Rev. Letters.
3. S. Schreiber et al., “Running experience with the laser system for the RF gun based injector at the TESLA Test Facility linac”, NIM **445** (2000) 427-431.
4. J. W. Wang, “Rf properties of periodic accelerating structure for Linear Colliers”, SLAC-Report-339.
5. S. Schreiber et al., “Performance status of the rf-gun based injector at the TESLA Test Facility”, EPAC 2000 proceedings,Wien.

Photo Injector Test Facility under Construction at DESY Zeuthen*

F. Stephan[a], D. Krämer[b], I. Will[c], and A. Novokhatski[d] for the PITZ Cooperation consisting of

[a]DESY, Notkestraße 85, 22603 Hamburg and Platanenallee 6, 15738 Zeuthen, Germany,

[b]BESSY, Albert-Einstein-Straße 15, 12489 Berlin, Germany,

[c]Max-Born-Institute, Max-Born-Straße 2a, 12489 Berlin, Germany,

[d]TU Darmstadt, Department TEMF, Schloßgartenstraße 8, 64289 Darmstadt, Germany

A **P**hoto **I**njector **T**est Facility is under construction at DESY **Z**euthen (PITZ) within a cooperation of BESSY, DESY, MBI, and TUD. The aim is to develop and operate an optimized photo injector for future free electron lasers and linear accelerators. First operation of the rf-gun is planned for late autumn 2000. In this paper we want to outline the scientific goals, the planned and existing hardware, the status of the project and new developments.

1. Goals

The scientific goal of the project is to operate a test facility for rf-guns and photo injectors in order to optimize injectors for different applications like free electron lasers, production of flat beams for linear colliders and polarized electron sources. We will make comparisons of detailed experimental results with simulations and theoretical predictions. At the beginning we will concentrate on the development of an optimized photo injector for the subsequent operation at the TESLA Test Facility - Free Electron Laser (TTF-FEL) [1]. This also includes the test of new developed components like the laser, cathodes and beam diagnostics under realistic conditions. After the installation of a booster cavity we will be able to test new concepts for the production of flat beams[2]. On a longer term basis we plan to investigate the design of polarized electron sources.

2. Setup

The experimental setup is shown in figure 1. In the future, the teststand will be complemented by more diagnostics, beam optical components and a booster cavity.

*The project is partially funded by the HGF Vernetzungsfond.

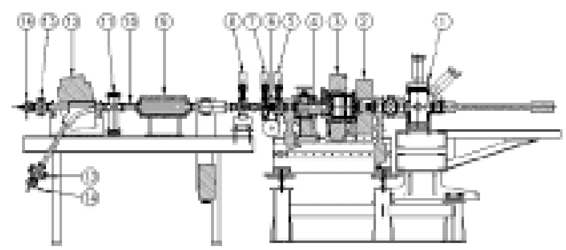

Figure 1. Experimental setup of PITZ in the start-up phase: 1. cathode system, 2. bucking solenoid, 3. main solenoid, 4. coaxial coupler, 5. laser input port, 6. beam position monitor, 7. Faraday cup + view screen, 8. emittance measurement system (slits + pepper pot), 9. quadrupole triplet, 10. wall gap monitor, 11.+13. view screen, 12. dipole, 14. Faraday cup.

3. Schedule and Status

In September 1999 it was decided to built the test facility in DESY Zeuthen. Now the raw construction work is mainly finished and soon we will start the installation of the test stand itself and all the other equipment. We plan to have the first rf inside the gun cavity in November and the first photoelectrons are scheduled for January 2001. A major upgrade of the test stand will take place mid 2002 when a booster cavity will be installed.

4. Laser Development

The Max-Born-Institute develops the photocathode laser for PITZ. Besides the former requirements for the TTF photocathode laser system [3] a new request on the logitudinal shape of the micropulses will be realized by the MBI: the micropulses should have a flat-top profile, 5-20 ps FWHM, with rising and trailing edges shorter than 1 ps. This requires a new laser concept which is shown in figure 2. The key element is the optical-parametric amplifier (OPA). It provides large amplification bandwidth and therefore allows for the amplification of pulses with sharp edges. A grating combination will be used for programming the shape of the micropulses. Wave front deformations will be corrected by computer-controlled optics. An extended version of the field tested TTF photocathode laser will serve as a pump laser for the OPA. In the beginning it will be used to produce the first photoelectrons. Then a continual upgrade to the full laser system follows.

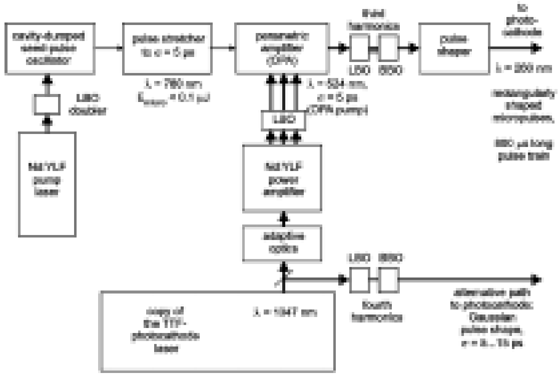

Figure 2. Scheme of the photocathode laser for the generation of micropulses with variable shape.

5. Simulations

One goal of TEMF at TU Darmstadt is the numerical study of the minimum attainable transverse and longitudinal emittance as a function of rf-gun parameters. Figure 3 presents a simulation that takes into account space charge and nonlinear rf forces. It shows that the main part of the transverse emittance is caused by the emission process and that the evolution of the emittance for the first and the second half of the bunch is opposite. The behaviour of the projected emittance seems to be a result of the rf field effects and MAFIA TS2 and ASTRA[4] are shown to be in good agreement. An other topic for TEMF is the development and installation of an on-line simulation program (V-code) [5] that is based on a model of ensembles. It will help to obtain an on-line understanding of the dynamics of the beam. At DESY an ASTRA simulation with a cutted disk structure booster cavity was performed. This cavity provides an average gradient of $\approx$ 12.6 MV/m and boosts the beam up to about 30 MeV. According to that simulation emittances in the sub-mm-mrd regime can be obtained.

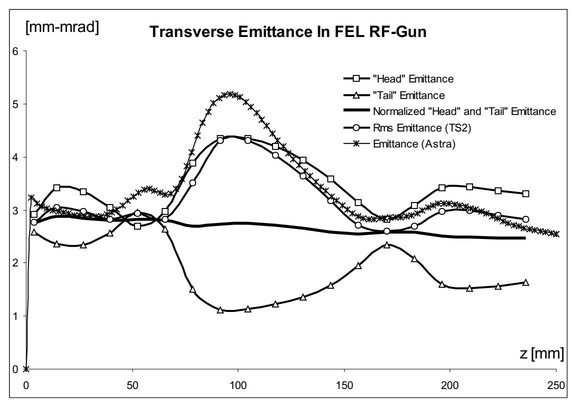

Figure 3. Development of transverse emittance in the rf-gun.

REFERENCES

1. J. Andruszkow et al., First Observation of Self-Amplified Spontaneous Emission in a Free-Electron Laser at 109 nm Wavelength, to be published in Phys. Rev. Lett.
2. R. Brinkmann, Y. Derbenev, K. Flöttmann, A low emittance, flat-beam electron source for linear colliders, EPAC 2000.
3. I. Will, A. Liero, D. Merins, W. Sandner, IEEE Journal of Quantum Electronics, Vol. 34, Oct. 1998, p2020-2028.
4. K. Flöttmann, ASTRA user manual, see www.desy.de/~mpyflo/Astra_dokumentation.
5. A. Novokhatski, T. Weiland, The Model of Ensembles for Beam Dynamics Simulation, PAC99, New York, p.2743.